STUDIES OF METHODS TO RESTRICT THE GRAIN GROWTH OF NANOCRYSTALLINE METAL OXIDES

By

YASSER AL-ANGARI

Thesis submitted as part of the
requirement for the degree of
Doctor of Philosophy in
Chemistry.

University of Kent at Canterbury

August 2002

Acknowledgments

I would first like to thank my supervisor, Professor Alan V. Chadwick, as I am very much indebted to him for his support, guidance, helpful comments and patience throughout the course of the PhD. I also thank everyone in the School of Physical Sciences who have helped me during the course of these studies.

I would like to thank the staff at the Daresbury Laboratory, particularly the station managers for all their help during my visits.

I would like to thank my fellows Georgios Rafeletos and Georgina Rush for their help and support throughout my PhD. Thanks go to everyone at Kent who have helped to make my time here enjoyable.

I gratefully acknowledge my wife and my daughter Jawana for their love, care, support and continuous encouragement. Many thanks should go also to my grandmother, my mother, and my uncles, my brothers and sisters and to the rest of the family who are always beside me, and I dedicate this thesis to them.

I would like to thank the financial support from King Abdulaziz University , Jeddah - Kingdom of Saudi Arabia. I am also grateful to the Saudi Cultural Bureau Office in the United Kingdom for their support during my period as a student.

Finally thanks to anyone who helped me, even if they were not aware of it.

ABSTRACT

There is considerable interest in nanocrystalline materials. This thesis is concerned with nanocrystalline oxides and the development of methods to prevent their grain growth on heating. This growth, which is evident at temperatures as low as 400°C, presents a serious problem in the study and applications of nanocrystalline oxides. The systems that were studied were nanocrystalline magnesium oxide, zirconium oxide, cerium oxide and tin oxide. The methods of preventing grain growth included the encapsulation of the oxide in the pores of porous silica, mixing with nanocrystals of alumina and treating the surface with a silanising agent, hexamethyldisilazane.

All the methods employed showed some effect on reducing the grain growth. Encapsulation in the pores of silica was effective, however it proved difficult to get large amounts of the oxides into the pores. A more efficient method of preparing large samples was the incorporation of alumina, which was achieved by a sol-gel process. An alkoxide of the target oxide and an aluminium alkoxide were mixed and then hydrolysed and calcined. This proved very effective for magnesium oxide, zirconium oxide and tin oxide. For example, heating zirconium oxide at 1000°C for 60 minutes causes the nanocrystals to grow to about 50nm. Treatment with alumina restricts the growth to 12nm. Similar effects were found for the other oxides, although magnesium oxide showed a reaction with alumina at the highest temperatures. Silanising the surface was only studied for tin oxide and it restricted growth at 1000°C to 27nm, compared to 88nm for an untreated sample.

A full description is given of the preparative methods and structural studies of the systems using X-ray diffraction and X-ray absorption spectroscopy.

CONTENTS

LIST OF FIGURES

LIST OF TABLES

I INTRODUCTION

I.1 INTRODUCTION TO NANOMATERIALS

The last decade has seen an explosion of interest in *nanoscience* or *nanotechnology*, which refers to the study of materials with particle sizes in the nanometre regime. This covers all areas of science, including biology, chemistry, physics and engineering. Historically, the term nanotechnology has been accredited to Eric Drexler who first used it in his book *Engines of Creation* in 1986 (Drexler, 1986, McLellan, 2002). The foreword from this book summarises the concepts of nanotechnology and is given below:-

"Engines of Creation begins with the insight that what we can do depends on what we can build. This leads to a careful analysis of possible ways to stack atoms. Then Drexler asks, "What could we build with those atom-stacking mechanisms?" For one thing, we could manufacture assembly machines much smaller even than living cells, and make materials stronger and lighter than any available today. Hence, better spacecraft. Hence, tiny devices that can travel along capillaries to enter and repair living cells. Hence, the ability to heal disease, reverse the ravages of age, or make our bodies speedier or stronger than before. And we could make machines down to the size of viruses, machines that would work at speeds which none of us can yet appreciate. And then, once we learned how to do it, we would have the option of assembling these myriads of tiny parts into intelligent machines, perhaps based on the use of trillions of nanoscopic parallel-processing devices which make descriptions, compare them to recorded patterns, and then exploit the memories of all their previous experiments. Thus those new technologies could change not merely the materials and means we use to

shape our physical environment, but also the activities we would then be able to pursue inside whichever kind of world we make."

Although Drexler is credited with creating the term nanotechnology the first person to speculate on building devices at the atomic level was the quantum theorist and Nobel Laureate Richard Feynman (Pesce, 2001). Pesce's summary and comments on the Feynman's his famous 1959 lecture "*There's Plenty of Room at the Bottom*" are quoted below:-

" Feynman examined the infant field of materials science. He hypothesised that as scientists learned more about how to make transistors and other small-scale structures, they would be able to make them smaller and smaller. Eventually they would approach their natural limits, at the edges of quantum uncertainty, stopping only when the atoms themselves became too slippery, too unknowable, to be mechanically reliable. Before molecular biology, such speculations seemed wild and unfounded, but Feynman is once again proving to have been correct. The detailed study of the structures of the cell revealed that nature had engineered machinery from the insubstantial substance of a few atoms strung together; the search for a "vital force" only revealed a bewildering array of mechanisms-- enzymes, ribosomes and other tiny structures - which demystified the cell even as it revealed the incredible versatility of atomic-scale chemistry. Feynman postulated that once the tidy language of atoms had been decoded, it would be possible to engineer molecules precisely, placing one atom against another to create the smallest possible artefacts. What kinds of tools might we create with these ultra-miniaturized forms? Feynman imagined a molecular "doctor" that would be hundreds of times smaller than an individual cell. It could be injected into a human body and go to work, reading the health of cells, making repairs, and generally keeping the body in perfect health. Science fiction, his peers said. Absolute fantasy tossed off by

the master storyteller of physics. During the heights of the Industrial Age, "big" carried an importance of its own- big science, big engineering projects, big dreams. Even computers, in the 1950s, consumed whole floors of buildings. But even as Feynman made his address, engineers at Texas Instruments put the finishing touches on the first integrated circuits, and the world began to grow small."

There is now a vast and rapidly growing literature on nanotechnology with papers appearing in the literature. There are also recently created specialised new journals in this field; for example, Journal of Nanoparticle Research (Kluwer), Nano Letters (American Chemical Society), Journal of Nanoscience and Nanotechnology (American Scientific Society), Nanotechnology (Institute of Physics) and Nanotechnology Magazine (Kelvin Publishing). A number of countries have invested large amounts of research funding into nanotechnology. In the United States the National Science Foundation has a National Nanotechnology Initiative (website; www.nsf.gov/search97cgi/vtopic) which began in 1991 and the budget for the financial year is $422 million. The EU has programmes on Nanotechnology Information Devices (website; http://www.cordis.lu/ist/fetnid.htm) and Nanoscale Integrated Circuits (website; www.cordis.lu/esprit/src/melari.htm#nano), each with budgets of some tens of million Euro, and more programmes are planned in Framework 6 (.website; ftp//ftp/cordis.lu/pub/rtd2002/docs/fp6mod_nano.pdf). In the United Kingdom the EPSRC has established nanotechnology institutes (for example at Imperial and University Colleges, London). There are also extensive programmes in Japan (Yamaguchi and Komiyama, 2001) and China (Bai, 2001) and most developed countries (Roco, 2001). The benefits are expected in many areas of life, such as health, energy saving, electronics, communications, medicine, etc.

From the various articles and web-sites quoted above it is soon very clear that there is no precise definition of nanoscience or nanotechnology. Some scientists define 'nano' in terms of the size of the dimensions of the species involved, however there are often differences as to the limiting size. Some papers take the limit as being less than 100 nm (Whatmore, 1999), whereas others assume a limit of around 10 nm (Gleiter, 2000). There is also a very wide range of scientific activity that is referred to as nanoscience. At the more speculative level there is discussion of *'molecular motors'* (Davis, 1999) where machines could be built at the atomic level. These could then be used to manipulate biological systems, such as bacteria and viruses. In addition, many areas of molecular biology, particularly those involved with DNA manipulation are referred to as nanotechnology (Seeman, 2001). Another area is that of microelectronics, where it is imagined that the components on a chip would be of nanometre dimensions, reducing size and increasing speed (Berman et al, 2000) and storage capacity (Menon and Gupta, 1999). Workers in the field of carbon nanotubes also term their research as nanotechnology (Cohen 2001). In chemistry the field of supramolecular chemistry or the chemistry of self-assembling structures, as it produces molecules of nanometre dimensions, is now often referred to as molecular nanotechnology (Fahy, 1993). Finally, just to emphasise the width of the subject, a recent focus has been on the use of atomic force microscopes (AFM) and scanning tunnelling microscopes (STM) to manipulate atoms on surface to produce nanostructures (Birdi, 1999). A recent review of the materials chemistry aspects of nanomaterials has been given by Rao and Cheetham (Rao and Cheetham, 2001).

The work in this thesis concerns the chemistry and physics of nanocrystalline oxide. The interest in simple solids, metals and oxides, in nanocrystalline form began in the 1980's and were pioneered by H. Gleiter at the University of Saarland in Germany

and R.W. Siegel at the Argonne National Laboratory in the U.S.A. Gleiter and co-workers published an article emphasising the unusual properties on nanocrystals in 1984 (Birringer et al, 1984) and this paper is cited extensively (294 times in the Web of Science at the time of writing). He has written 86 papers on nanocrystalline solids, includining two very influential reviews (Gleiter 1989, Gleiter 1992), and the former having been cited 942 times on the Web of Science at the time of writing. Siegel began to publish papers on nanocrystalline titanium dioxide in the late 1980's (Li et al 1988, Siegel et el 1988a, Siegel et al 1988b) and he was a member of the Department of Energy panel that recommended research into cluster and cluster assembled materials (Andres, 1989). He has written over 50 papers on nanocrystals and a number of reviews that have popularised the subject (Siegel 1991, Siegel, 1996). Both these authors stress the unusual behaviour of nanocrystal arising from the fact that as the particle size approaches, or becomes smaller than, the critical length for certain phenomena, e.g. the de Broglie wavelength for the electron, the distance required to form a Frank-Reed dislocation loop, etc. In addition, when the particle size approaches the nanometre regime a large fraction of the atoms are in the surface region and hence unusual behaviour is expected, particularly in terms of the surface chemistry.

At this point it is appropriate to review the unusual properties expected of nanocrystals and a good starting point is the review by Gleiter (1992). Gleiter begins his review by considering the disorder in bulk defects in normal materials, i.e. grain boundaries and dislocations. He argues that the density is low in these regions and hence there are unusual properties. He then goes on to consider a nanocrystalline sample where a large fraction of the atoms are in the surfaces and argues that the sample will behave very much like a grain boundary. Gleiter's view of a nanocrystalline

sample is shown in Figure I.1. The fraction of atoms in the surface of a spherical nanocrystal of MgO is shown in Figure I.2, which is about 50% at 3 nm.

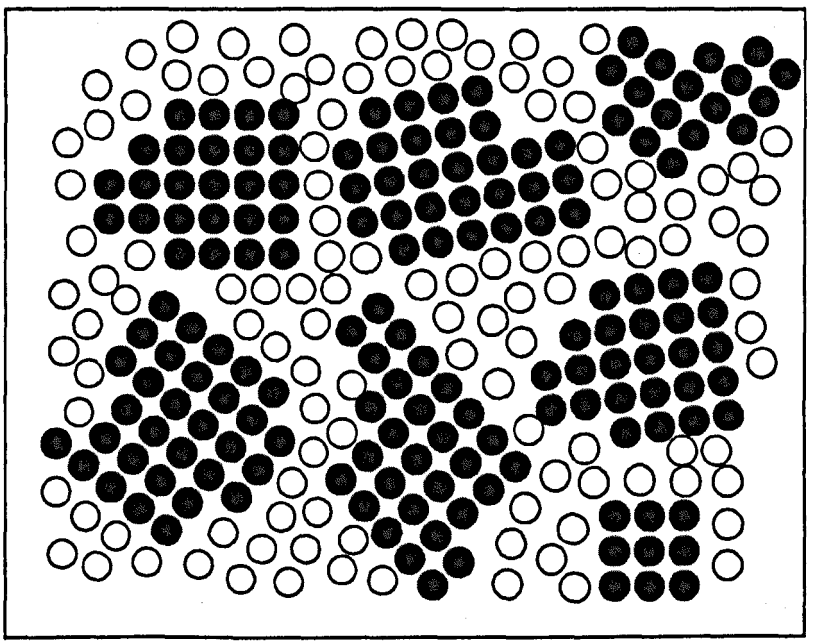

Figure I.1: Gleiter's picture of a nanocrystalline sample.

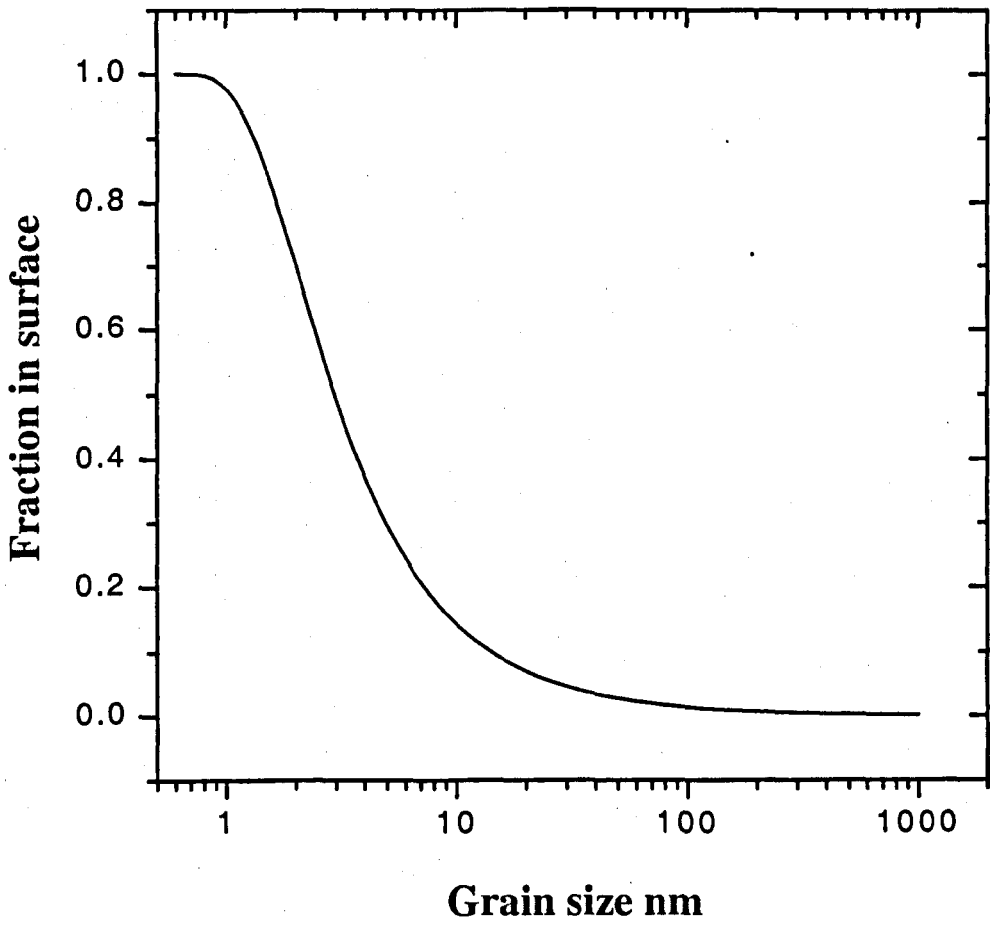

Figure I.2: The fraction of atoms in the surface of a spherical nanocrystal of MgO.

Gleiter made the following list of experimentally observed properties that were consistent with the picture shown in Figure I.1:-

1. Reduced amplitude of EXAFS oscillations.
2. Reduced Debye temperature.
3. Enhanced specific heat.
4. Enhanced solute solubility.
5. Increased thermal expansion.
6. A change in positron lifetime.

A list of the experimental observations quoted by Gleiter is given in Table I.1.

Table I.1 Experimental properties of nanocrystalline solids

Property	Bulk	Glass	Nanocrystal	System
D/m^2s^{-1} at 300K	10^{-39}		10^{-19}	$^{67}Cu/Cu$
	10^{-39}	10^{-36}	$2x10^{-19}$	Ag/Cu
Solubility/%	$<10^{-4}$		4	Bi/Cu
	10^{-3}		10^{-1}	H_2/Pd
Deformation/%	<0.1		>100	TiO_2
Magnetisation/ emu/g (4K)	220	215	130	Fe
Electronic specific heat(0.1-1K)/10^5J/gm/K^2	1.1	~1	1.6	Cu
Carrier density(electrons/atom)	1.24	~1.2	0.6	Cu

The basis of Gleiter's arguments is the highly disordered interface, which is sometimes referred to as 'gas-like'. This will explain all the observations. For example the high diffusion coefficients would be due to the migration of atoms in the disordered interface. These interfaces would also be able to accommodate other atoms, hence the high impurity solubilities. The high plastic deformation, sometimes referred to as *superplasticity,* would be due to the ease of grains sliding over each other with the highly disordered interface. With these high levels of disorder the EXAFS amplitudes would be reduced, as there would be a loss of crystallinity for a large proportion of the sample. It will be seen later that there are alternative explanations to the experimental observations and that the concept of highly disordered interfaces is not required. In fact more recent work suggests that the interfaces are more like grain boundaries in normal bulk materials (Chadwick and Rush, 2001).

In addition to the properties considered by Gleiter there are some more that need to considered. Firstly, there are the properties due to the particle size being comparable to the critical lengths for a number of parameters, e.g. the de Broglie wavelength and the depth of the space-charge region. Thus the particle size can give rise to quantum confinement and can affect the colour of a material, a good example being cadmium sulphide. In ionic materials when the particle size approaches the depth of space charge layer the point defect equilibria can be perturbed (Maier, 1995). An important property of nanocrystals is that they are extremely hard, referred to as *superhardeness*, as the crystallites are not large enough to sustain Frank-Reed loops, and dislocations can not be generated. Finally, when particles are small there is evidence that the crystalline phases and surface morphologies are different from bulk materials. When zirconia is less than ~30 nm in diameter the tetragonal phase is stable, whereas in larger crystals the stable phase is the monoclinic form (Garvie, 1965, 1978). Nanocrystals of MgO have a different surface morphology to bulk MgO (Stark et al, 1996, Stark and Klabunde, 1996, Koper et al, 1997). Thus the surface chemistry, and hence the catalytic behaviour, can be very different for nanocrystals.

The next section will deal specifically with nanocrystalline oxide, the subject of the experimental work in this thesis.

I.2 INTRODUCTION TO NANOCRYSTALLINE OXIDES

Research on nanocrystalline oxides has been on-going for over two decades and nanocrystalline titanium dioxide was the subject of the early studies by Siegel (Siegel et al 1988). In fact, there has been a great deal of early work on nanocrystalline oxides that was performed before nanomaterials became a popular area of study. A number of oxides have been prepared in nanocrystalline form for applications in catalysis. A good example of early work that was not recognised as a nanocrystal study is the preparation of zinc oxide. A route to zinc oxide from the oxychloride was published by Srivastava in 1967. This was later used by Garcia- Martinez and co-workers (1993) to prepare nanocrystalline zinc oxide and they modified the procedures to produce nanocrystalline copper (I) oxide. In the case of catalysts and catalyst supports there is a long history of using small particles, often in the nanometre regime to increase the surface area of the reagent (Anpo, 1989, and Cauqui and Rodriguez-Izquierdo, 1992). As will be shown later there are a wide variety of methods of preparing nanocrystalline oxides as both powders and thin films.

The reason for the more recent interest in nanocrystalline oxides was initiated from the ceramics viewpoint. Ceramic materials are naturally extremely hard and in the form of nanocrystals the individual particles are superhard (Averback et al, 1993, Radonjic, 1998, Hauert and Patscheider, 2000). However, normal bulk ceramic materials are brittle and fracture easily under bending stress. The use of compacted nanocrystals results in tougher ceramics as the materials are superplastic (Mayo, 1997, Mayo et al 1999). Further interest has been generated by the electrical behaviour as nanocrystalline ionic oxides have been shown to have enhanced conductivity (Kosacki et al, 2000). The origin of the enhanced conductivity had been predicted for some time

and was attributed to nanocrystallites approaching the dimensions of the space-charge layer (Maier, 1995). Recently there has been interest in nanocrystalline oxides as adsorbers of pollutant gases, for example nanocrystalline MgO can adsorb large quantities of SO_2 (Stark, et al, 1996). The effect is regarded as not simple being due to the increased surface area-to-volume ratio that is possible with nanocrystals but an extra effect due to unusual surface morphologies that occur in nanocrystals, i.e. bulk MgO surfaces are (100) crystal planes and higher order planes are found on nanocrystal surfaces. Semiconducting oxides are used in flammable gas sensors and there are a number of reports of enhanced selectivity and sensitivity when compacts of nanocrystals are used as the sensing elements, e.g. SnO_2 (Davis et al, 1998) and TiO_2 (Lin et al, 1997)

More details on nanocrystalline oxide will be given in the following sections.

I.3 PREVIOUS WORK ON NANOCRYSTALLINE OXIDES

I.3.a Preparation

There are a large number of methods that have been used to prepare nanocrystalline oxides, some of which are very specific to a given oxide. Focus here will be given to the more general methods.

A general method that is widely used is the thermal decomposition of a hydroxide. This is the common method of preparing zirconia (Rush et al, 2000). However, in a number of cases this will not produce very small crystallites, for example MgO (Stark et al, 1996). A variation is to prepare the hydroxide *via* the hydrolysis of an alkoxide, often referred to as the *sol-gel route.* (Klabunde et al, 1996, Ding and Liu, 1997). This route usually produces very small nanocrystals, e.g. 5 nm in the case of MgO (Klabunde et al, 1996). Another variation, referred to as a *polymer pre-cursor route*, is to prepare a viscous solution of a metal salt in a glycol, spin coat this on an inert substrate (e.g. sapphire) and then thermally decompose to the oxide (Suzuki et al, 2002). This method has been show to produce very perfect nanocrystals (Rush, et al, 2000). Care has to be exercised in any method that uses a decomposition of a hydroxide material in that it is often difficult to remove traces of the hydroxyl groups. This is particularly true in the case of zirconia (Chadwick, et al 2001). The advantage of the sol-gel route is that it is generally easy to prepare very large samples, a few tens of grams, or thin films. It is also relatively easy to introduce dopants at the hydrolysis stage. However, care has to be taken to remove traces of water or hydroxylated species.

Another general method that can be used to prepare a wide range of materials types (metals, oxides and other compounds) is the *vapour condensation method* (Gleiter, 1992). The set up is shown in Figure I.3. It is basically a vacuum sublimation apparatus with a cold finger to collect the sublimed material. The system is run with a

small pressure of helium in the chamber, the aim being to form the nanocrystalline particles in the gas phase, rather than simply condensing as large crystallites on the finger. In cases where the metal oxide is very involatile, then the procedure is to deposit nanocrystalline metal particles and then oxidise these particles (e.g. tin oxide was prepared by this route by Huh, et al, 1999). An advantage of the gas condensation method is that the particles are very clean and free from traces of water, a problem with the sol-gel route (Cui, 1999). However, it is rather slow and produces relatively small samples; it takes several hours to produce one gram of material. It is also difficult to produce uniformly doped materials by this method. There are several variations of the method, usually in the form of the vapour source. The source can be provided by heating in a crucible, such as laser ablation (Fang et al, 2002) and radio-frequency sputtering (Comini et al, 2001).

Nanocrystalline oxides have also been prepared by *chemical vapour deposition methods (CVD)*, where a volatile compound, usually a metal alkyl or alkoxide is decomposed in the presence of oxygen on a heated substrate (Veith et al 1999). The technology is the same as that used to produce semiconductor films, such as silicon (Komiyama et al, 1999). This is an excellent method of producing thin films and it is possible, as in semiconductors, to introduce dopants.

Many nanocrystalline systems have been produced by *high-energy ball-milling*, sometimes referred to as *mechanical attrition* (Indris et al, 2000). The material is simply ground to a small size. A number of oxides have been prepared as nanocrystals by this route. This route has the advantage that is fairly rapid and relatively easy to

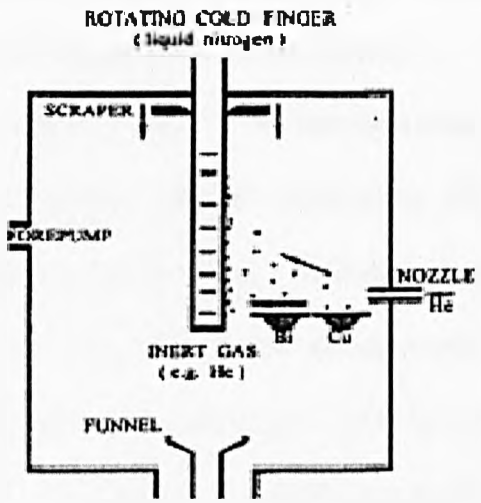

Figure I.3: Vapour condensation apparatus (used to prepare nanocrystalline bismuth-copper alloys).

produce large samples, the order of a few grams. It is also possible to use the ball milling to synthesise compounds in nanocrystalline form. For example $PbTiO_3$ has been prepared by milling PbO and TiO_2 (Kong et al, 1999). A disadvantage is that it is difficult to avoid contamination from the balls. In addition, the nanocrystals produced show a wide variation in size and there is often the production of amorphous material (Gajovic et al, 2001, Scholz et al, 2002).

I.3.b Properties

Some general properties of nanocrystalline oxides have been mentioned in Section I.1, particularly from the ceramics viewpoint. It is worth noting here some of the important properties and the current explanation of them.

The most important property is that of the microstructure, as this will underlie the chemical and physical properties. Recent work using EXAFS has shown that nanocrystalline oxides prepared by sol-gel type routes do not have highly disordered interfaces (Chadwick and Rush, 2001). In other words the model developed by Gleiter and shown schematically in Figure I.1 is not correct. This has been proved for several oxides including zinc oxide (Chadwick et al, 1994), tin oxide (Davis et al, 1997), zirconia (Rush et al, 2000, Rush 2001) and ceria (Rush, 2001). Although there are several EXAFS studies that claim there is a disordered interface in nanocrystalline oxide this has been shown to be a result of the method of sample preparation (Chadwick and Rush, 2001). For example, zirconia samples prepared by heating zirconium hydroxide will contain hydroxide groups unless they are heated to sufficiently high temperature. Also nanocrystalline samples prepared by ball-milling are different and appear to contain amorphous material (Gajovic et al, 2001, Scholz et al, 2002, Al-Angari et al, 2002) and need to be considered as separate from normal nanocrystals. Thus it seems reasonable to assume that the interfaces in all oxides, certainly those that are strongly ionic are like normal grain boundaries.

Surface morphology of nanocrystalline oxides has been reported as being different to bulk material in the case of MgO (Stark, et al, 1996). The evidence for this came from the adsorption behaviour and some preliminary AFM studies. A search of the literature shows that there have been few studies of the morphology of nanocrystalline oxides, particularly as a function of size. A great deal of the work on

nanocrystalline oxides involves the study of thin films on substrates and there the morphology is determined by the substrate. It is an interesting question for free standing particles, as the surface energy is a major contribution to the total energy of a nanocrystal. A classic case is the formation of the tetragonal form of zirconia when prepared as nanocrystals in contrast to the stable bulk form being monoclinic. Garvie (1965,1975) noted this over 25 years ago. Small crystallites, less than about 30nm prepared by the usual sol-gel route are tetragonal. Heating and subsequent grain growth causes a transformation to the monoclinic form. The argument for the origin of the tetragonal form has been that it is stabilised by the surface energy. It is argued that the tetragonal form is kinetically metastable. It should be noted that there has been considerable debate over the transformation and the temperature of the transition is very dependent on the method and conditions of the preparation. (Turrillas et al, 1995). Recently it has been shown that nanocrystalline monoclinic zirconia could be formed by mechanically treating the tetragonal particles, but on heating these transformed back to the tetragonal form. This suggests that the tetragonal form is truly thermodynamically stable in nanocrystals. The technical importance of zirconia has meant there have been many studies of this system. It is interesting to know if similar effects occur in other oxides or if it is specific to zirconia.

There has been considerable recent interest in the electrical conductivity of the ionically conducting oxides (Maier and Tuller, 2000). The start of the interest goes back to the 1970's when Liang (1973) found that mixing fine particles of an insulator, like alumina or silica, with a simple ionic salt led to an unusually high conductivity. There were a number of explanations of the effect that were proposed but the one that has prevailed is that developed by Maier (1995) which is based on the space charge region. Maier proposed that the effect of the additions was to introduce many

interfacial regions into salt by adding the insulator. In these interfacial regions the space charge region would affect the defect concentrations. It is known that the energies of formation of individual defects in an ionic crystal are not the same for the members of a pair; for example, in sodium chloride the energy to form a cation vacancy is not the same as the energy to form an anion vacancy. Thus the energetics alone would suggest that there would be a different concentration of each defect in a crystal. However, the defects are charged and electrical neutrality demands an equal concentration of each defect in a bulk crystal. The restriction of electrical neutrality does not apply at a surface or interface and there will be differences in the defect concentrations. This leads to the space charge layer. Maier argued that there can be high defect concentrations in the interface and the interfaces can therefore provide high conductivity paths in these salt-insulator mixtures. He has given a full theoretical derivation (Maier, 1995). In principle the same theory can be applied to a nanocrystal when its diameter is the order of the thickness of the space charge region. Thus a compact of nanocrystals should have a high conductivity due to the conduction in the surface regions, with a limit being reached when the crystallite size was less than the depth of the space charge region. Although the theory was known for some time the experimental proof of the effect has only recently been reported. The work on films of nanocrystals has led to conflicting results (Tuller, 2000). Nanocrystalline ceria is highly conducting, as shown by a number of workers, but it is electronic rather than ionic conduction due to the formation of Ce^{3+} in the nanocrystals. Studies of nanocrystalline zirconia have yielded a varied set of results, some studies showing enhanced conductivity and some a normal conductivity. Recent work by Kosacki et al (2000) on well-characterised films does claim to show unambiguous enhanced conductivity. The space charge enhancement of the conductivity in ionic solids, although not oxides, has

been proved experimentally by Sata et al (2000). These workers prepared alternating films of CaF_2 and BaF_2 and they varied the thickness of the layers. The conductivity was measured perpendicular to the layers, i.e. along the interfaces. As the layer thickness approached the calculated thickness of the space charge layer the conductivity rose, in agreement with Maier's theory, and conductivities an order of magnitude over the pure materials were produced. The results of the work are shown Figure 1.4. This work has proved the effects can be produced experimentally and has led to an interest in developing the effects in the oxides where high oxygen conductivity would have many technological applications, particularly in fuel cell electrolytes (Kosacki, 2002).

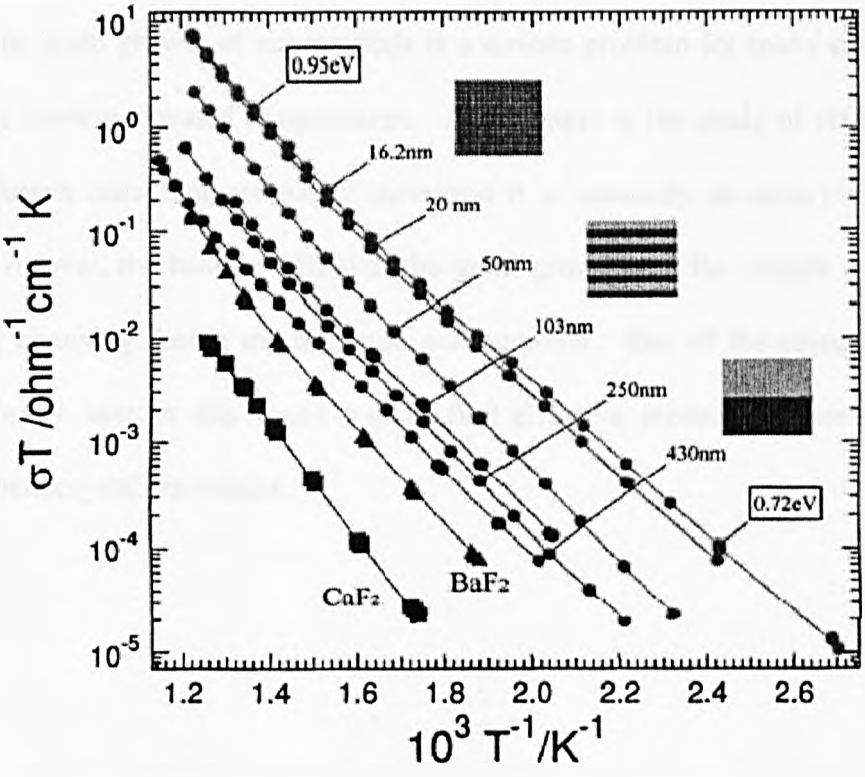

Figure I.4: Conductivity of films consisting of alternating layers of BaF_2 and CaF_2. The thickness' of the layers are shown on the plots.

A general property of all nanocrystals is that they will readily grow at quite moderate temperatures. The fundamental reason is that particles will tend to grow to reduce the surface area to volume ratio and hence reduce the surface area. The mechanism can vary from system to system, i.e. it can be due to diffusion sintering, evaporation and recondensation (sometimes referred to as Ostwald ripening) and vapour transport. Grain growth is important in ceramics, particularly in the formation of dense materials from powders (Shaw, 1989, Xue and Brook, 1989). An example of the growth of a nanocrystalline oxide is shown in Figure I.5, where data for SnO_2, taken from Davis et al (1997), are displayed. The samples, 2-3 nm crystals, were being heated at 5°C per minute and the diffraction pattern was collected. The pure material clearly begins to grow at only 400°C. It is interesting that the presence of dopants inhibits the growth. The grain growth of nanocrystals is a serious problem for many experimental studies that involve elevated temperatures. An example is the study of diffusion. To obtain diffusion rates that are easily measured it is normally necessary to heat the sample. However, the heating will start the grain growth and the sample size will be continually changing during the diffusion measurement. One of the objectives of the work presented later in this thesis was to find effective methods of preventing the growth of nanocrystalline oxides.

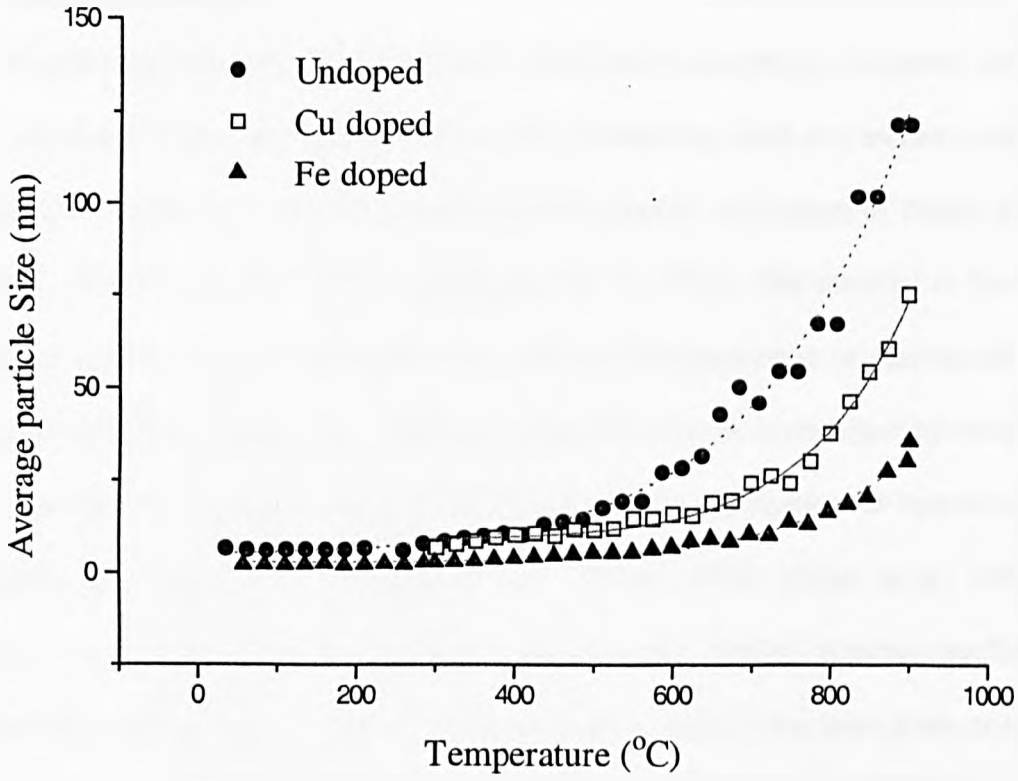

Figure I.5: The average particle size of tin oxide nanocrystals when heated at 5 degrees C per minute.

I.3.c Specific materials

I.3.c.1 *Magnesium Oxide*

Magnesium oxide, MgO, is one of the most studied materials as it is purely ionic and has the simple rock-salt structure. It has been extensively used as a model system for computer simulation studies of oxides (see, for example, the papers of Parker and co-workers; Harris et al, 1999,2001, and Kenway et al, 1992). The material is found naturally as periclase and can be prepared by thermal decomposition of various salts, e.g. acetate, hydroxide, nitrate, etc. Nanocrystalline MgO can be synthesised by several routes, however the simplest and most effective is by the calcination of hydrolysed magnesium methoxide, $Mg(OCH_3)_2$ (Stark et al., 1996a, 1996b, Koper et al., 1997, Chadwick et al., 1998). As mentioned earlier the surface morphology of nanocrystalline MgO has been reported as being different to bulk material and this has been given as the reason for the very high adsorptive power of nanocrystals of this oxide (Stark, et al, 1996). The main interest in nanocrystalline MgO is as an adsorbent of pollutant gases. MgO is an ionic conductor, however the high melting point (2800°C) means that the pure material needs to be heated to very high temperatures to obtain measurable diffusion or conductivity. In addition, it cannot be highly doped with aliovalent impurities. Hence there has been little interest in the conductivity of this material, even in nanocrystalline form. The fact that magnesium is a light element means that it cannot easily be studied by many techniques and there are no EXAFS data available for nanocrystalline MgO.

I.3.c.2 Zirconium Oxide

Zirconium oxide, zirconia, occurs naturally as the mineral baddeleyite which has a monoclinic structure. The phase diagram of zirconia is complex, particularly when doped with lower valency cations, such as yttrium, and is shown in Figure I.6. At room temperature the stable phase is monoclinic but on heating it transforms at 1400K to the tetragonal form, and then at 2640K to a cubic, fluorite-structured phase. The addition of lower valent cationic dopants at low concentrations will stabilise the tetragonal phase and at concentration exceeding ~8 mol per cent the cubic phase is

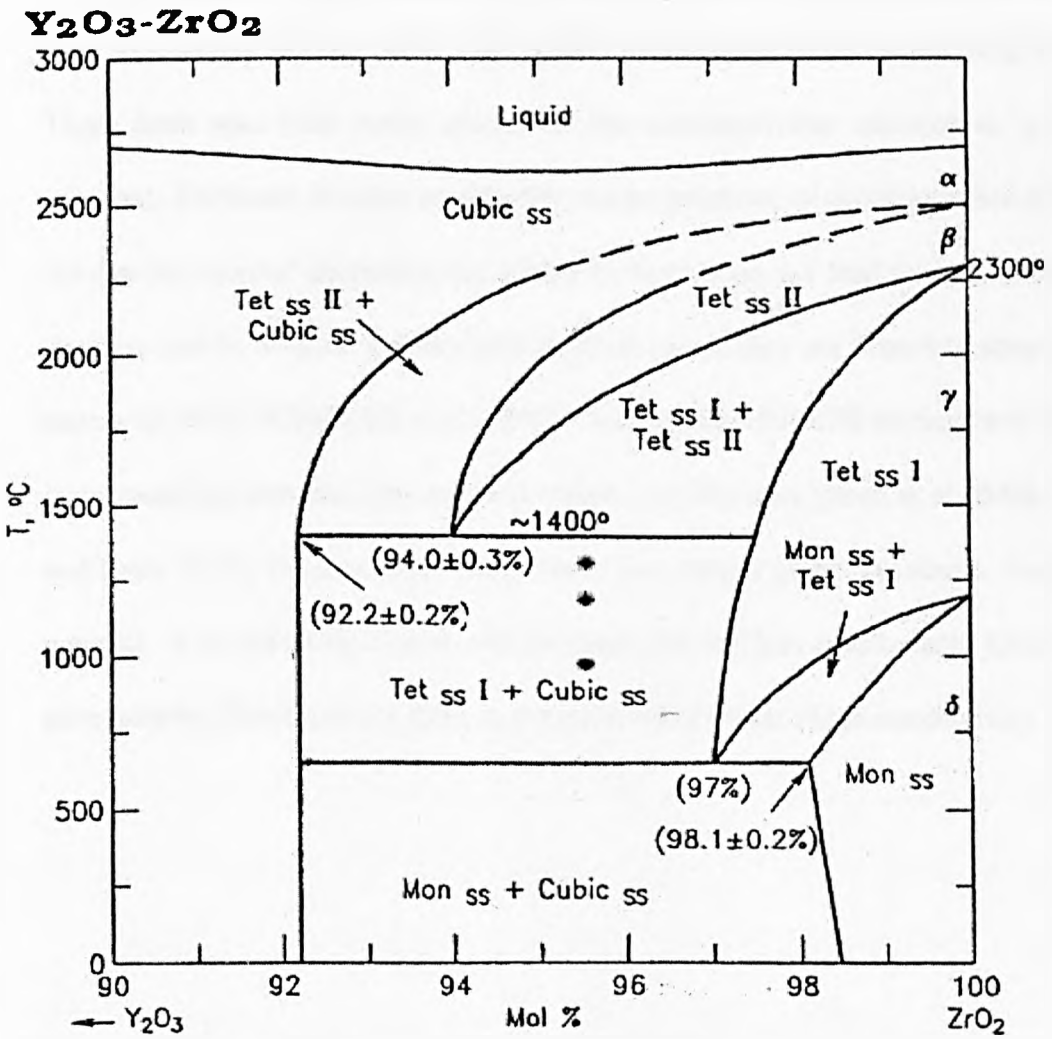

Figure I.6 The phase diagram of zirconia.

stabilised. Although the monoclinic phase is the stable room temperature phase when the material is prepared as nanocrystals (> about 30 nm particle size) other phases can form, most commonly the tetragonal form (Garvie, 1965, 1978). Zirconia is second only to diamond in terms of hardness and is used as a specialised ceramic (Birkby and Stevens, 1996). The cubic stabilised material, normally by the addition of yttrium (so-called YSZ) has a high oxygen ion conductivity at ~1000°C and is used in gas sensors (Steele et al, 1981), and as an electrolyte in solid oxide fuel cells (SOFC) (Badwal, 1990) and oxygen separators (Ziehfreund and Maier, 1996).

The importance of zirconia as a ceramic and an electrolyte has meant that it has been extensively studied, with over 10,000 publications listed on the Web of Science. There have also been many studies of the nanocrystalline material as it is readily prepared. However, as mentioned earlier, the preparations of nanocrystalline zirconia that involve the thermal decomposition of the hydroxide do not lead to pure zirconia. The samples tend to contain hydroxylated material unless they are heated to temperatures in excess of 700°C (Chadwick et al, 2001). Very careful EXAFS studies have shown that nanocrystalline zirconia does not have disordered interfaces (Rush et al, 2000, Chadwick and Rush 2002), the interfaces being more like normal grain boundaries found in bulk material. It is interesting to note that the same type of films used in these EXAFS studies were used by Kosacki et al (2000) in the studies that found a high conductivity.

I.3.c.3 *Cerium Oxide*

Cerium oxide, ceria, (CeO_2) has the cubic fluorite-structure (space group Fm3-m) when pure or doped with lower valent cations. The pure material is a mixed electronic and oxygen ion conductor. The doped material (e.g. 8 mol per cent Gd) is a purely ionic conductor and can be a better oxygen ion conductor than YSZ at equivalent temperatures (e.g. Gd-doped CeO_2) and offers the potential for an SOFC operating at lower temperatures (Kharton et al, 2001). Ceria is also an important oxidation catalyst and along with platinum, rhodium and gamma alumina makes up the 'three-way' automotive catalyst used in car exhausts to reduce the emission of carbon monoxide and hydrocarbons.

There have been some studies of nanocrystalline ceria. Like zirconia care is need in the preparation to ensure the removal of hydroxylated species. EXAFS studies of carefully prepared nanocrystalline films show again that the interfaces are not disordered (Chadwick and Rush, 2001). Several studies have been made of the conductivity of nanocrystalline ceria and there is overall agreement that the conductivity is enhanced compared to the bulk material (Tuller, 2000). However, the conductivity is not ionic and is due to the generation of Ce^{3+} ions and a hole conductivity.

I.3.c.4 *Tin Oxide*

Tin oxide occurs naturally as cassiterite and has the rutile structure (space group P42/mnm). It is an *n*-type semiconductor, which is used in flammable gas sensors (Sberveglieri, 1992, 1995, Barsan et al 1999). The principle of operation is based on the fact that tin oxide in a vacuum has a relatively high conductivity. However, in air the surface is covered with chemisorbed oxygen, which traps the mobile electrons. A flammable gas in the atmosphere will react with the chemisorbed oxygen and release the

trapped electrons. Thus a simple measurement of the electrical conductivity of a pellet of tin oxide can detect flammable gases at parts per million levels. These sensors are sold commercially (known as Taguchi sensors and sold by Figaro, Japan). A severe problem with these sensors, and the reason for their not being recommended by UK gas companies, is that they are not selective and will respond to any flammable gas, i.e. methane or alcohol or cooking fats. Strategies that have been employed to improve the sensitivity and selectivity have included the use of nanocrystalline materials and doping with aliovalent cations (Davis et al 1998).

The preparation of nanocrystalline tin oxide by reacting a solution of tin chloride with ammonia will yield material 2 to 3 nm in size. The material seems to pure and free from hydroxylated species. There is general agreement amongst the various EXAFS studies that the nanocrystallites are not highly disordered and the interfaces are like normal grain boundaries (Davis et al, 1997, Chadwick and Rush, 2001).

I.4 OBJECTIVES OF THE PRESENT STUDY

The preceding Sections have outlined the importance of nanocrystalline solids and described work on the nanocrystalline oxides. As mentioned in these Sections the growth of the oxides at moderate temperatures presents problems. From the fundamental viewpoint this limits the type of experimental work that can be performed. For example, the enhanced ionic conductivity of the nanocrystalline oxides is of great current interest. However, conductivity measurements are not discriminating as to the origins of the enhanced ionic motion. They only measure the overall charge transport and do not focus on a particular ion. A better approach would be to study the diffusion of the oxygen ions in nanocrystalline zirconia. In principle these can identify motion in a surface region, as predicted by the space charge layer models. This is possible with ^{17}O NMR and there are plans at Kent to make these measurements for zirconia. However, the experiments will require studies at relatively high temperatures, at least up to 1000°C, and this would cause rapid crystallite growth. From the technological viewpoint there is a need to maintain the nanocrystal size. For example although nanocrystalline tin oxide is a better gas sensor than the bulk material (Davis et al 1998) the sensor is operated at around 500°C and the crystallites grow with a degradation of the sensing behaviour. Similarly, the reported high adsorptive power of nanocrystalline oxides, such as magnesium oxide, is of little use unless the materials can be simply recycled. The obvious approach would be to heat the oxides to desorb the gases but this would lead to crystallite growth and loss of activity. Thus the stabilisation of the crystallite size at high temperatures is very important and this is the objective of the work in this thesis. The aims of the work are to find methods that are generally applicable to a wide range of oxides, that allow the preparation of large samples (a few

grams), that do not affect the major properties of the nanocrystals and to characterise the materials. The requirement of large samples is to enable a wide range of characterisation techniques to be used and to provide samples big enough for future studies, such as NMR diffusion.

To date there have been very few attempts to find general methods of stabilising nanocrystals, particularly nanocrystalline oxides. One approach that has been widely used is to confine the nanocrystal inside a porous matrix. The matrix used has very fine pores, as in zeolites and other microporous solids. This approach was first used by Barrer (1958, 1983) to form silver particles in the pores of zeolites and was employed more recently by Anderson et al (1996) to form potassium metal wires in zeolite L and cobalt particles in zeolite X. The silica matrix is useful as the pore size can be varied from less than 1 nm, as in zeolites, to 10 nm, as in the MCM mesoporous silicas (e.g. Mukherjee et al, 2001), to very large pores that can be produced in sol-gel prepared silica. In addition, it is possible in some cases to prepare the matrix and the nanoparticles simultaneously, via a sol-gel route. This has been used for both silica matrices (Zaharescu et al, 2000) and alumina matrices (Tang et al, 2001). Polymer matrices can also be used and the nanoparticle formed inside a porous polymer, as for TiO_2 in PPV (Zhang et al, 2001) or the polymer formed around a nanoparticle, as for silver in polymers (Akamatsu et al 2000). This general confinement approach will be used in the present work on nanocrystalline oxides. Clearly organic polymer matrices will not be useful, as they will decompose on heating. The silica matrices clearly offer the best prospects, however reaction between the oxide and silica at high temperatures will need to be explored.

In ceramics and metallurgy the growth of grains can be inhibited by the addition of a second phase material. The effect is referred to as *Zener pinning*, as the second

phase stops the movement of the grain boundaries and the growth rate of grains is reduced. This is used to maintain a small grain size when a compact is densified. The second phase is normally added in small amounts. A commonly used second phase is alumina. In principle this approach could be used to stabilise nanocrystals, however in the case of oxides it has only been used to stabilise nanocrystalline zirconia. There are several reports of adding alumina to nanocrystalline zirconia. These mostly focus on the composites with relatively large micron size grains. Viswanath and Ramaswamy (1999) used a mixture of zirconium and aluminium alkoxides to form a gel which was hydrolysed and heated to form the oxide. The amounts of alumina used were 5, 10 and 15% and the particle size was maintained at 11nm at 900°C and ~30 nm at 1000°C. Betz et al (2000) prepared nanocrystalline zirconia and alumina by gas phase condensation, about 14%, and densified the material at 1200°C and the particle size was maintained at <40 nm. Thus this approach of pinning the boundaries shows possibilities as a general method of restricting the growth of nanocrystals and one that will be explored for a number of oxides in this thesis.

Another approach that could have wide usage is to coat the surface of a nanocrystal with an inert material. Again this has not been widely used, although there has been a report of coating tin oxide, titanium dioxide and zirconia with a thin layer of silica (Wu et al 1999). This was achieved by treating the nanocrystals with hexamethyldisilazane, known as HMDS. This reacts with surface hydroxide groups on the oxide surface to form silicate units. In the original work very small crystallites were used 1 to 5 nm and the particle size was maintained on heating at 500°C. This is a relatively low temperature, however this approach is worthy of further pursuit and will be explored as a general method in this thesis.

I.5. THEORY OF EXPERIMENTAL TECHNIQUES

I.5.a X-ray diffraction

The early work of the Braggs (William and his son Lawrence) treated the scattering of X-rays as the reflection from successive planes of atoms in the crystal. This is considered schematically in Figure I.7. The X-rays are taken as a set of parallel planes impinging on the crystal at some angle θ to the lattice planes. Some of the rays will be 'reflected' from the upper layer of atoms, the angle of reflection being equal to the angle of incidence. Some of the X-rays will be absorbed and some will be reflected from the second layer, and so on with successive layers. All the waves reflected by a single plane will be in phase. Only under certain conditions will the waves reflected by different underlying planes be in phase with one another. The condition is that the difference in the path length between waves scattered from successive planes must be an integral number of wavelengths, $n\lambda$. If we consider the reflected waves at some point outside the crystal, this path difference for the first two planes is δ, where $\delta = AB + BC$. Since the triangles ALB and COB are congruent, $AB = BC$ and therefore $\delta = 2\,AB$. Hence $\delta = 2\,d\,sin\Theta$. Thus the condition for reinforcement or Bragg 'reflection' is given by

$$n\lambda = 2d\,sin\theta \qquad \textbf{(I.1)}$$

This is known as the Bragg equation.

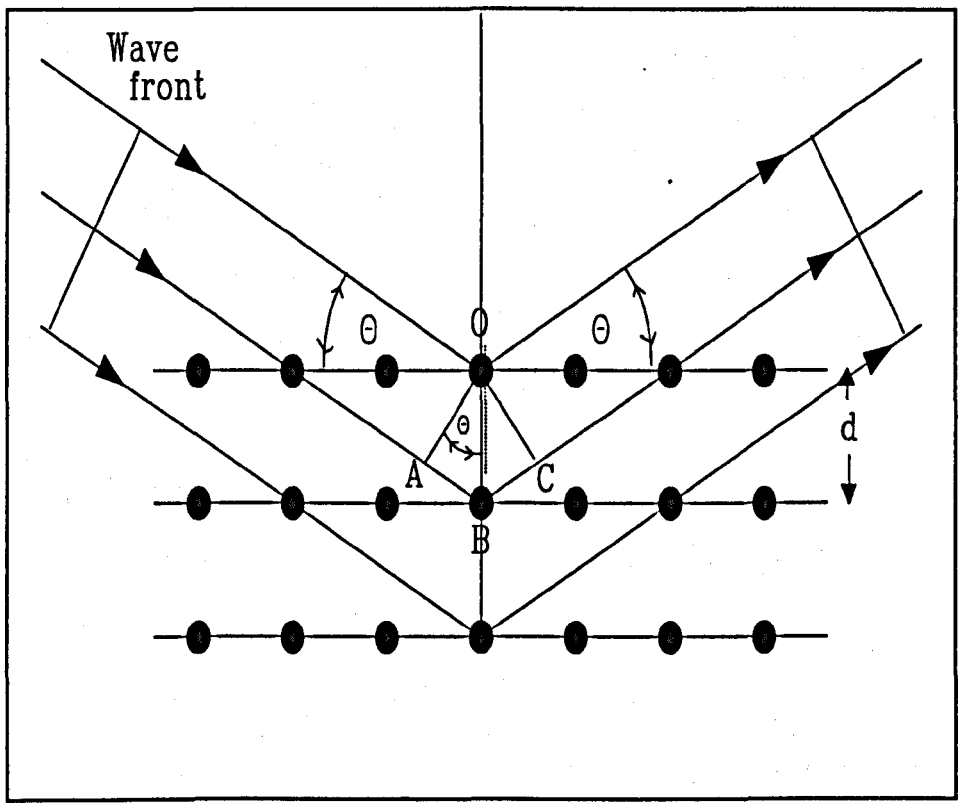

Figure I.7: Demonstration of the derivation of the Bragg equation

There are a variety of experimental methods to collect X-ray diffraction data (Klug and Alexander, 1974). The Laue method involves diffracting X rays from a single crystal and collecting the pattern on a photographic plate, or with modern instruments an area detector. Diffraction leads to a series of spots on the plate which correspond to diffraction from different crystal planes. Analysis of the positions and intensities of the spots yields the crystal structure of the material. When the sample consists of a powder the Debye-Scherrer method is employed. In this case the X-ray beam is diffracted from randomly oriented crystallites in the powder. This produces diffraction cones and with a photographic plate the result is a series of circles. The commonly used arrangement for powder diffraction instruments is shown in Figure I.8. Instead of a photographic plate a

detector is used and this is moved on an arc, centred at the sample. Thus the detector cuts through the cones of the diffracted beam. Usually the sample is scanned through an angle θ and the detector through an angle of 2θ. This results in a plot of intensity versus 2θ which contains peaks when the beam is diffracted. Effectively the two dimensional Laue pattern is reduced to one dimension. A typical powder pattern is shown in Figure I.8. Until recently it was not possible to determine crystal structures from powder patterns, however this can be done with high quality data and the use of the Reitveld method. The common use of powder diffraction patterns is in the identification of materials as the patterns are unique to a given material. Comparing the pattern to a database of patterns does this. A second use, and one used extensively in the current work, is the determination of the average crystallite size.

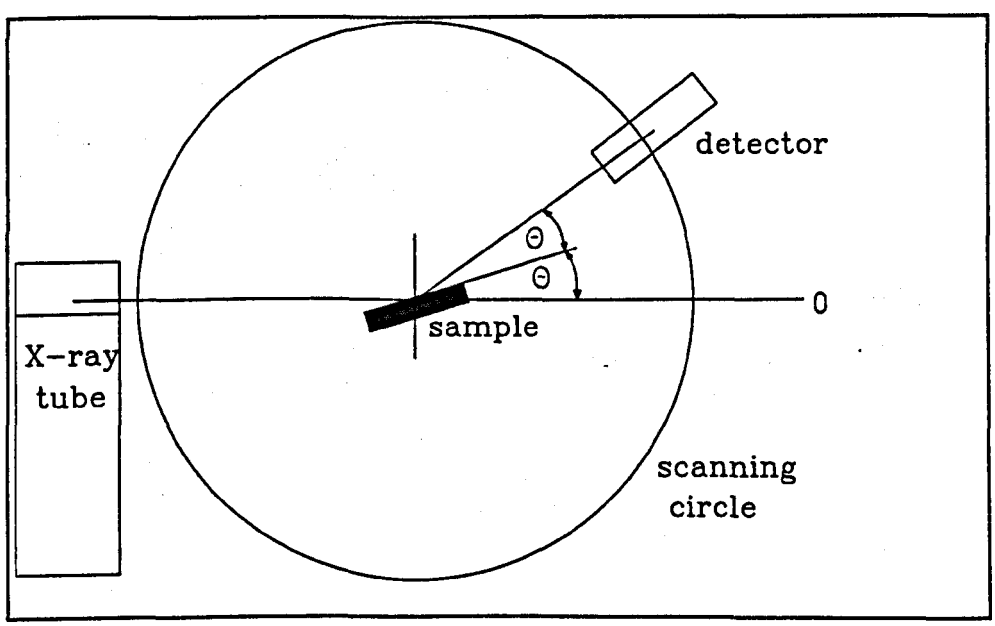

Figure I.8: Schematic picture of a powder diffractometer.

The diffraction lines given by crystalline powders become broader as the particle size gets smaller and this provides a very useful method of determining the average size of the crystallites. When considering the conditions for diffraction in perfect crystals it was shown that constructive interference occurred at certain values of 2θ as defined by the Bragg equation. At small deviations from this diffraction maximum the scattered waves will be slightly out of phase. The requirement to observe destructive interference is that the crystals must possess a large number of lattice planes such that the diffracted waves from all the planes will eventually combine destructively. For small crystals the number of planes is insufficient to result in total destructive interference. Thus the distinction between constructive and destructive interference is blurred and a broadening of the diffraction lines is observed.

The mathematical treatment of the broadening was developed by Scherrer and is given by the equation (Klug and Alexander, 1974):-

$$average\ crystallite\ size\ = \frac{k\lambda}{\beta \cos\theta} \qquad \textbf{(I.2)}$$

This is referred to as the Scherrer equation. Here k is a constant, β is the line width at half-maximum height for a diffraction peak at an angle of 2θ. The value of k depends on the method of derivation of the equation and is around unity, often taken as 0.89 (Cullity, 1978). In practice the value taken for k is not that important as the crystallite size is only expected to be accurate to $\pm$ 10% and is only useful for crystallite sizes less than about 100 nm. In using the Scherrer equation it is important to take into account any broadening of the diffraction line due to the optics of the diffractometer. This is usually done by determining the peak width of large crystallites (micron dimensions) of a highly crystalline material such as sodium chloride. Most modern diffractometers have versions of the

Scherrer equation encapsulated in the data analysis software. The advantage of the use of line broadening in determining the crystallite size is that it is very rapid and inexpensive compared to electron microscopy. Clearly it lacks the detail of electron microscopy and does not give information on the distribution of particle sizes, however the two methods do give comparable results for the average particle size.

I.5.b EXAFS

Extended X-ray absorption fine structure (EXAFS) is the study of the oscillations that occur in the absorption spectra beyond the energy for the emission of a photoelectron from a core level of an atom in condensed matter (Koningsberger and Prins, 1988). The basic EXAFS experiment involves measuring the X-ray absorption spectrum of a thin sample as a function of X-ray energy. Thus the experiment is simple and involves the measurement of the incident X-ray intensity, I_o, and the transmitted intensity, I_t, and evaluating the absorption coefficient, μ, from

$$\mu = ln \frac{I_o}{I_t} \qquad \text{(I.3)}$$

In other words, it is like any absorption experiment used in spectroscopy, such as IR.

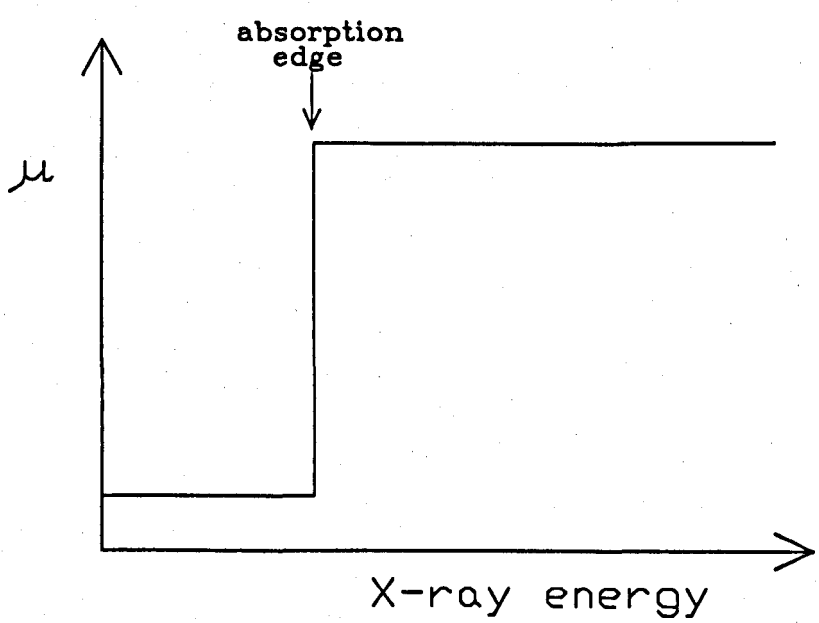

Figure I.9: Predicted X-ray absorption spectrum

Consideration can be given to what happens to the absorption coefficient as the X-ray energy (frequency) is increased. At low energies the X-rays will pass right through the sample and μ will be close to zero. As the energy is increased a point will be reached where the X-ray has sufficient energy to 'eject' an electron (a photoelectron) from the atoms of one of the elements in the sample. This will be an inner core electron, K or L shell, and X-ray will be in the energy range 1 to 40 keV. This point, where there is a very sharp rise in μ, is referred to as the absorption edge and X-ray energy, $h\nu$, will be equal to the binding energy, E_b, of the electron in its initial state. Further increasing the X-ray energy is not expected to change μ as the extra energy should simply be transformed into kinetic energy of the photoelectron. Thus the absorption spectrum would be predicted to be a simple step-function, as sketched in Figure I.9, and the final energy state, E_f, of the photoelectron in the energy balance equation, i.e.

$$E_f = h\nu - E_b \qquad \text{(I.4)}$$

would simply be the kinetic energy and have a linear dependence on $h\nu$.

Simple absorption experiments were performed in the 1920's and for condensed systems the results were *not* as simple as sketched in Figure I.9. A typical EXAFS spectrum is sketched in Figure I.10. The spectrum is usually considered in terms of three regions, marked in the figure, the *pre-edge features*, *the near-edge structure* (*XANES* - X-ray absorption near-edge structure, sometimes called the *NEXAFS* - near-edge X-ray absorption fine structure), which extends over about 50eV and the *EXAFS* (extended X-ray absorption fine structure) which are oscillations extending out about 1keV beyond the edge. Collectively the XANES and EXAFS are referred to as XAFS (X-ray absorption fine structure). The origin of pre-edge features is the excitation of electrons from a core

level to an outer bound level. These features are common in transition metals and correspond, for example in vanadium, to a 1s to 3d transition for the electron. The pre-edge features will vary in position, height and breadth as the oxidation state (i.e. electronic structure) and local symmetry of the atom changes and can be used to fingerprint oxidation - reduction reactions of a particular atom. The origins of the pre-edge features are fairly obvious, but the XAFS is more puzzling; why should the absorption coefficient show oscillations (typically with an initial amplitude about 10% of the edge step) which extend out with decreasing amplitude to about 1keV beyond the edge. The search for a proper explanation of the EXAFS in condensed matter lasted 50 years, from the early experiments in the 1920's until the early 1970's. Before the physical basis of XAFS is outlined it is interesting to consider why progress was apparently so slow. The reasons are due to the difficulty in performing the experiments and, hence, the lack of reliable data to decide between the opposing theories.

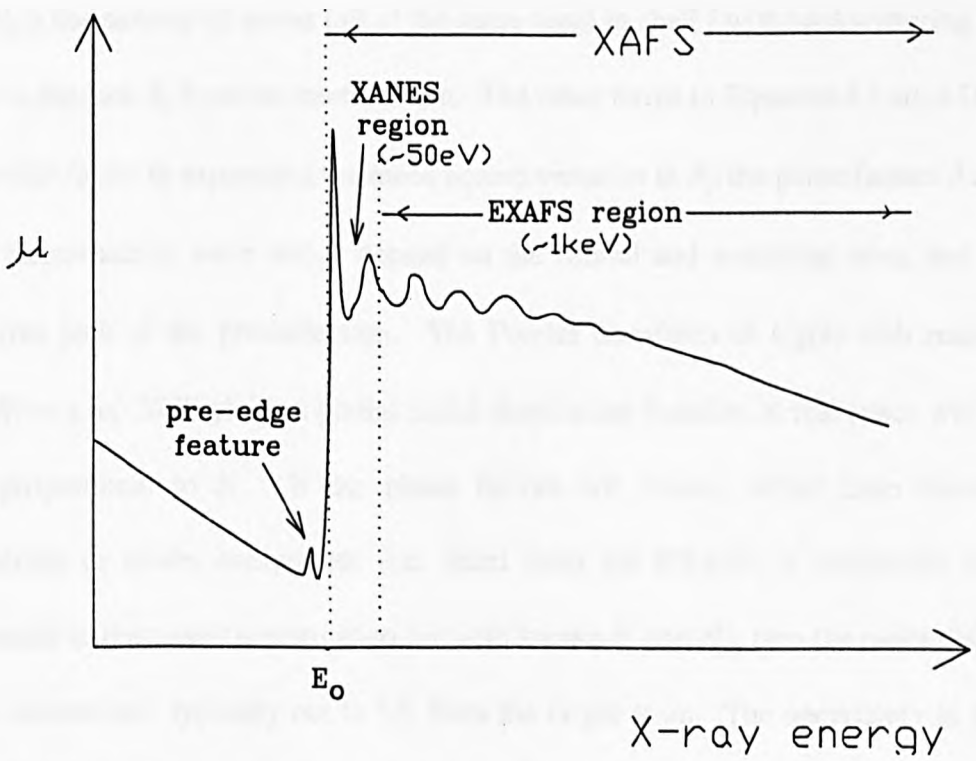

Figure I.10: The real X-ray absorption spectrum from condensed phase sample

From the qualitative explanation in the preceding paragraph it should be clear that the frequency of the EXAFS oscillations contains information on the distance from the target atom from its neighbours. The intensity of the oscillations will depend on the type of atom which is acting as the backscatterer, i.e. the higher the atomic weight the more intense the oscillations, and the number of backscattering atoms. To be more precise, after subtraction of the background absorption, the normalised absorption coefficient, $\chi(k)$, as a function of the photoelectron momentum, k, can be written in an equation of the form (Lee and Pendry, 1975, Koningsber and Prins, 1988):-

$$\chi(k) =$$

$$\sum_j \frac{N_j}{k R_j^2} |f_j(\pi)| \exp(-2\sigma_j^2 k^2) \exp(-2R_j/\lambda) \sin(2kR_j + \psi_j + 2\delta) \qquad \text{(I.5)}$$

Here N_j is the number of atoms (all of the same type) in shell j with backscattering factor $f_j(\pi)$ at a distance R_j from the central atom. The other terms in Equation I.5 are a Debye-Waller like factor σ_j expressing the mean square variation in R_j, the phase factors δ and ψ_j of the photoelectron wave which depend on the central and scattering atom, and λ the mean free path of the photoelectron. The Fourier transform of $k.\chi(k)$ with respect to $sin(2kR)$ or $exp(-2ikR)$ yields a partial radial distribution function in real space with peak areas proportional to N_j. If the phase factors are known, either from theoretical calculations or model compounds (i.e. fitted from the EXAFS of chemically similar compounds to that under investigation but with known R_j and N_j), then the radial distances can be determined, typically out to 5Å from the target atom. The uncertainty in R_j that can be achieved with EXAFS is about +/- 0.01 Å. The determination of N_j is usually less accurate, about +/- 20%, as it is strongly coupled to the Debye-Waller factor. $f_j(\pi)$ does

not vary strongly with atomic number and the identification of the type of atoms in the shells is limited to differentiation between rows of the Periodic Table. The advantages of EXAFS over diffraction methods are that it does not depend on long range order, hence it can be used to study local environments in both crystalline and amorphous solids, and liquids, it is atom specific and can be sensitive to low concentrations of the target atom.

The experiments described in this thesis were performed at the CLRC Daresbury Synchrotron Radiation Source (SRS) and it is appropriate here to describe the experimental arrangement and the method of data analysis.

Figure I.11 shows schematically the typical arrangement of the EXAFS stations at the Daresbury SRS. The 'white' beam from the synchrotron is 'shaped' by passing through lead slits (to produce a beam ~1 mm high and 10 mm wide) and then monochromated by a double crystal monochromator. The beam is diffracted from the first single crystal to select a particular wavelength of light and the further diffracted from a second crystal (with the same crystallographic cut as the first crystal) to bring the beam back to the horizontal direction. Rotating the two crystals together by means of a stepper motor will change the wavelength of the beam. The beam then passes through the first ion chamber (referred to as the reference chamber), to determine I_o, the sample, and then a second ion chamber (referred to as the signal chamber) to record I_t. The ion chambers are partially filled with a rare gas to detect the X ray and made up to a total pressure of 1 bar by adding helium. The pressure of the rare gas in each chamber is adjusted so that the reference chamber is 80% transmitting and the signal chamber is 80% absorbing. The currents on the chambers are measured with sensitive Keithley electrometers. The sample thickness is adjusted so that the change in absorbance before and after the absorption edge is approximately 1. In the case of powders the sample is mixed with a light element diluent, such as silica, boron nitride or polythene, and

pressed into a 13 mm radius pellet with an IR press. In a typical EXAFS experiment the X ray energy is scanned from approximately 50 eV below the absorption edge to 1000 eV beyond the edge. The scans are controlled by a computer system, which also records the angle of the monochromator, I_o and I_t, and records the data to a file. A scan will typically take around 30 minutes and, depending on the data quality, several scans are collected to improve the signal-to-noise ratio. When the concentration of the target element is very low in the sample, typically less than 1 atom per cent, transmission experiments are not feasible. In this case an alternative approach is to collect the fluorescence X rays with a solid state detector. This will measure I_f which is proportional to the absorption. The basic arrangement described above applies to all the Daresbury EXAFS station, i.e. 7.1, 8.1, 9.1 and 9.3. Station 9.3 is a combined station and a curved position sensitive detector can be placed in the system to measure a powder diffraction pattern of the sample simultaneously with an EXAFS scan.

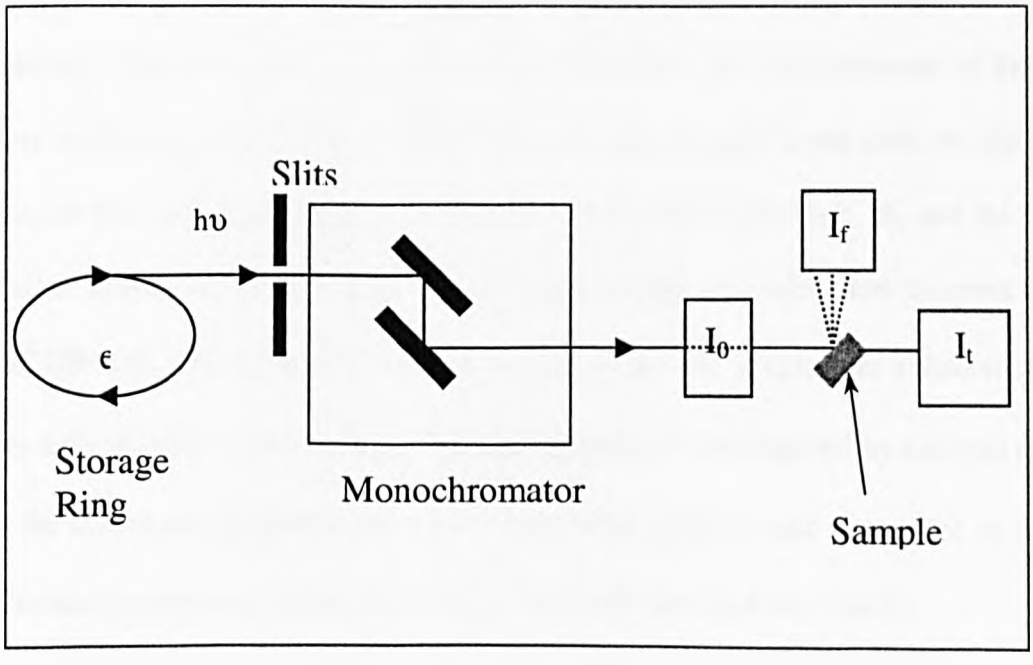

Figure I.11: A typical experimental set up for EXAFS.

The Daresbury suite of EXAFS analysis programmes were used to analyse the spectra collected in this thesis (Binsted et al, 1992, Binsted, 1998). The first programme is EXCALIB which simply calibrates the data, i.e. allows for background counts in the ion chambers and converts monochromator angle to energy. This creates a simple data file of incident X ray energy versus absorption coefficient. The second programme is EXBACK which takes the EXCALIB files and produces the normalised EXAFS, $\chi(k)$, as a function of k, the X ray wave vector. This involves determining the EXAFS oscillations by subtracting the absorption spectrum for the atom, i.e. producing the spectrum caused by the presence of the atom in a condensed medium. EXBACK produces a file, which can then be analysed by the main data analysis programme EXCURV92.

EXCURV92 essentially fits the data to the EXAFS expression given in equation I.5. The procedure is an iterative one where a model of the environment of the target atom is set up and then the parameters in the model are iterated until a best-fit is obtained. The first step in the fitting is to define the local environment of the target atom in terms of the number of shells, i, the number of atoms in the shell, N_i, the type of atom in the shell, T_i, the distance from the target atom to the shell, R_i, and the Debye-Waller factor, A_i, of the shell. The phase shifts are calculated theoretically by EXCURV92. The model is then used by the programme to calculate a theoretical $\chi(k)$. The difference between this value and experimental $\chi(k)$ is compared by a simple addition of the differences (experimental $\chi(k)$ – theoretical $\chi(k)$) at each data point in k. This difference is referred to as the R-factor, i.e. for n data points R is given by

$$R_{EXAFS} = \sum_{i}^{n} (\sigma_i \left| \chi_i^{experiment}(k.) - \chi_i^{theory}(k) \right|)^{-1} \times 100\% \qquad \textbf{(I.6)}$$

where

$$\left(\frac{1}{\sigma_i}\right) = \frac{k(i)^n}{\sum_j k(j)^n \left|exp(\quad j)\right| \quad|} \qquad \text{(I.7)}$$

The model parameters N_i, A_i, R_i, and the start of the EXAFS, E_o, are then iterated, either singly or as sets, to produce the minimum R-factor using a multiple regression routine. Clearly a reasonable starting model for the fitting is essential, but this was not a problem with the simple oxides used in the present work. It is important to note that it is the normalised EXAFS that is fitted, not the Fourier transform. EXCURV92 produces a Fourier transform and the experimental and theoretical curves can be compared. The Fourier transform gives a very useful visual comparison of the model and the experiment but it is not the basis of the analysis.

I.5.c DSC

Differential scanning calorimetry, DSC, provides a rapid method of studying thermal transitions in materials and there are several commercial systems available (Turi, 1997). A schematic diagram of the essential components of a DSC is shown in Figure I.12. The principle of the technique is essentially very simple and is best explained by outlining the experimental procedure.

The central unit of a DSC consists of two platinum cups, typically 10mm in diameter and 5mm deep. Each cup is fitted with a heater and a thermocouple and the two cups are thermally insulated and covered with a heat shield. A small amount of the sample to be studied, usually a few mg, is pressure sealed into a sample pan. The pans are usually made of very thin aluminium sheet. The pan is then placed in one of the

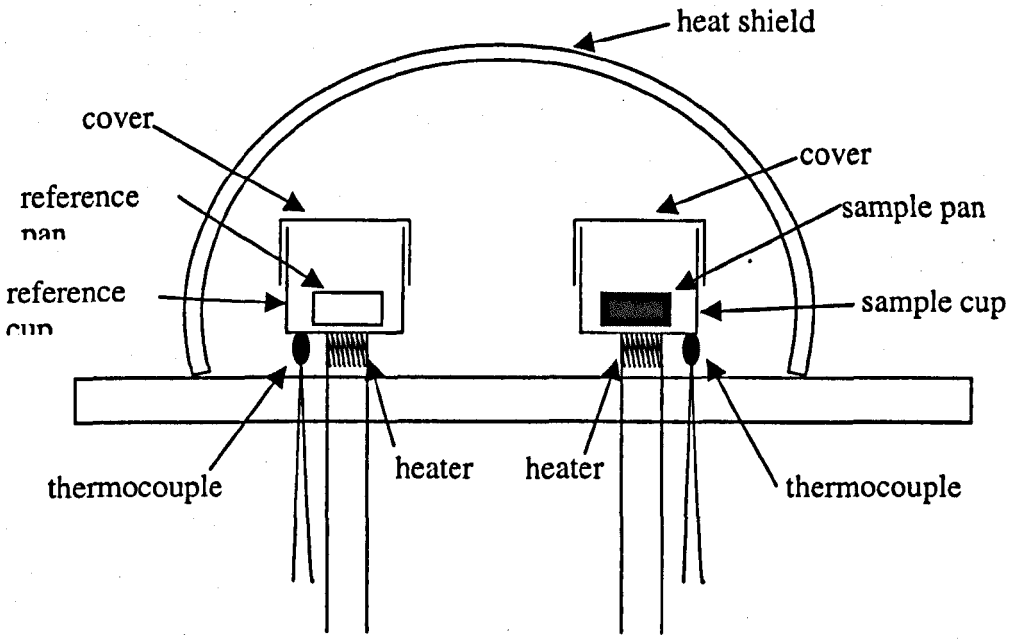

Figure I.12: A sketch of the essential features of a DSC apparatus.

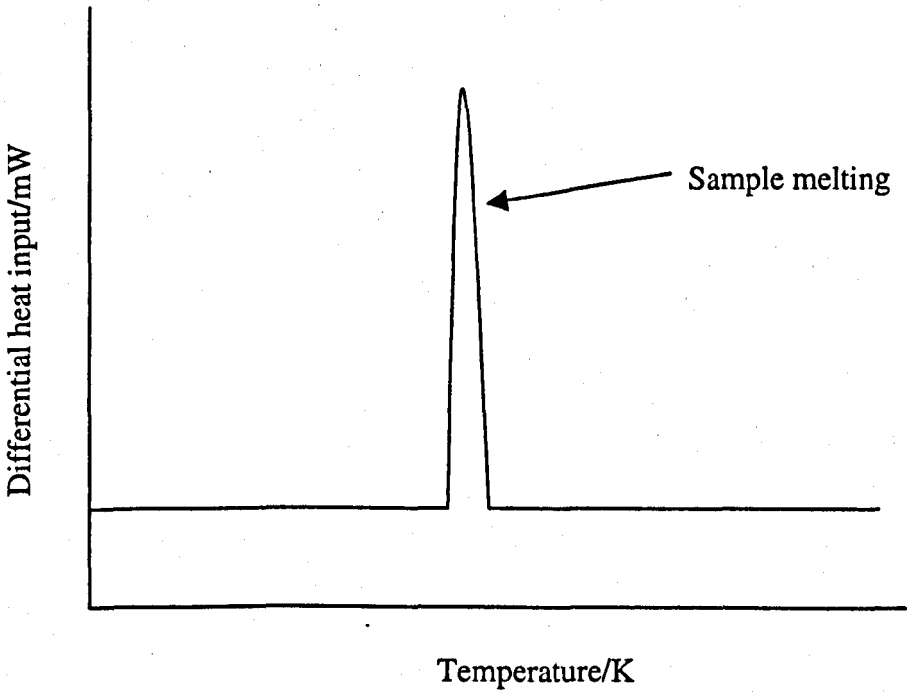

Figure I.12: A sketch of the DSC output for a solid sample.

platinum cups and covered to prevent heat loss. A reference sample, usually an empty pan, is placed in the second cup and covered. The heat shield is placed over the cups and if the sample is reactive or liable to oxidation nitrogen gas is flushed through the heat shield. The system is then ready to collect data.

The associated electronics and control computer allow the two cups to be heated simultaneously at a given rate. The electronics ensures that the two cups are always at exactly the same temperature. In addition, the electronics measures the electrical input into each of the heaters. The output, displayed on the screen of the control computer, is a plot of the difference in heat input to the two cups versus the temperature of the cups. Clearly in the absence of any thermal transitions this will be a straight line. If a transition occurs in the sample, such as melting, extra heat has to be supplied to the sample cup to counteract the latent heat of fusion giving a peak in the plot. A sketch of a typical DSC plot for a melting transition is shown in Figure I.13. The area under the peak is the latent heat of fusion for the sample.

In principle DSC measurements can yield a great deal of information on thermal transitions, e.g. transition temperatures and latent heats, and are widely used to study melting transitions and glass transitions. The measurements are rapid and very useful in testing materials, however accurate measurements require careful calibration of the system, as they are dynamic measurements. For example for the observed melting point depends on the heating rate. Thus the system has to be calibrated by measuring the melting points of standards, e.g. pure metals, at the same heating rate that is used for the sample. The original objective was to study phase transitions in the nanocrystalline oxides, specifically the transition on heating of the zirconium-aluminium alkoxide systems to form zirconia. As will be seen later in Section III.3 this occurs well above 600^0C, the upper temperature limit of the DSC using aluminium pans. Thus these measurements were not pursued.

II EXPERIMENTAL

II.1 MATERIALS PREPARATION

II.1.a Raw materials

A wide range of chemicals was used to synthesise the nanocrystalline samples. These were purchased from Aldrich and the details are given in the appropriate sections. Four types of porous silica were used to encapsulate the nanocrystals and their description is given here as the specifications are given here to simplify the later sections.

The largest pore material was obtained from Reatec GmbH (Ahornweg 6, 64331 Weiterstadt, Germany). This company produces a range of porous silicas with a large variety of pore sizes. The samples used in this work had a specified pore diameter of 126 nm and a total surface area of 40.92 $m^2 g^{-1}$. The pore volume was reported to be 1.309 $cm^3 g^{-1}$. It is worth noting that the relationship between pore volume and surface area is:-

$$Pore\ volume = \frac{Pore\ diameter \times Surface\ area}{4} \qquad \text{(II.1)}$$

Three types of silica with smaller pores were used in this study. These were all purchased from Aldrich and they were designated Silica gel, Merck. They had pore diameters of 4 nm (catalogue number 40,356-3, surface area 750 $m^2 g^{-1}$), 6 nm (catalogue 40,359-8, surface area 550 $m^2 g^{-1}$) and 10 nm (catalogue 40,360-1, surface area 300 $m^2 g^{-1}$). The pore volume was roughly constant at 0.75 $cm^3 g^{-1}$.

Later in the thesis the silica samples will only be referred to by their pore diameter.

II.1.b General procedures

Several methods have been used in the literature to prepare nanocrystalline materials and these have been outline in Chapter I. The general method that was used for the work in this thesis was to prepare a hydroxide of the metal and then to calcine this to form the oxide. A number of methods were used to produce the hydroxide, including precipitation with ammonia and hydrolysis of a metal alkoxide, often referred to as a sol-gel route. Variations of these procedures were then adapted to produce the confined nanocrystals. The general methods will be outlined first and then the detailed procedure for each system studied will be described.

The preparation of the oxides from the hydroxides is very simple. An aqueous solution is prepared from a soluble salt of the metal and the hydroxide is precipitated by the addition of ammonia.

$$MX + NH_4OH \rightarrow MOH + NH_4X \qquad \textbf{(II.2)}$$

It is worth noting that it often requires many washings with distilled water to remove the ammonium salt. The calcining usually requires about 500°C to produce the oxide.

$$2MOH \rightarrow M_2O + H_2O \qquad \textbf{(II.3)}$$

In many cases this method is not completely satisfactory as traces of hydroxylated species will be retained in the sample, as has been found for zirconia (Chadwick et al, 2001).

In many cases the preparation of the hydroxide via the alkoxide is preferred, as this tends to produce smaller nanocrystals. The general equation is given by

$$M(OR) + H_2O \rightarrow MOH + ROH \qquad \textbf{(II.4)}$$

In some cases the hydrolysis is not complete, for example with magnesium methoxide, and the reaction is then

$$M(OR)_2 + H_2O \rightarrow M(OR)OH + ROH \qquad \text{(II.5)}$$

The hydroxides (or alkoxide-hydroxides) produced from the alkoxides have a more 'open' structure, and this is why they produce smaller nanocrystals (Klabunde et al, 1996).

II.1.c Nanocrystalline alumina

Alumina was used to restrict the growth of nanocrystalline oxides. As part of the work a brief investigation was made of alumina. It was prepared by hydrolysing the alkoxide to form the hydroxide and then calcining to the oxide.

20 ml of aluminium tri *sec* butoxide ($Al[C_2H_5CH(CH_3)O]_3$) were measured from the manufacturer's bottle (Aldrich) into a small vial inside a glove box. The liquid is very viscous and the operation was performed with a measuring cylinder rather than a syringe. The vial was removed from the glove box, the material poured into a beaker and hydrolysed by the simple addition of distilled water with constant stirring. A gel formed initially and this turned into a white precipitate with excess water. The solid was filtered off and dried overnight in an oven at 100°C. This produces boehmite, AlO(OH). Calcining this at 1200°C produces α-alumina, however lower temperature calcination will produce other forms of alumina. The calcination and the products will be discussed in Chapter III.

II.1.d Nanocrystalline MgO

II.1.d.1 *Pure MgO*

The preparation of pure nanocrystalline MgO described by Chadwick et al., (1998) was repeated as part of the work to provide standard samples. 50 ml of commercial $Mg(OCH_3)_2$, a 70% solution in methanol (Aldrich), was dispensed into a 250 ml bottle in a glove box. The bottle was removed from the glove box, a magnetic flea was added and the bottle placed on a magnetic stirrer plate. The liquid was stirred and water was added drop-wise. A gel was formed which was allowed to dry in air. The sample was tended to form a cake, which was broken up with a spatula. Previous work (Rywak et. al 1995, Utamapanya et .al., 1991) had shown that the product from this procedure is $Mg(OH)(OCH_3)$, and this was confirmed by XRPD in this study (see Chapter III). Calcining the material produced nanocrystalline MgO, the particle size depending on the temperature employed.

MgO was also produced by calcining $Mg(OH)_2$ at 500°C but this did not produce nanocrystalline material.

II.1.d.2 *Nanocrystalline MgO in porous silicas*

The first attempts at producing nanocrystalline MgO in silica were based on the method of Barrer (1958,1983) which involves filling the pores with the metal nitrate hydrate and then calcining to form the oxide. The silicas were mixed in a Pyrex beaker with an appropriate amount of the nitrate necessary to give the desired fraction of pore filling, e.g. ¼, ½, etc. The fraction was always kept less than 1 so that all the salt was taken up in the pores and none remained on the surface. The beaker was then placed in an oven at 100°C (the m.p. of the hydrate is 89°C) and left for three hours. This yielded a dry silica powder indicating that the salt was in the pores. The sample was then

heated to 300°C to form the oxide. Two different silicas were used with pore sizes 6 and 10 nm. However, the XRPD patterns for all the samples showed no lines due to MgO. A closer examination of the calculations on pore filling provided the explanation of the negative result.

There is a considerable mass loss in converting $Mg(NO_3)_2.6H_2O$ to MgO and a large increase in the density. The net result is that a very small amount of MgO is formed in the pores and this would only leave a thin (0.1 nm) coating inside the pores. Thus there is very little MgO formed inside the pores. In an attempt to overcome this problem a sample was prepared with silica which had larger pores, i.e. 126 nm. This strategy was successful in producing MgO inside the pores, however, the particle size was 35 nm. Therefore the silica is not confining the MgO to nanocrystal formation. It should be noted that simply heating $Mg(NO_3)_2.6H_2O$ does not produce nanocrystalline MgO.

The second approach that was used was the deposit $Mg(OCH_3)_2$ from the methanol solution inside the pores of silica, decompose the methoxide with water and calcine the product. As we have shown earlier calcining $Mg(OCH_3)_2$ will produce nanocrystalline MgO on heating. Large pore volume silica, 126 nm, was used for the experiments. The sample was not easy to prepare quantitatively as the methoxide solution in methanol provided by Aldrich is not well defined (e.g stated to be approximately 70%) and the solution decomposes slowly even in a glove box. We estimated that the sample we prepared had about one half the pore volume filled with solid methoxide. The sample was calcined for 60 minutes at several temperatures. This produced nanocrystalline MgO in the pores, as will be described in Chapter III.

II.1.d.3 *Nanocrystalline MgO with alumina*

As described in the Introduction the addition of alumina to ceramics is known to pin the grain boundaries and prevent crystal growth. This has been used extensively for metal oxides, however no references were found to magnesium oxide crystals pinned with alumina.

The synthesis used was based on that described for the stabilisation of zirconia nanocrystals by Viswanath and Ramasamy (1999). 100 ml magnesium methoxide (10% solution in methanol) and 4 ml aluminium tri *sec* butoxide ($Al[C_2H_5CH(CH_3)O]_3$) were mixed together in a vial inside a glove box. The quantities used were calculated to produce approximately 5 g of MgO containing 15% by weight of Al_2O_3 (equivalent to 14% by volume). Aluminium tri *sec* butoxide ($Al[C_2H_5CH(CH_3)O]_3$) is very viscous and a few millilitres of propanol were added to ensure thorough mixing of the two alkoxides. The vial was removed from the glove box and excess water was added to decompose the alkoxides. The white solid was filtered off and dried in an oven at 100°C. The sample was then heated at a series of temperatures for 60 minutes. It will be shown in Chapter III that the procedure produced nanocrystalline MgO.

II.1.e Nanocrystalline zirconia

II.1.e.1 *Pure zirconia*

Several routes can be used to prepare zirconia. The simplest is to add aqueous ammonia to a solution of a zirconyl salt, usually the chloride or the sulphate (Liu et al, 1995). This produces a precipitate of zirconium hydroxide, which is often referred to as $Zr(OH)_4$. However, the precipitate is actually more complex and consists of a variety of zirconyl species, the exact nature depending on the pH of the solution (Turillas 1995). The hydroxide is amorphous and is converted to the oxide by calcining at 500°C or

higher. The product depends on annealing time and temperature. For example, heating for 60 minutes at 500°C produces particles of about 10 nm size in the tetragonal form (Liu et al, 1995). On further heating the particles grow and when they reach 30-40 nm they transform to the monoclinic structure. However, recent work (Chadwick et al, 2001) has shown that this view of the calcination is too simplistic. Heating to 700°C is necessary to get complete conversion to zirconia. At any lower temperature there is a mixture of zirconia and hydroxylated species, which being amorphous are undetected in a XRPD pattern. These species were detected by proton NMR (Chadwick, et al 2001). Zirconia can also be prepared by treating a zirconium alkoxide with water, which forms the hydroxide, and calcining the product. The result are the same as using an inorganic salt, however the alkoxide route has the advantage of being cleaner and there is no contamination from ammonium salts.

In this work pure nanocrystalline zirconia was used only as a standard to compare with samples where the growth of the zirconia particles was restricted. A 250ml saturated solution of zirconyl chloride ($ZrOCl_2 \cdot 8H_2O$; Aldrich 98% purity) was prepared in a 500ml beaker. Concentrated ammonia (Aldrich) was added until the pH was alkaline. The precipitate, zirconium hydroxide, was washed several times with distilled water and then calcined at various temperatures to produce zirconia. The resulting materials are discussed in Chapter III.

II.1.e.2 *Nanocrystalline ZrO_2 in porous silicas*

Attempts were made to deposit zirconia in porous silica by mixing zirconyl chloride with the silica and then calcining. As with the MgO the XRPD results showed that there was no detectable zirconia in the samples. Another approach that was tested was to deposit zirconium hydroxide inside the silica pores. The procedure used was to

place the silica in an aqueous solution of zirconyl chloride and urea and boil the solution overnight. This procedure is used to deposit oxide on catalyst supports. At 100°C the urea decomposes to form ammonia which in turn precipitates out the metal hydroxide. The sample is then calcined to form the oxide. However, this failed to produce any zirconia in the silica, as judged from the XRPD.

Since the deposition of magnesium methoxide inside silica had yielded nanocrystalline MgO a similar procedure was adapted for zirconia. Zirconium propoxide in 1-propanol (70% w/w solution from Aldrich) was added to the porous silica and the propanol allowed to evaporate from the sample. This was performed in a glove box. The sample was then removed from the glove box and water added to form the hydroxide. The sample was then calcined to form the oxide. This was performed by heating for 60 minutes at several temperatures. This method was used to prepare samples using 10nm and 126nm pore size silica. The aim was to produce zirconia only inside the pores. The pore volume was known, and based on the concentration of the zirconium propoxide solution and the density of solid zirconium propoxide, the amount added to the silicas was calculated to half or completely fill the pores. The calculation of the fraction of pore volume filled was calculated from the equation

$$Fraction\ filled = \frac{(V\ ZP\ soln)\times(\rho\ ZP\ solid)\times(conc\ of\ ZP\ soln[w/w])}{(\rho\ ZP\ solid)\times(pore\ volume)} \qquad \textbf{(II.6)}$$

Where ρ is the density and ZP is zirconium propoxide.

Calcination to zirconia will result in a mass loss and therefore there should only be zirconia inside the pores. The results of the calcining are discussed in Chapter III.

II.1.e.3 *Nanocrystalline zirconia with alumina*

Several groups have stabilised nanocrystalline zirconia by adding small amounts of alumina. The synthesis used was based on that described by Viswanath and Ramasamy (1999). These workers prepared the alkoxides *in situ* from inorganic salts and glycols. As the alkoxides are readily available from commercial sources it is simpler to mix the alkoxides directly. In this work the appropriate quantities of zirconium propoxide (70% solution in 1-propanol, Aldrich) were mixed with aluminium tri *sec* butoxide ($Al[C_2H_5CH(CH_3)O]_3$, Aldrich) in a glove box and then hydrolysed the mixture with water. Three samples were prepared with the alkoxide ratios aimed at producing nominally 5, 10 and 15% by weight of Al_2O_3 (equivalent to 7, 14 and 21% by volume, respectively) in the final sample. As an example, 1 ml aluminium tri *sec* butoxide mixed with 5 ml zirconium propoxide solution produces 1.5 g zirconia with 15% by weight alumina. The hydrolysed materials were calcined to produce the oxide. The results of the calcining are discussed in Chapter III.

II.1.f Nanocrystalline ceria

II.1.f.1 *Pure nanocrystalline ceria*

As with zirconia several routes can be used to prepare ceria. The simplest is to add aqueous ammonia to a solution of a cerium salt, usually the sulphate. This produces a precipitate of cerium hydroxide, which is $Ce(OH)_3$, which is then calcined to the oxide (Hirano and Kato, 1996; Nachimuthu et al, 2000).

In this work cerium hydroxide was precipitated by adding ammonia solution (Aldrich) to an aqueous solution of cerium (IV) sulphate tetrahydrate (Aldrich, >98% purity), the pH adjusted to 9.0 and the system left to age for 7 days at room temperature.

The precipitate was then washed and dried and calcined to the oxide. Calcining was performed for 360 minutes at 150, 400, 600 and 800°C to produce ceria. The results are discussed in Chapter III.

II.1.f.2 *Nanocrystalline ceria in porous silicas*

The approach that was successfully used to deposit cerium hydroxide inside the silica pores was the slow deposition created by the decomposition of urea. The procedure was attempted for preparing zirconia in silica pores but in that case it failed.

The porous silica was added to an aqueous solution of cerium (IV) sulphate tetrahydrate. The concentration of the solution was such that complete decomposition to the hydroxide would completely fill the pores. Urea (Aldrich, 99% purity) was added to the solution, sufficient to produce an excess of ammonia compared to the cerium salt, and the solution refluxed overnight. The next morning the silica was filtered and dried. The dried powder was then calcined for 60 minutes at a series of temperatures.

Two series of samples were prepared using 4 and 10 nm pore silica. The samples were calcined at a series of temperatures from 500 to 1000°C. The results are discussed in Chapter III.

II.1.g Nanocrystalline tin oxide

II.1.g.1 *Pure nanocrystalline tin oxide*

Nanocrystalline tin oxide can be prepared by several routes and the method used to prepare the samples in this work involved precipitation from an aqueous solution of tin chloride pentahydrate by the addition of aqueous ammonia [26,27]. Tin chloride pentahydrate, $SnCl_4.5H_2O$ (Aldrich) was dissolved in distilled water and aqueous ammonia added with constant stirring. A white precipitate rapidly formed and the

addition of ammonia was stopped when the pH of the solution became alkaline. Previous work (Davis, 1997) had shown that extensive washing with dilute nitric acid was required to remove the ammonium chloride from the precipitate. In this work the washing was continued until the washings showed no trace of chloride ion, as tested by silver nitrate solution. The powder was then dried overnight in an oven at 100°C. The particle size, as estimated from the XRPD peaks in the work of Davis was 2 to3 nm.

The sample was then calcined for 60 minutes at several temperatures up to 1000°C. The results are discussed in Chapter III.

II.1.g.2 *Nanocrystalline SnO_2 in porous silicas*

The approach that was successfully used to deposit tin oxide inside the silica pores was the slow deposition created by the decomposition of urea.

The porous silica, 10 nm pore size, was added to an aqueous solution of tin (IV) chloride pentahydrate (Aldrich). Two concentrations of the solution were employed. The first was such that complete decomposition to the oxide would completely fill the pores. A second concentration was chosen that would half fill the pores with oxide. Urea was added to the solution, sufficient to produce an excess of ammonia compared to the cerium salt, and the solution refluxed overnight. The next morning the silica was filtered and dried. The dried powder was then calcined for 60 minutes at a series of temperatures. The results are discussed in Chapter III.

II.1.g.3 *Nanocrystalline SnO_2 with alumina*

The success of stabilising zirconia and magnesia nanocrystals by the addition of alumina indicated this could also be a means of stabilising tin oxide nanocrystals. However, for tin oxide the alkoxide pre-cursors are very expensive and unstable. Thus it was decided add the aluminium alkoxide to the pre-formed tin oxide nanocrystals.

Nanocrystalline tin oxide, 5g of the material prepared in Chpater II.1.g.1 was mixed with 5 ml of dried propanol in a 15 ml plastic vial. This was undertaken in a glove box. 0.75 ml of aluminium tri *sec* butoxide ($Al[C_2H_5CH(CH_3)O]_3$) (Aldrich) were then added to the vial, the operation again being performed in the glove box. The vial was thoroughly shaken, removed from the glove box and distilled water was added to hydrolyse the alkoxide. The water and alcohol were decanted off and the sample dried overnight at 100°C. The sample was estimated to contain nominally 3% by weight of Al_2O_3 (equivalent to 5% by volume). Samples were calcined for 60 minutes at a series of temperatures up to 1000°C and the results are discussed in Chapter III.

II.1.g.4 *Nanocrystalline SnO_2 with HMDS*

Wu et al (1999) stabilised a number of nanocrystalline metal oxides (SnO_2, TiO_2 and ZrO_2) by treating them with hexamethyldisilazane, HMDS. The structure of this compound is shown below.

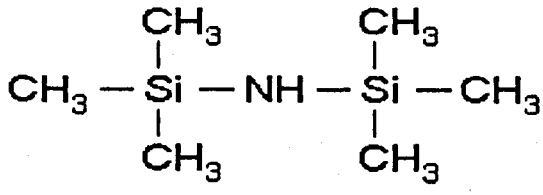

The authors assumed that the compound reacted with surface hydroxyl groups on the oxides to produce surface siloxyl groups (- $O\text{-}Si(CH_3)_3$). The coated surface was

reported to prevent the growth of the crystallites, however in the original work the samples were only heated to 500°C.

In the present work 5g of nanocrystalline tin oxide were placed in a screw-cap plastic vial with 2 ml dried 1-propanol. 0.75ml of HMDS (Aldrich) were added to the vial, the operation being performed in a glove box (HMDS is moisture sensitive). The vial became warm to the hand, suggesting there was some reaction of the HMDS. The sample was then left for three days at room temperature. After this period the vial was removed to a fume cupboard, the stopper removed and the excess HMDS and propanol allowed to evaporate. The sample was then dried at 100°C overnight. The sample was then calcined at several temperatures and the results are discussed in Chapter III.

II.1.h Summary of the samples prepared

Table II.1 summarises all the samples that were prepared for the calcination experiments that will be discussed in Chapter III.

Table II.1

Nanocrystal metal oxide sample or pre-cursor	State
AlO(OH)	Pure
$Mg(OH)_2$	Pure
$Mg(OCH_3)(OH)$	Pure
$Mg(OCH_3)(OH)$	In 126 nm silica pores
$Mg(OCH_3)(OH)$	With alumina
$Zr(OH)_4$	Pure
$Zr(OH)_4$	In 10 nm silica pores
$Zr(OH)_4$	In 126 nm silica pores
$Zr(OH)_4$	With alumina
CeO_2	Pure
CeO_2	In 4 nm silica pores
CeO_2	In 10 nm silica pores
SnO_2	Pure
SnO_2	In 10 nm silica pores
SnO_2	With alumina
SnO_2	With HMDS

II.2 CHARACTERISATION METHODS

II.2.a X-ray diffraction

Xray powder diffraction patterns were collected with both a laboratory source and at the Daresbury SRS on station 9.3. The later experiments will be described in the section on the EXAFS experiments. The laboratory diffractometer was a Phillips PW1720 instrument using a Cu K_α tube operating at 35 kV and 20 mA. This was supplied by Hiltonbrook Ltd and was controlled by the Siehilt software (Diffraction Technology Pty) operating on a Pentium based PC. The geometry was the conventional θ-2θ arrangement, as described in Section I. The powder samples were pressed into 'open' cavities (10 wide × 15 long × 1 mm deep) in aluminium holders. The backing of the cavities was a piece of Sellotape. For very small samples a Perspex holder with a smaller cavity (10 mm diameter × 0.5 mm deep) was employed. This holder had the disadvantage that it gave a broad background up to ~ 25° due to scattering from the Perspex. Diffraction scans were usually collected for 2θ from 20 to 70° with a step size of 0.02° and a scan speed of 1° per minute. When high-resolution results were required several scans were collected overnight and averaged. The patterns were analysed with the programme Trace V.3 (Diffraction Technology, Pty). This contained a library of spectra for sample identification and routines for background subtraction and estimation of the particle size.

Trace V.3 employed the Scherrer equation to determine the particle size, s, in the form

$$s = \frac{k\lambda}{\beta \cos\theta} \qquad \text{(II.7)}$$

with k = 0.89 (see Section I.5.a). The instrumental broadening was determined by collecting patterns for samples of sodium chloride and potassium chloride which had been ground in a mortar and pestle, i.e. particle sizes around 20 microns. The peaks were assumed to be unaffected by particle size broadening. The width of each peak was measured and fitted to a polynomial to provide a plot of the broadening as a function of 2θ. The appropriate value of the broadening could then be applied to any given peak in a diffraction pattern of an unknown sample.

II.2.b EXAFS

EXAFS spectra were collected on station 9.3 at the Daresbury SRS. The station equipment is shown schematically in Figure II.1. Station 9.3 has been specially designed to make measurements on dilute samples and for high energy edges, with an energy range of 7-33 keV. It is on the Wiggler I source and the energy is tuned with a double crystal harmonic rejecting Si(220) monochromator of which the first crystal is water cooled. The monochromator can run in 'quick EXAFS scanning mode'. It is equipped with a 32 channel Canberra scalar solid state fluorescence detector, which allows the signal to be re-normalised for count rates up to about 85 kHz per channel. The system is basically the same as that described in Section I.5.b except that station 9.3 is also fitted with a curved Inel position sensitive detector. This detector allows the collection of XRDP patterns as well as EXAFS spectra. In addition, there is a furnace chamber around the sample which can be flushed with nitrogen and the sample can be programmable heated to 1100°C. During data collection the SRS was running at 2 GeV with an average current of 150 mA. All EXAFS data were collected with the monochromator off set to give 50% harmonic rejection, i.e. higher order wavelengths were removed from the beam to ensure that the true EXAFS were collected.

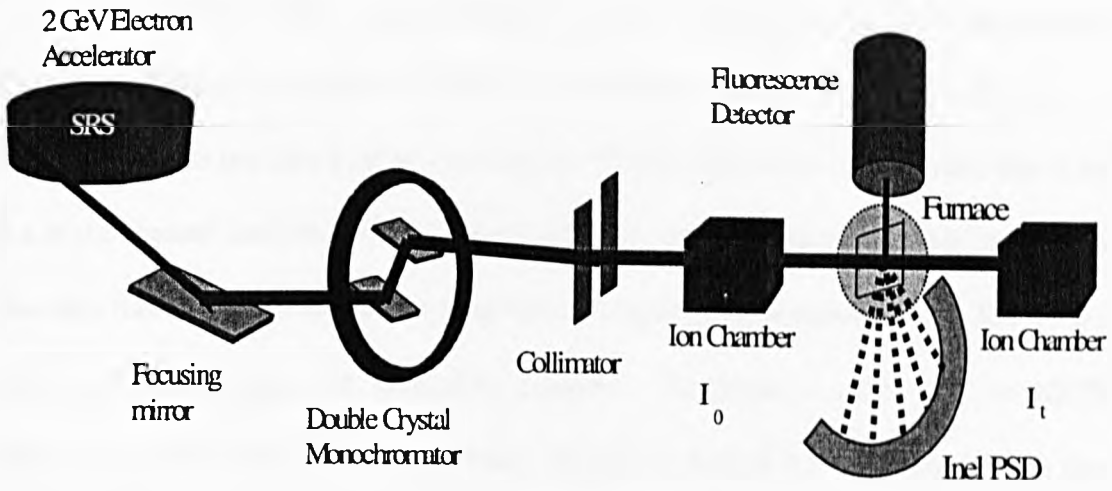

Figure II.1: Schematic representation of SRS station 9.3 experimental layout.

The basic EXAFS procedure involved sample preparation, data collection and data analysis. The sample preparation involved taking a small amount of the sample (typically ~20mg) that would produce an edge step of about 1 (see Section I.5.b). This was thoroughly mixed with an inert diluent, polythene or silica powder, and pressed into a 13mm diameter pellet in a standard IR press (Specac Ltd). Silica powder was used for samples that were heated. For measurements on samples at room temperature simultaneous scans of EXAFS and XRPD patterns were collected. Usually six scans of each were collected and averaged to improve the signal-to-noise ratio. The EXAFS scans were collected in quick scanning mode and were timed for five minutes per scan with a three-minute XRPD scan. The XRPD patterns were collected at a fixed wavelength set at the starting wavelength for the EXAFS scans. For heating runs the system was programmed to collect consecutive EXAFS scans (three minutes) and an XRPD scans (two minutes) whilst the sample was heated at 5 degrees per minute. Thus every 25°C there was an EXAFS spectrum and an XRPD pattern. For some runs spectra were collected on heating and cooling cycles.

The EXAFS data were analysed with the Daresbury suite of programmes EXCALIB, EXBACK and EXCURV92, as described in Section I.5.b. The analysis of the XRPD results requires further explanation. The Inel detector collects data that is fed to a multi-channel analyser and the output is in the form of channel number and counts. The data has to be calibrated and converted to equivalent patterns for Cu Kα so that they can be compared with laboratory patterns. To obtain a calibration an XRPD pattern was collected for a silicon standard sample on station 9.3. The pattern was then compared with the XRPD pattern for silicon collected with Cu Kα radiation on the Traces database. This allowed an identification of the Inel channel number with a 2θ angle for each diffraction peak. A least squares fit was made to these figures and a small BASIC programme was compiled to convert the Inel data for the samples into equivalent Cu Kα patterns. For the heating runs the patterns were analysed in EXCEL and displayed in 3D plots.

II.2.c DSC

Differential scanning calorimetry was performed with a commercial Perkin-Elmer DSC7 instrument and the results analysed with the associated software. The instrument was fitted with a sub ambient cooling attachment. The measurements were performed with aluminium pans. This limited the upper temperature of runs to 600°C. DSC measurements were only collected for the zirconia and zirconia with alumina samples.

III RESULTS AND DISCUSSION

In this chapter the results of the various experiments are presented and discussed. For clarity the various oxides are treated separately and a summary for all the materials is presented at the end of the chapter. A number of the experiments, for example the EXAFS and XRPD studies, produced a great deal of data and it is not feasible to present them all here. Hence, representative results are presented. For example, although all the Fourier transforms are presented, the full EXAFS are only shown for one sample of each system that has been investigated. This allows a comparative judgement of the quality of the raw EXAFS spectra.

III.1 NANOCRYSTALLINE ALUMINIUM OXIDE

The preparation of nanocrystalline aluminium oxide was not an initial objective of the project. However, the use of aluminium oxide in the stabilisation of other nanocrystalline oxides led to a brief study of this material. In order to simplify the presentation of the results for other oxides it is appropriate to describe the results of this study at the outset.

III.1.a Pure nanocrystalline aluminium oxide

The preparation of the sample was described in Section II.1.c. The XRPD pattern, shown in Figure III.1, identified the powder as-prepared as boehmite, AlO(OH) with a particle size of 3.6 nm. The sample was then heated for 60 minutes at a series of temperatures up to a final temperature of 1200°C. The aim was to estimate the temperatures at which phase transitions occurred and to determine the particle sizes after heating.

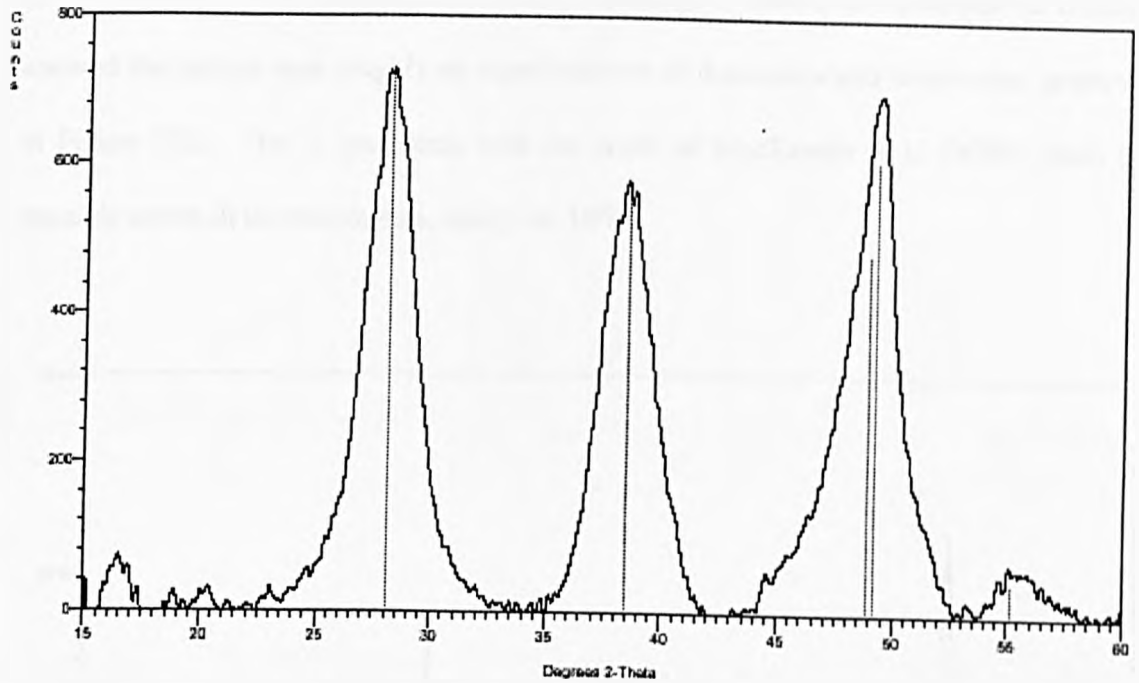

Figure III.1: The XRPD pattern for the hydrolysed and dried aluminium tri *sec* butoxide. The lines are database positions for boehmite [AlO(OH)].

An extensive study of the effect of calcining the boehmite was not undertaken. It is well known that boehmite transforms to alumina (Yang et al, 1988 and references therein) and the transformation have been extensively studied. Therefore the point of interest in the present work was the size and nature of the particles. A detailed study has been reported recently by MacKenzie et al (2000). This work showed that the dehydration of the boehmite to form alumina is complete by 500°C. The alumina formed is γ-alumina, which on heating transforms to δ-alumina and then to α-alumina. The sequence is best represented by the following scheme:-

$$AlO(OH) \rightarrow 500^{o}C \rightarrow \gamma\text{-alumina} \rightarrow \sim 1000^{o}C \rightarrow \delta\text{-alumina} \rightarrow 1195^{o}C \rightarrow \alpha\text{-alumina}$$

In the present work the boehmite sample was heated for 60 minutes at 1100°C. The XRPD pattern showed that the sample was predominantly δ-alumina, Figure III.2. The particle size was estimated as 16 nm. Heating at 1200°C for a further 90 minutes showed the sample was roughly an equal mixture of δ-alumina and α-alumina, as shown in Figure III.3. This is consistent with the work of MacKenzie et al (2000) given the possible errors in thermocouples, easily +/- 10°C.

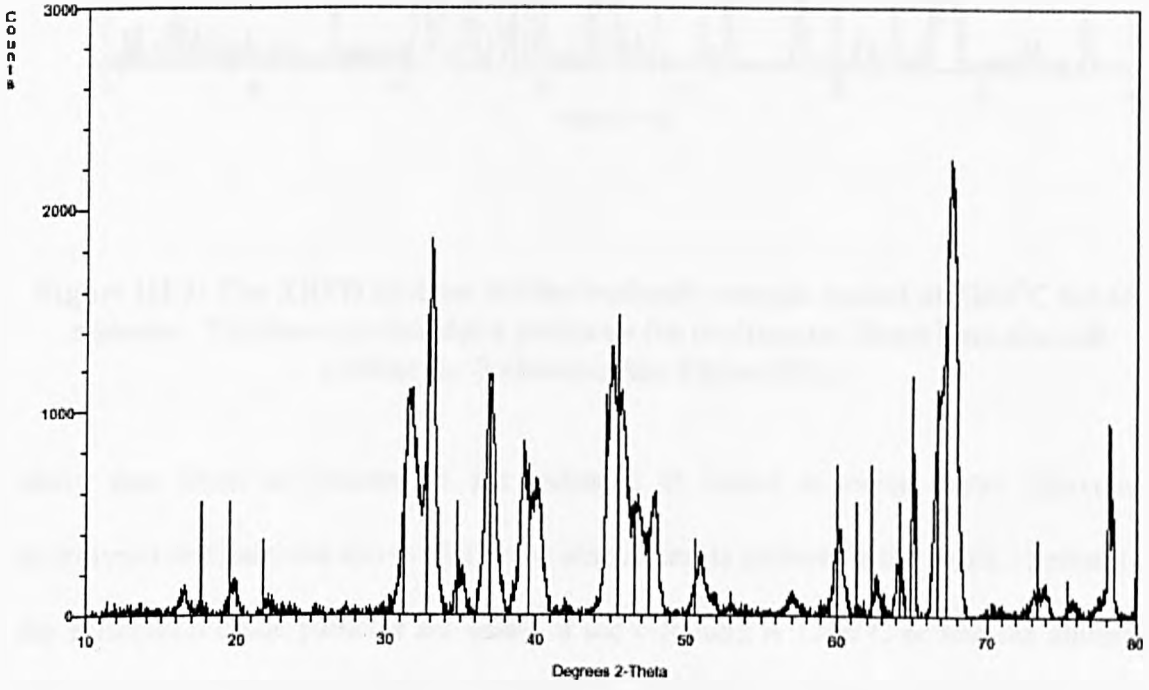

Figure III.2: The XRPD pattern for the boehmite sample heated at 1100°C for 60 minutes. The lines are database positions for δ-alumina.

In terms of the work that will be reported later in this thesis where alumina has been used to prevent the growth of other nanocrystalline oxides there are two key points. Firstly, the boehmite alone dehydrates to alumina at 500°C. Thus it seems most

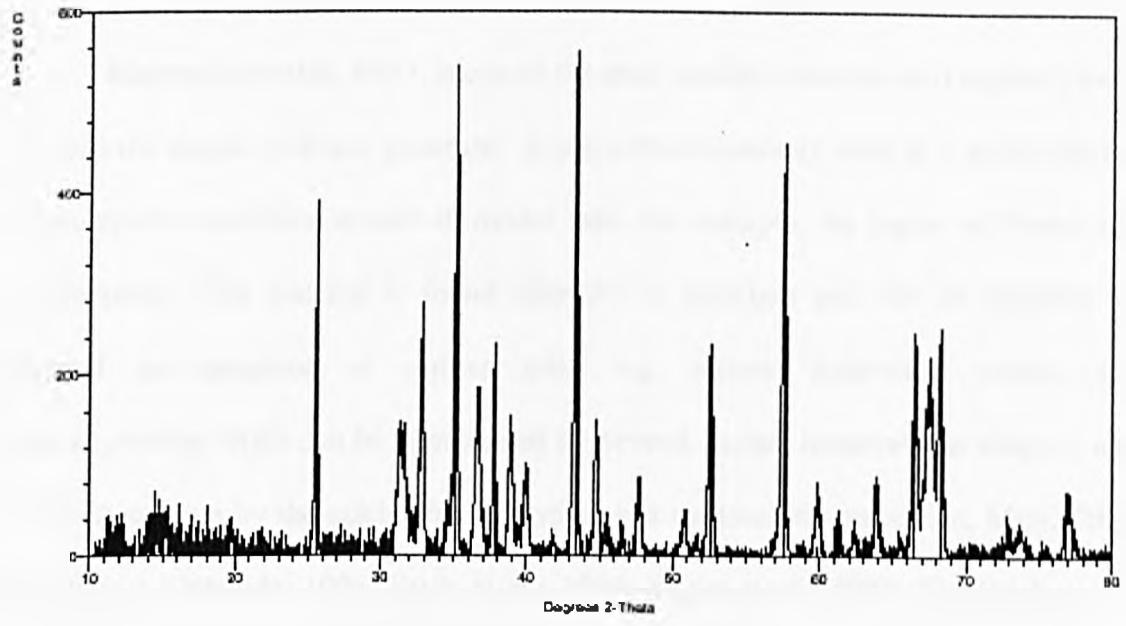

Figure III.3: The XRPD pattern for the boehmite sample heated at 1200°C for 60 minutes. The lines are database positions for α-alumina. Some lines are still evident for δ-alumina (see Figure III.2).

likely that when aluminium tri *sec* butoxide is added to other metal alkoxides, hydrolysed and calcined above 500°C the aluminium is present as the oxide. Secondly, the aluminium oxide particles are small; if the calcining is 1100°C or less the alumina particles will be 16 nm or smaller. Of course, there may be changes in the details in the calcining behaviour when there are two alkoxides and hydrolysed compounds present, but at least there are some guidelines to interpret the results.

III.2 NANOCRYSTALLINE MAGNESIUM OXIDE

Magnesium oxide, MgO, is one of the most studied materials as it is purely ionic and has the simple rock-salt structure. It has been extensively used as a model system for computer simulation studies of oxides (see, for example, the papers of Parker and co-workers). The material is found naturally as periclase and can be prepared by thermal decomposition of various salts, e.g. acetate, hydroxide, nitrate, etc. Nanocrystalline MgO can be synthesised by several routes, however the simplest and most effective is by the calcination of hydrolysed magnesium methoxide, $Mg(OCH_3)_2$ (Stark and Klabunde, 1996, Stark et al., 1996, Koper et al., 1997, Chadwick et al., 1998). One aim of this project was to prepare nanocrystals of MgO that is stable at high temperatures and the various approaches and results are presented in this section.

III.2.a Standards

The first experiments that were performed were to prepare MgO by various routes to provide standards for the studies of the confined material. The primary standard was commercial MgO obtained from BDH Ltd. The XRPD pattern for this material is shown in Figure III.4a. The pattern is very simple and the peaks match those in the Traces Search-Match database for periclase. The dominant peak is at $2\theta = 42.90^{\circ}$. Magnesium hydroxide, $Mg(OH)_2$, was used in some of the work. The sample used in this work was prepared by adding aqueous ammonia to an aqueous solution of magnesium chloride. The XRPD pattern for this material is also shown in Figure III.4b. The pattern is again simple and the peaks match those in the database for brucite. The dominant peak is at $2\theta = 38.86^{\circ}$.

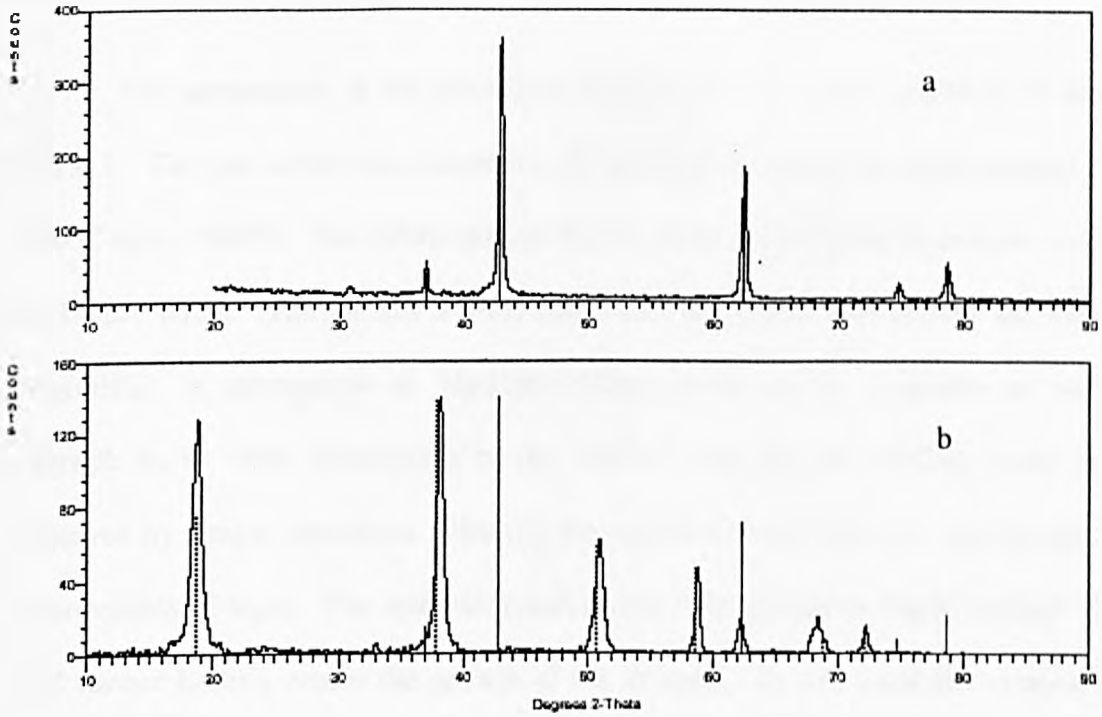

Figure III.4: The XRPD patterns for (a) magnesium oxide (BDH Ltd) and (b) magnesium hydroxide. The solid and dashed lines are database positions for magnesium oxide and magnesium hydroxide, respectively.

III.2.b Pure nanocrystalline MgO

The preparation of the pre-cursor from $Mg(OCH_3)_2$ was described in Section II.1.d.1. The pre-cursor was heated for 60 minutes at a series of temperatures; every 100°C up to 1000°C. The XRPD pattern for the dried powder after hydrolysis is shown in Figure III.5a. The pattern is interesting and the material is clearly not MgO or $Mg(OH)_2$. It corresponds to $Mg(OH)(OCH_3)$, as shown by a number of workers (Rywak et. al 1995, Utampanya et .al., 1991). The second (OCH_3) group is not removed by simple hydrolysis. Heating the material in air results in the formation of nanocrystals of MgO. The material transforms to nanocrystalline MgO at about 400°C and further heating causes the growth of the crystals. In this work the material was heated for one hour at 500°C. The XRPD pattern around the dominant peak in MgO is shown in Figure III.5b. It can be seen that the main peak is broad and corresponds to a particle size of 7.8 nm. This is consistent with the work of Chadwick et. al. (1998) who found a particle size of 5 nm after heating at 500°C for 30 minutes under vacuum.

Attempts were made to produce nanocrystalline MgO from $Mg(OH)_2$. These were not successful. Heating $Mg(OH)_2$ at moderate temperatures, e.g. 300°C, does not give full conversion to the oxide and traces of the hydroxide are always present. Higher temperatures, around 500°C are required for complete removal of hydroxide and this leads to relatively large particles of MgO. This is well demonstrated in Figure III.5c, which compares MgO prepared by heating $Mg(OH)_2$ and $Mg(OH)(OCH_3)$. The former has much sharper peaks, and the calculated particle size is ~200 nm.

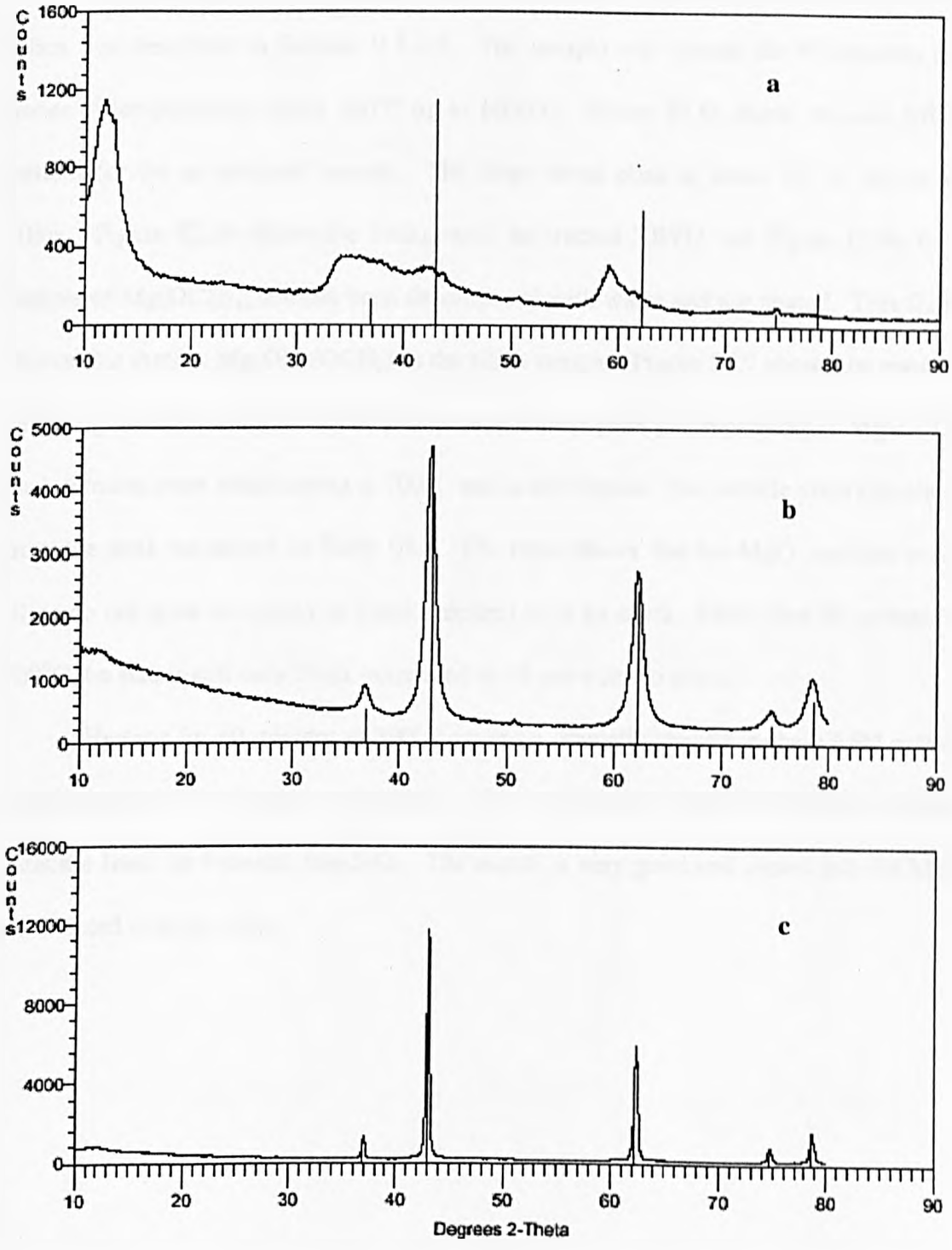

Figure III.5: The XRPD patterns for (a) hydrolysed magnesium methoxide, no heating (b) hydrolysed magnesium methoxide, after 60 minutes heating at 500°C, and (c) magnesium hydroxide, after 60 minutes heating at 500°C. The solid lines are database positions for magnesium oxide.

III.2.c Nanocrystalline MgO in porous silicas

The description of the preparation of the nanocrystalline pre-cursor in 126 nm silica was described in Section II.1.d.2. The sample was heated for 60 minutes at a series of temperatures; every 100°C up to 1000°C. Figure III.6a shows the raw XRPD pattern for the as prepared sample. The large broad peak at about 22° is due to the silica. Figure III.6b shows the background subtracted XRPD and Figure III.6c for a sample of $Mg(OCH_3)_2$ that has been decomposed with water and not heated. This figure shows that there is $Mg(OH)(OCH_3)$ in the silica sample. Figure III.7 shows the result of calcining the silica sample. At 400°C there is a clear peak corresponding to MgO. The peak remains even after heating at 700°C and is still broad. The particle sizes calculated from the peak are shown in Table III.1. The table shows that the MgO particles in the silica do not grow as rapidly as those prepared with no silica. Even after 60 minutes at 700°C the size is still only 7 nm, compared to 35 nm with no silica.

Heating for 60 minutes at 800°C caused a dramatic change in the XRPD pattern and the production of many more peaks. This is shown in Figure III.8 along with the database lines for fosterite, Mg_2SiO_4. The match is very good and shows that the MgO has reacted with the silica.

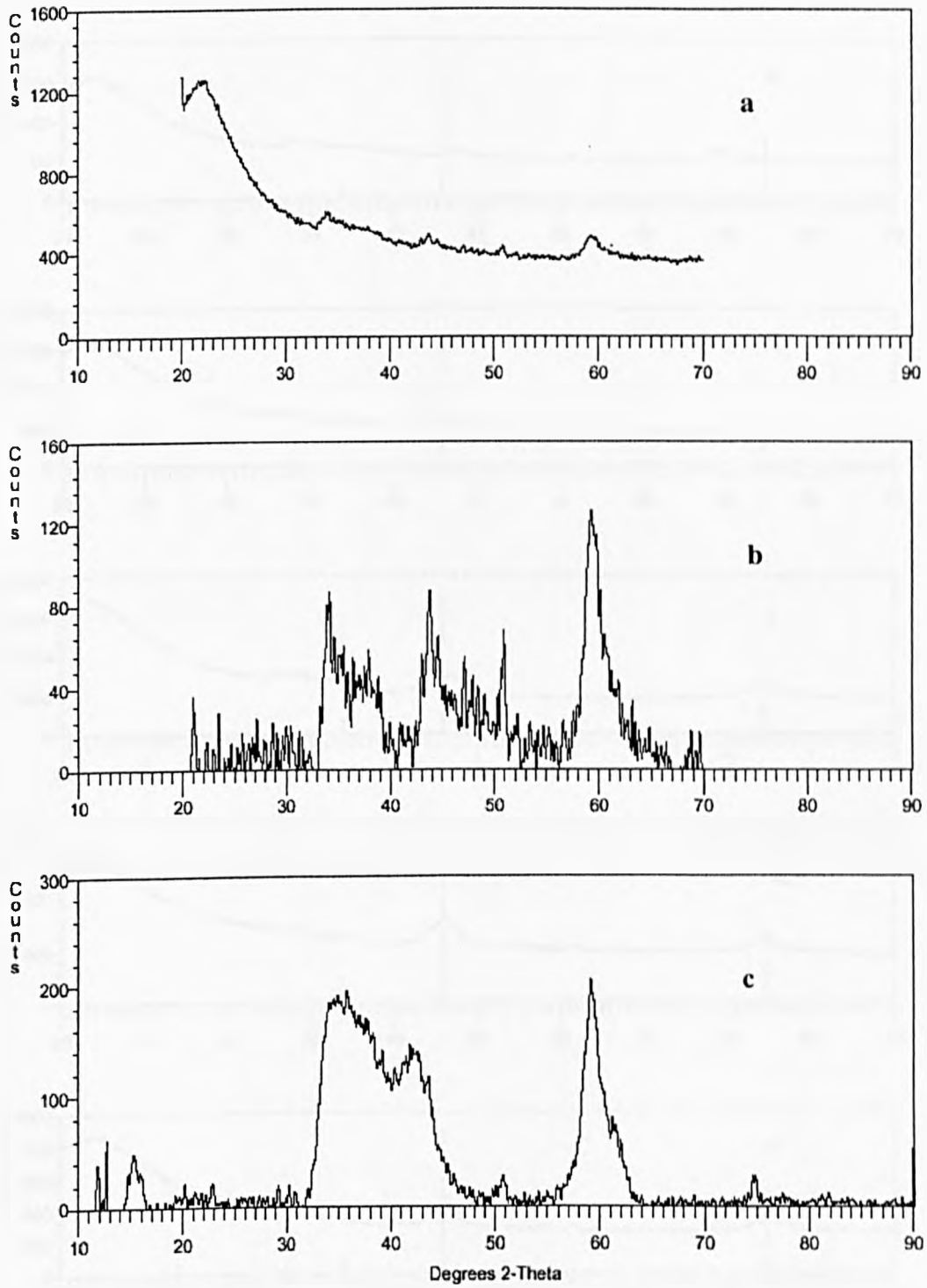

Figure III.6: The XRPD patterns for (a) hydrolysed magnesium methoxide in 126 nm pore silica, no heating, (b) pattern (a) background subtracted, and (c) hydrolysed magnesium methoxide, no heating.

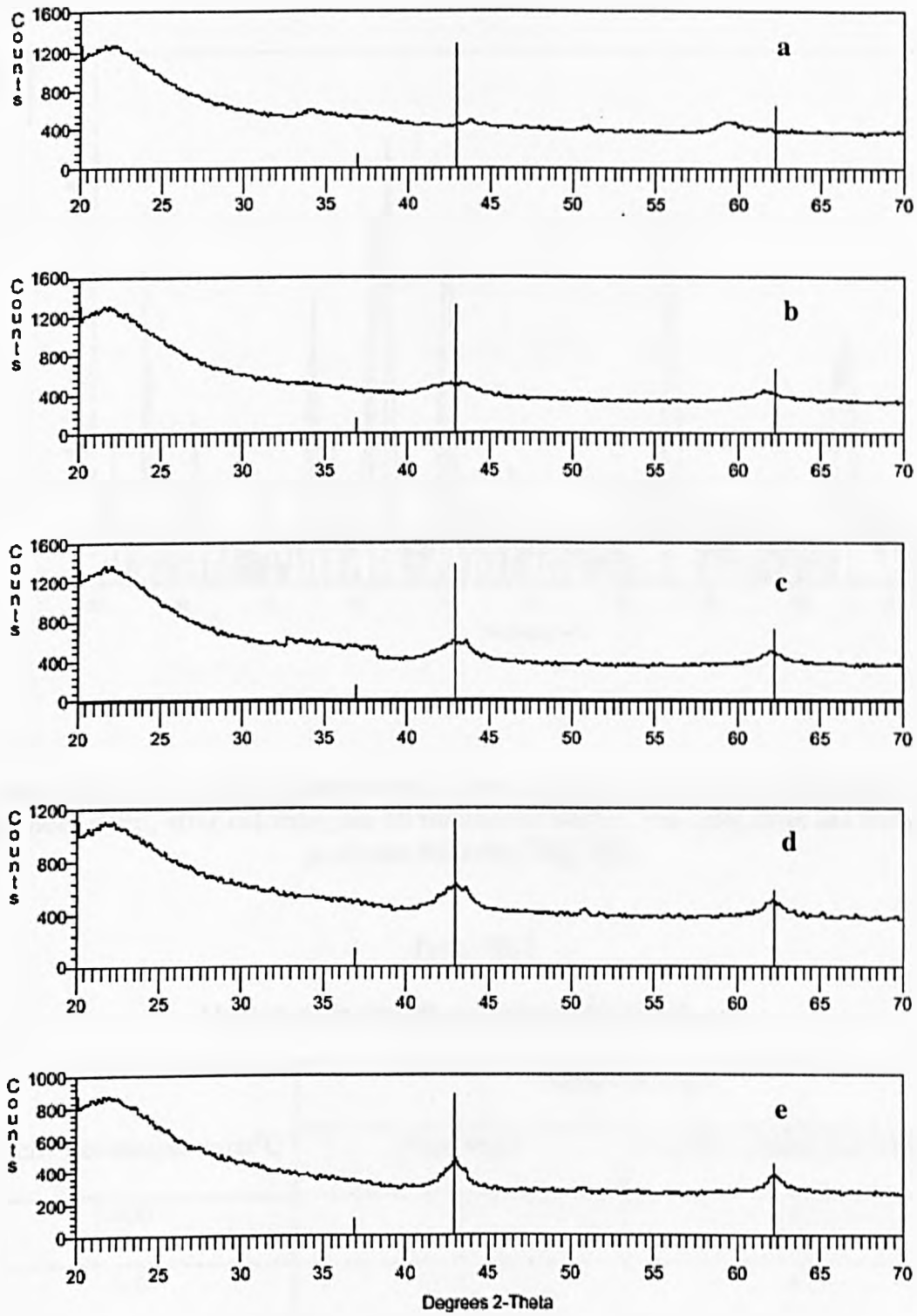

Figure III.7: The XRPD patterns for (a) hydrolysed magnesium methoxide in 126 nm pore silica, no heating, and after calcining for 60 minutes at (b) 400°C, (c) 500°C, (d) 600°C, and (e) 700°C. The solid lines are database positions for magnesium oxide.

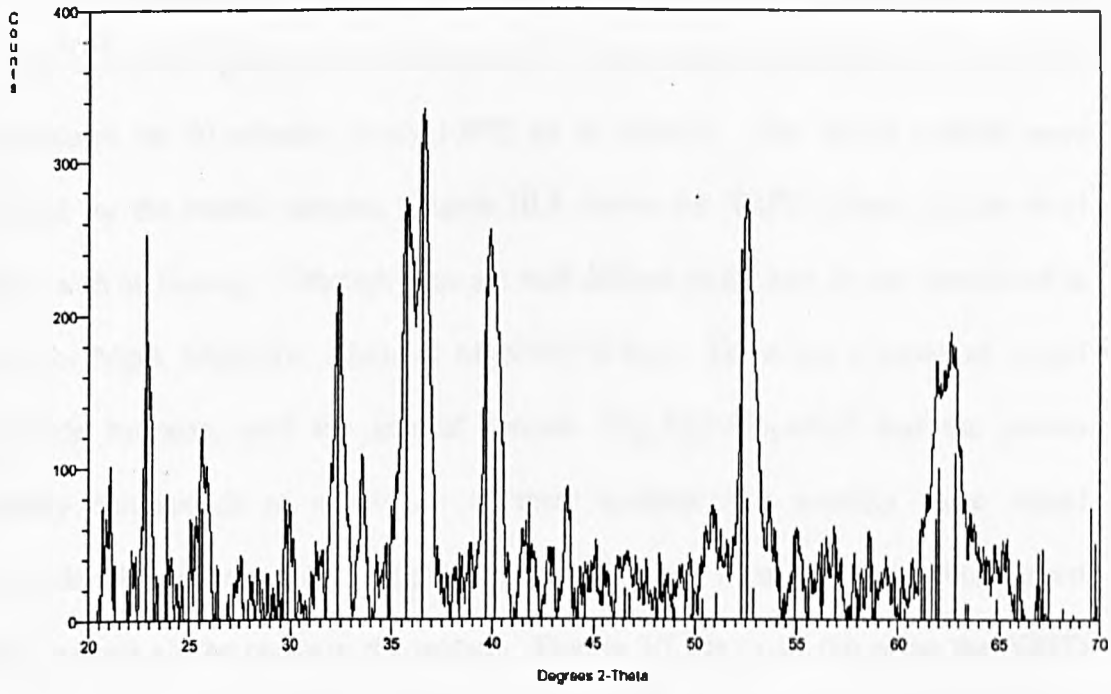

Figure III.8: The XRPD patterns for (a) hydrolysed magnesium methoxide in 126 nm pore silica, after calcining for 60 minutes at 800°C. The solid lines are database positions fosterite, Mg_2SiO_4.

Table III.1

MgO particle size after calcining for 60 minutes

Calcination temperature/°C	Particle size/nm	
	Pure MgO	MgO in 126nm pore silica
400	3	3
500	5	4
600	13	4.5
700	35	7

III.2.d Nanocrystalline MgO with alumina

The preparation involved the hydrolysis of $Mg(OCH_3)_2$ and aluminium butoxide and the details are given in Section II.1.d.3. The sample was heated at a series of temperatures for 60 minutes; every 100°C up to 1000°C. The XRPD patterns were collected for the heated samples. Figure III.9 shows the XRPD pattern for the dried sample with no heating. Although there are well defined peaks they do not correspond to peaks for MgO, $Mg(OH)_2$, Al_2O_3 or $Mg(OH)(OCH_3)$. There are a series of mixed hydroxide hydrates, with the general formula $Mg_xAl_y(OH)_z.nH_2O$ and the pattern probably corresponds to a mixture of these systems and possibly some mixed hydroxide-alkoxide materials. $MgAl(OH)_{14}.xH_2O$ gives a match to the four largest peaks, but not all the peaks in the pattern. Figures III.10a to III.10e show the XRPD patterns on subsequent heating. At 400°C it is clear that MgO has formed and that it is nanocrystalline, the particle size is very small,

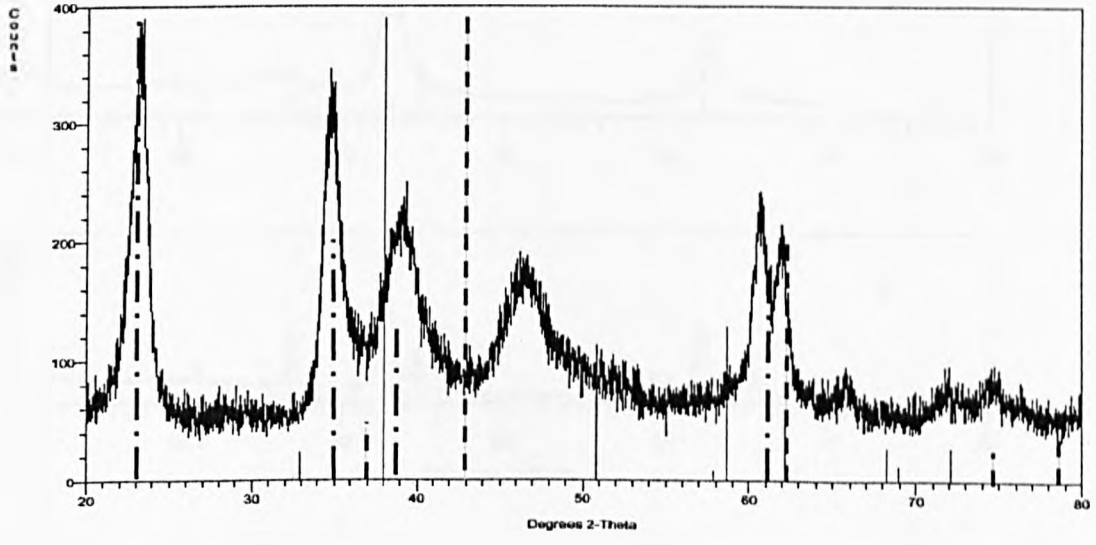

Figure III.9: The XRPD pattern for a hydrolysed mixture of magnesium methoxide and aluminium tri *sec* butoxide. The solid database positions for magnesium oxide (dashed line), and magnesium hydroxide (solid line) and $MgAl(OH)_{14}.xH_2O$ (dot and dash line) are shown.

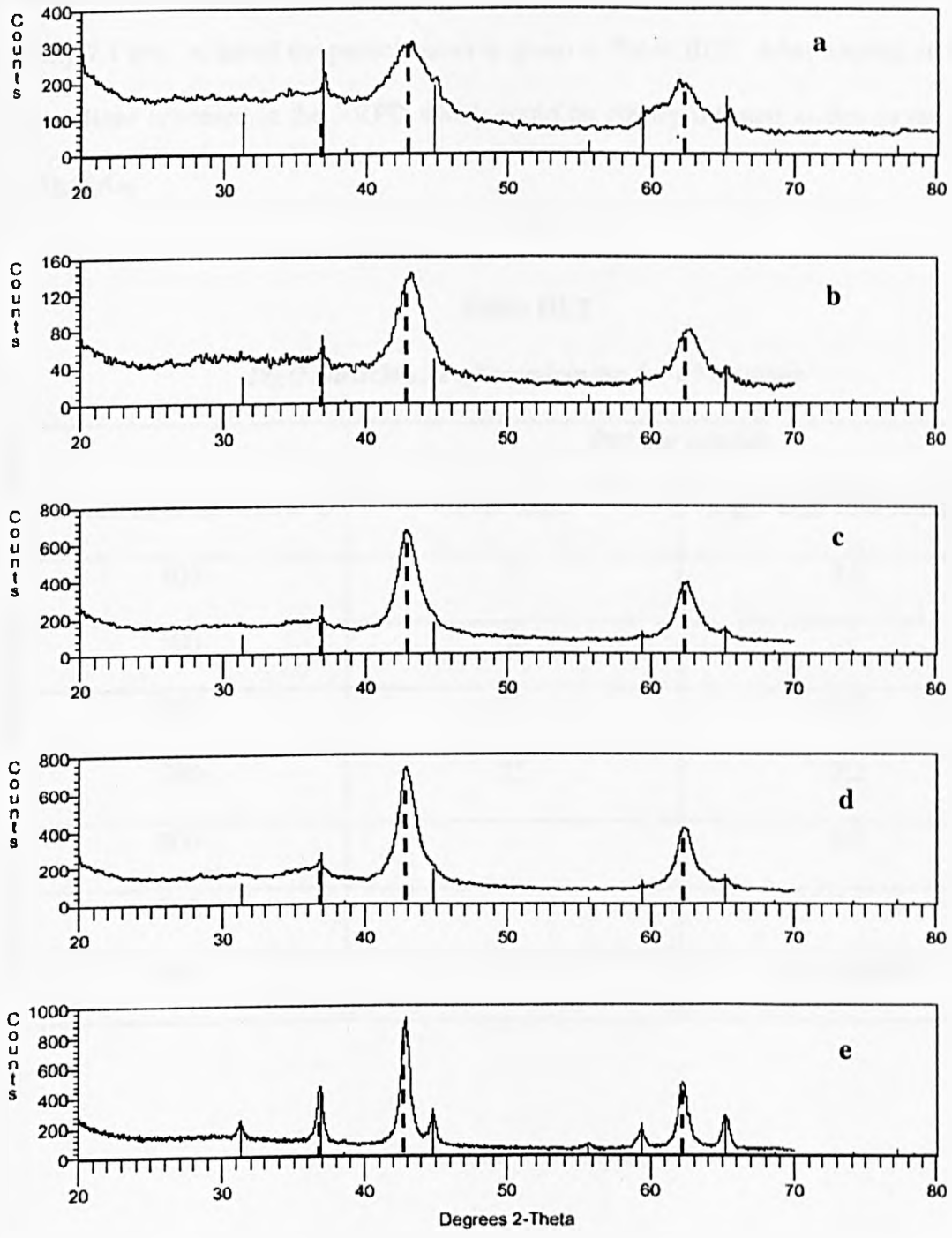

Figure III.9: The XRPD pattern for a hydrolysed mixture of magnesium methoxide and aluminium tri *sec* butoxide after calcining for 60 minutes at (a) 400°C, (b) 600°C, (c) 800°C, (d) 900°C and (e) 1000°C. The dashed lines and solid lines are database positions for magnesium oxide and spinel, $MgAl_2O_4$, respectively.

being calculated as 2.5 nm form the peak width. Subsequent heating of the sample shows only a slight narrowing and even after 60 minutes at 900°C the particle size is only 7.1 nm. A list of the particle sizes is given in Table III.2. After heating at 1000°C new lines appeared in the XRPD which could be clearly indexed as due to the spinel, $MgAl_2O_4$.

Table III.2

MgO particle size after calcining for 60 minutes

Calcination temperature/°C	Particle size/nm	
	Pure MgO	MgO with 15% Alumina
400	3	2.5
500	5	-
600	13	4.7
700	35	5.2
800	-	5.7
900	-	7.1
1000	-	18 + spinel

III.2.e Summary of the results for nanocrystalline MgO

The results for nanocrystalline MgO are basically contained in Tables III.1 and III.2. For clarity, they are shown graphically in Figure III.11. Confining the MgO in silica clearly restricts the growth of the nanocrystals. Addition of alumina to MgO, by adding together the two alkoxides, also restricts the growth of MgO. As can be seen from the figure the effect of restricting the growth is very similar in both cases up to calcining temperatures of 700°C. However, above 700°C the MgO reacts with the silica to form fosterite. The addition of alumina is effective in restricting growth up to 900°C, beyond which there is the formation of the spinel.

Thus effective methods have been developed to maintain nanocrystalline MgO at elevated temperatures and one of the objectives of the project has been achieved. From this work it appears that MgO is less reactive with alumina than silica. Therefore it would be interesting to explore the effect of depositing MgO in porous alumina.

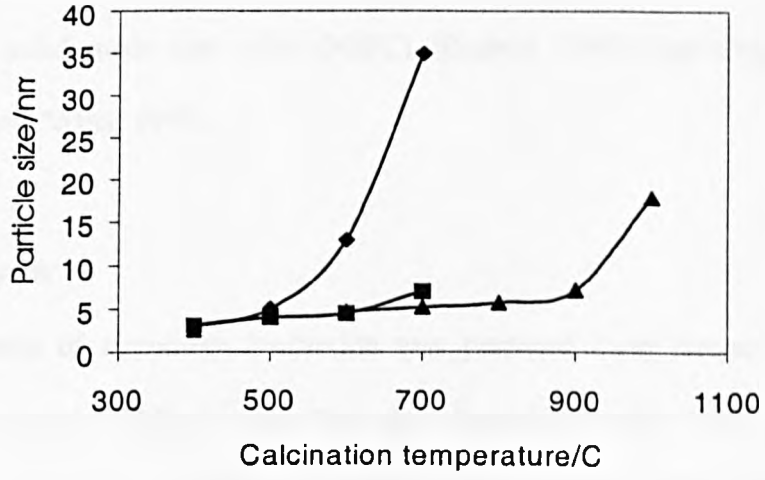

Figure III.11: The particle sizes of MgO. The results of calcining for 60 minutes at each temperature; ◆ pure MgO from methoxide, ■ MgO in 126 nm silica, ▲ MgO with 15% alumina.

III.3 NANOCRYSTALLINE ZIRCONIA

Zirconium oxide, zirconia, occurs naturally as the mineral baddeleyite which has a monoclinic structure. The phase diagram of zirconia is complex. At room temperature the stable phase is monoclinic but on heating it transforms at 1400K to the tetragonal form, and then at 2640K to a cubic, fluorite-structured phase. The addition of lower valent cationic dopants at low concentrations will stabilise the tetragonal phase and at concentration exceeding ~8 mol per cent the cubic phase is stabilised. Although the monoclinic phase is the stable room temperature phase when the material is prepared as nanocrystals (> about 30 nm particle size) other phases can form, most commonly the tetragonal form (Garvie, 1965, 1978). Zirconia is second only to diamond in terms of hardness and is used as a specialised ceramic (Stevens, 1986). The cubic stabilised material, normally by the addition of yttrium (so-called YSZ) has a high oxygen ion conductivity at ~1000°C and is used in gas sensors (Steele et al, 1981), and as an electrolyte in solid oxide fuel cells (SOFC) (Badwal, 1990) and oxygen separators (Ziehfreund. and Maier, 1998).

III.3.a Standards

A sample of zirconium hydroxide was prepared from zirconyl chloride, as described in Section II.1.e.1, and this was heated for one hour at successive temperatures to provide a standard for nanocrystalline zirconia. Figure III.12a shows the XRPD pattern for the hydroxide. There are no real peaks, only a very broad peak at around 30° in 2θ. The result of heating for 60 minutes at 500°C is shown in Figure III.12b. There are now clear peaks that are indexed as tetragonal zirconia. The effect of calcining at higher temperatures is shown in Figures III.12c to III.12g. After calcining

at 700°C the pattern changes due to the transformation of some of the sample to the monoclinic phase. There was still a trace of tetragonal material after the 800°C anneal, but the 900°C anneal led to only the monoclinic phase being present. The particle sizes, calculated from the XRPD peaks, are listed in Table III.3. The value for the size after the 800°C anneal is hard to explain, as it is larger than after subsequent calcining at higher temperatures. Overlapping peaks would give too broad a line and hence too small a particle size. In addition, the tetragonal and monoclinic peaks are well separated. This anneal should be repeated. The preparation of zirconia by calcining the hydroxide appears to give very variable results, as shown in Table III.3, where data on particle sizes from Bearman (2000) are listed. Bearman used the same calcining procedures as those used in this work. He found that there was monoclinic material formed at a lower temperature and also that the particle size did not always increase with calcining temperature. It has been reported by Turillas et al (1995) that the transformation temperature and particle sizes are sensitive to the precipitation procedure of the hydroxide, particularly the pH and that may explain the differences in Table III.3.

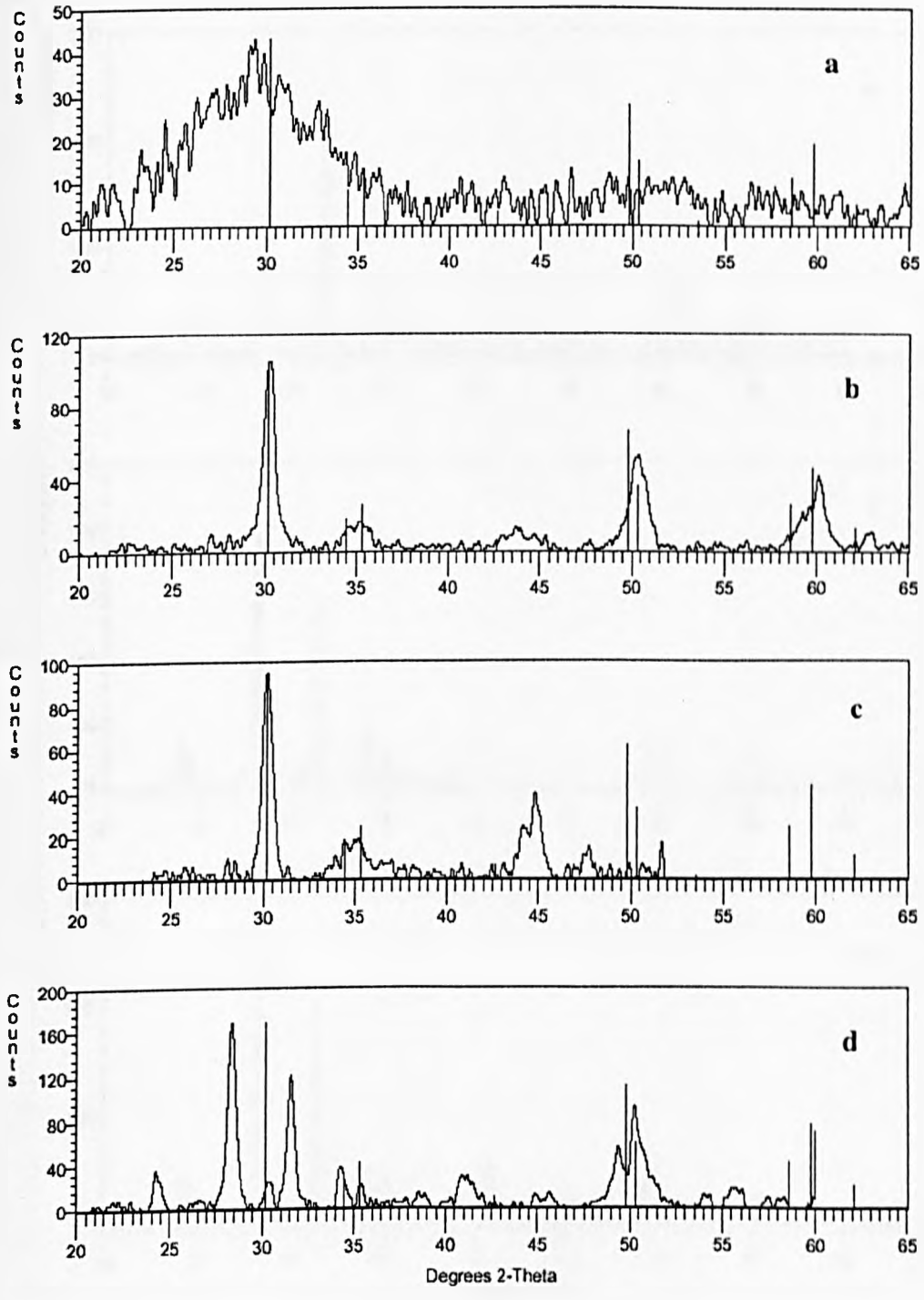

Figure III.12: The XRPD patterns for calcined zirconium hydroxide. Calcination for 60 minutes at (a) no heat, (b) 500°C, (c) 600°C and (d) 700°C. The solid lines are database positions for tetragonal zirconia.

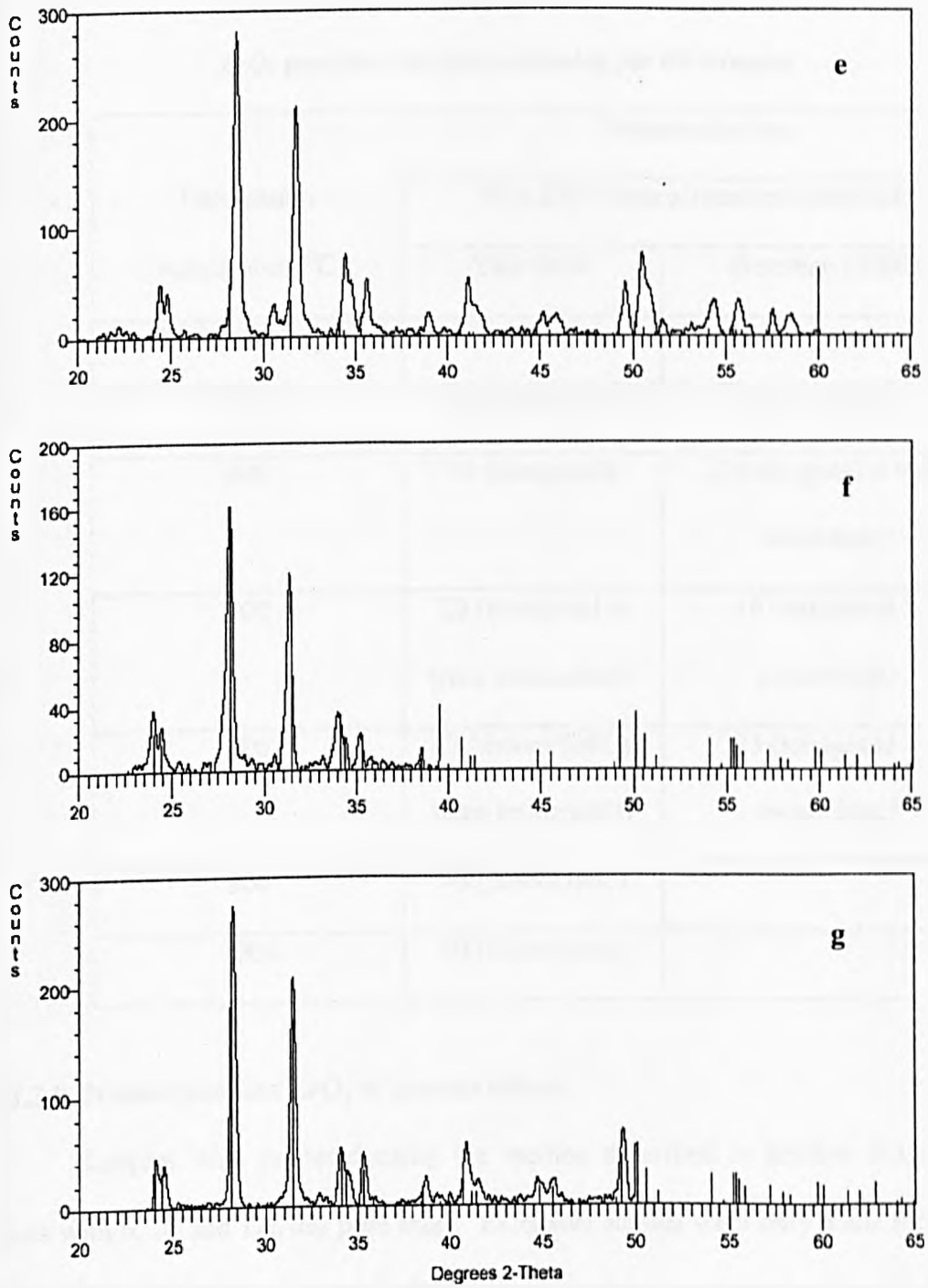

Figure III.12 (continued): The XRPD patterns for calcined zirconium hydroxide. Calcination for 60 minutes at (e) 800°C, (f) 900°C and (g) 1000°C. The solid lines are database positions for monoclinic zirconia.

Table III.3

ZrO_2 particle size after calcining for 60 minutes

Calcination temperature/°C	Particle size/nm	
	Pure ZrO_2 from zirconium hydroxide	
	This work	Bearman (2000)
25 (no heating)	1	
500	16 (tetragonal)	18 (tetragonal)
600	18 (tetragonal)	22 (tetragonal + trace monoclinic)
700	25 (tetragonal + trace monoclinic)	16 (tetragonal + monoclinic)
800	47 (monoclinic + trace tetragonal))	23 (tetragonal + monoclinic)
900	40 (monoclinic)	
1000	50 (monoclinic)	

III.3.b Nanocrystalline ZrO_2 in porous silicas

Samples were prepared using the method described in Section II.1.e.2 using silica with 6, 10 and 126 nm pore sizes. Extensive studies were only made for samples with 10nm and 126nm pores. Measurements included laboratory base XRPD and measurements of XRPD and EXAFS on station 9.3 at the Daresbury SRS. For clarity the results will be presented on the basis of the silica matrix.

III.3.b.1 *Nanocrystalline ZrO_2 in 10-nm pore silicas*

The manner of preparation was that described above and samples were prepared on the basis of the expected pore filling by the zirconium propoxide solution. Two fillings were used, half-filled and completely filled, designated HF and CF, respectively. In both cases the XRPD patterns taken in the laboratory at Kent did not reveal the presence of ZrO_2. There are two possible reasons for this result. Firstly the loss of the solvent and the resulting conversion of the propoxide to the oxide means a considerable loss in mass. Hence very little ZrO_2 is left in the pores and this may be present as a coating of the pores rather than as crystallites. In addition, the propoxide solution is very susceptible to decomposition and the sample used was not 'fresh'. Thus although ZrO_2 may be present the intensity of the laboratory X-ray source is insufficient to detect the crystallites. The experiments at the Daresbury SRS, with several orders of magnitude higher intensity were fruitful, in terms of both the XRPD and the EXAFS.

The results for the HF and CF materials at Daresbury, both XRPD and EXAFS were very similar and only those for the CF samples will be discussed here. The HF were more 'noisy' as the signals were weaker. XRPD patterns were collected at Daresbury on samples that had been heated for 60 minutes at every 100°C up to 1000°C at Kent and samples heated in situ at the SRS. The XRPD patterns are shown in Figure III.13. From the figure it can be seen that the patterns at room temperature and 500°C show no real peaks, indicating that the zirconia particles are amorphous or very small, i.e. less than 1nm.

The sizes of the zirconia particles measured form the SRS XRPD patterns are listed in Table III.4. As can be seen the sizes are very small, 5 to 6 nm, and are only present after heating at 1000°C. The fact that no signal could be observed on the

laboratory based X-ray system suggests that the concentration is very low. This point will be discussed later.

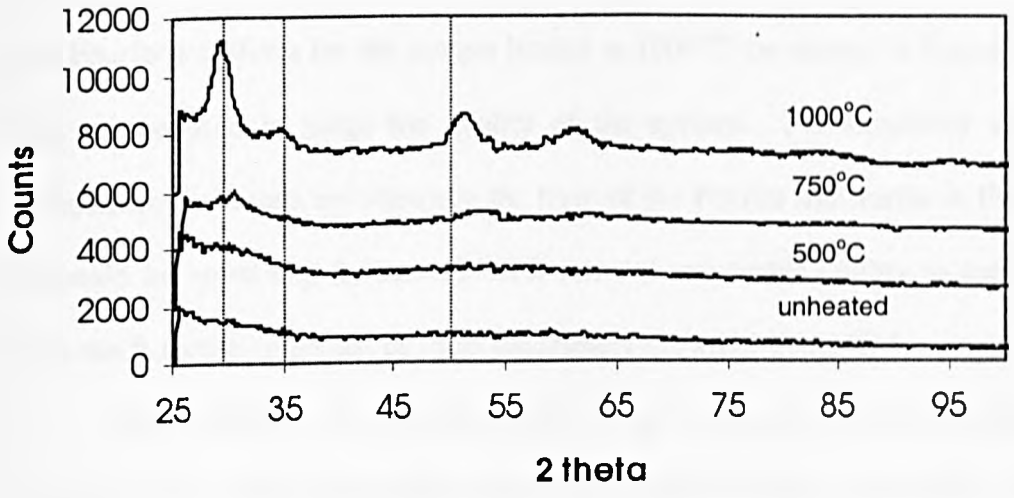

Figure III.13: The XRPD patterns for calcined zirconia in 10 nm pore silica samples. Patterns were collected on the Daresbury SRS. Calcination for 60 minutes at the temperatures indicated on the patterns. The dashed lines are database positions for tetragonal zirconia.

Table III.4

Particle sizes of ZrO_2 in 10nm-porous silica

Calcination temperature/°C	Particle size/nm	
	HF	CF
Unheated		
500		
750		
1000	5.0	5.8

The EXAFS spectra for both CF and HF samples were collected for the Zr K-edge. Again the results were very similar for both and, since the signal was less noisy, only the results for the CF sample will be discussed. The EXAFS were collected on samples that were calcined at a variety of temperatures. The full results, i.e. the EXAFS and Fourier transform for the sample heated at 1000°C are shown in Figure III.14, and this can be used to judge the quality of the spectra. For simplicity and ease of comparison the results are shown in the form of the Fourier transforms in Figure III.15. It should be noted that the raw EXAFS were of reasonable quality as can be judged from the R factors in the list of fitted parameters shown in Table III.5.

The EXAFS of the unheated sample shows two peaks in the Fourier transform at ~2.0 and 3.5 Å. These correspond to shells of O and Zr atoms, respectively. The results were very similar to those obtained by Rush (2001) for amorphous zirconium hydroxide prepared by precipitation from zirconyl chloride with aqueous ammonia. The spectrum was fitted using as a starting model the parameters of Rush (2001). The fit was good and the final parameters, as seen in Table III.5 were very similar to those of Rush and within the expected experimental error, i.e. ±0.02 Å in the radial distance. The spectrum was also fitted with tetragonal zirconia as the starting parameters. The fit is slightly better in terms of the R-factor, as might be expected as the number of variables has been increased, however the Debye–Waller for the Zr shell is unreasonably large.

Successive heating shows a gradual change in the Fourier transform. The main feature being the growth of the Zr peak at ~3.5 Å. The spectra were fitted using the tetragonal form as the starting parameters. The fits to the samples calcined at 500 and 750°C are poor in that the Debye-Waller factors for the Zr shell are unreasonably

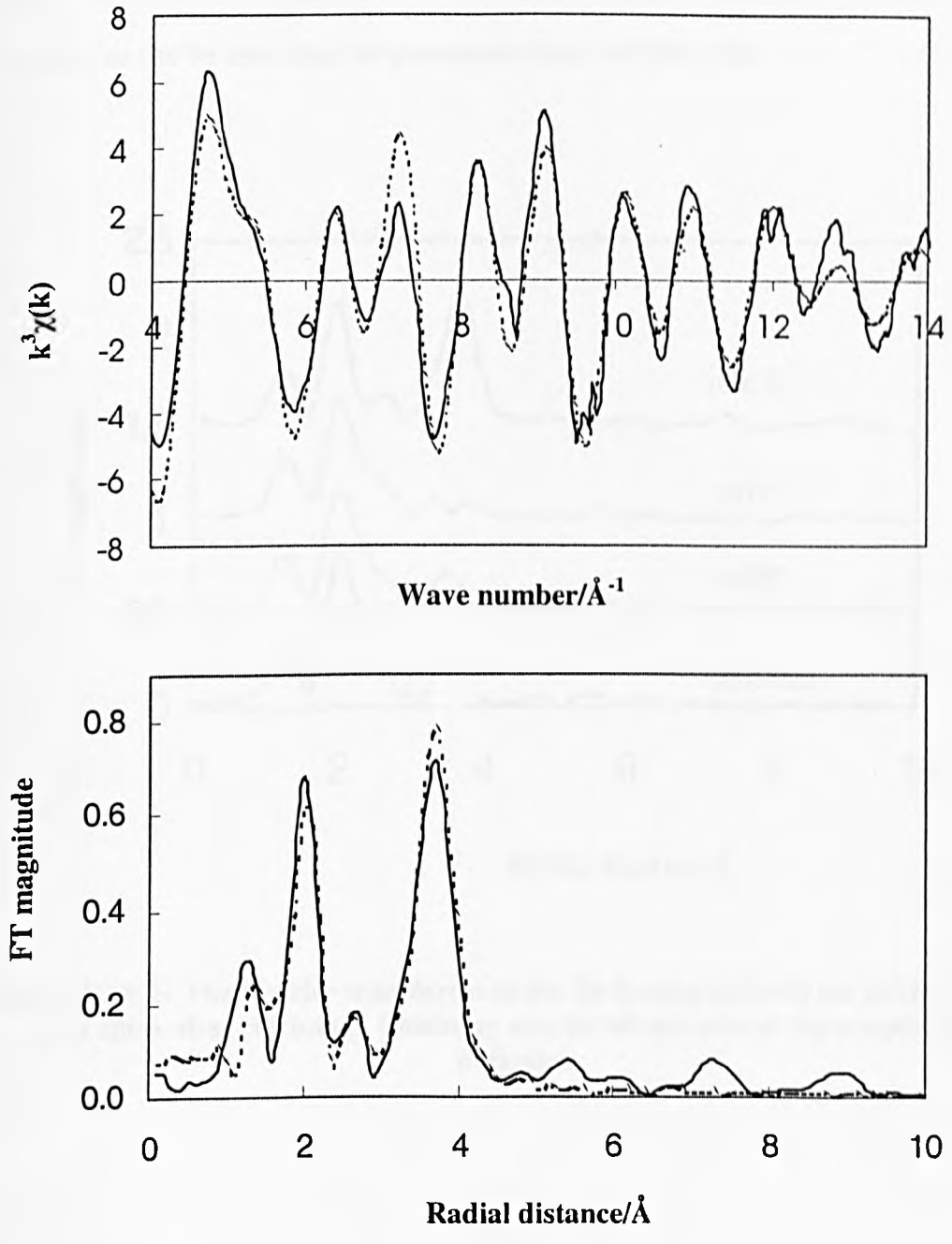

Figure III.14: The Zr K-edge EXAFS for ZrO_2 in 10 nm pore silica after calcining at 1000°C. The upper plot is the EXAFS and the lower plot the corresponding Fourier transform. The solid lines are the experimental results and the dashed lines are for the best fit model to tetragonal zirconia.(R-factor = 33%).

large. However, the sample calcined at 1000°C gives an excellent fit to tetragonal zirconia, as can be seen from the parameters listed in Table III.5.

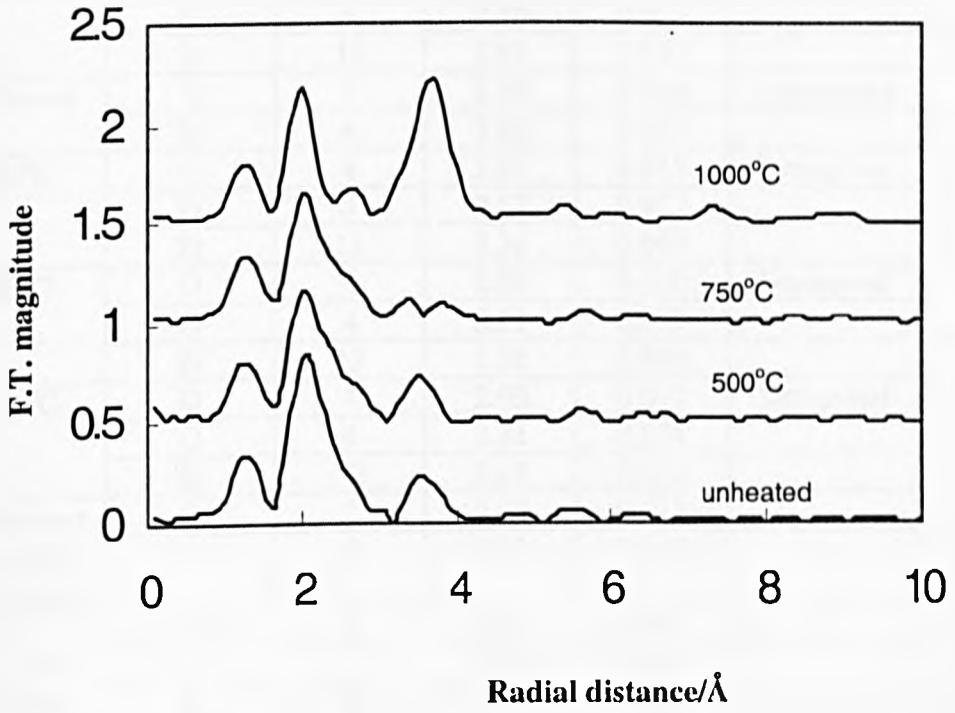

Figure III.15:- The Fourier transforms of the Zr K-edge EXAFS for ZrO_2 in 10 nm pore silica after calcining. Calcining was for 60 minutes at the temperatures indicated.

Table III.5

Best fit parameters to the EXAFS results for ZrO_2 10 nm pore silica

Sample	Atom	CN	RD/Å	$2\sigma^2/Å^2$	Model	R/%
Unheated	O	4	2.09	0.012	Tetragonal	31
	O	4	2.19	0.025		
	Zr	12	3.42	0.043		
Unheated	O	7	2.10	0.018	Amorphous	34
	Zr	4	3.40	0.027		
500°C	O	4	2.07	0.015	Tetragonal	34
	O	4	2.17	0.027		
	Zr	12	3.36	0.045		
750°C	O	4	2.07	0.016	Tetragonal	39
	O	4	2.11	0.059		
	Zr	12	3.35	0.059		
1000°C	O	4	2.09	0.012	Tetragonal	33
	O	4	2.31	0.031		
	Zr	12	3.61	0.022		
Amorphous zirconium hydroxide	O	7	2.13	0.018		From Rush (2001)
	Zr	4	3.37	0.028		
Bulk tetragonal zirconia	O	4	2.11	0.013		From Rush (2001)
	O	4	2.30	0.037		
	Zr	12	3.64	0.020		

The results from the XRPD and the EXAFS are consistent in showing that the transformation of the zirconium hydroxide to zirconia in the porous silica is not completed in this work until the samples are calcined at 1000°C. It should be noted that a calcination time of 60 minutes was employed. A transformation to zirconia might be achieved by longer heating at less than 1000°C. The present work is in agreement with previous studies of the EXAFS of the transformation from the hydroxide to zirconia. It was noted earlier that a temperature of 700°C were necessary to full conversion to zirconia (Chadwick et al, 2001). However, in the present work the particle size was maintained at 5 to 6 nm, even after heating at 1000°C. In this respect the experiments were very successful.

III.3.b.2 *Nanocrystalline ZrO_2 in 126-nm pore silica (Reatec)*

The samples were prepared in the manner described above. In this case the samples were prepared on the basis that the pores were completely filled with the propoxide.

The XRPD taken on the laboratory system of the sample prior to heating is shown in Figure III.16. For the unheated sample, Figure III.16a, there is a very broad peak between 30 and 35° which is due to the amorphous hydroxide or very small crystals of zirconia that have formed due to a decomposition of the hydroxide. The peak around 20 to 25° is due to the silica. The pattern remained the same until the sample was heated at 500°C, where the tetragonal form of zirconia was formed, as shown in Figure III.16d. The particle size was 7.5 nm. Further heating caused no change in the pattern, unlike the case of heating with no silica, except a slight increase in particle size, until 900°C. At 900°C the particle size grew to 15 nm and traces of monoclinic phase were evident, as seen in Figure III.16h. The particle sizes are listed in Table III.6.

Combined EXAFS and XRPD measurements were taken for the samples on station 9.3 at the Daresbury SRS. The XRPD patterns were consistent with those collected on the laboratory system and need not be discussed. EXAFS spectra were collected on an unheated sample and samples heated for 60 minutes at 500, 750 and 1000°C. The full results, i.e. the EXAFS and Fourier transform for the sample heated at 1000°C are shown in Figure III.17, and this can be used to judge the quality of the spectra. The Fourier transforms of the spectra are shown in Figure III.18. Again, this is done for simplicity and the raw EXAFS were of good quality. It should be noted that the raw EXAFS were of reasonable quality as can be judged from the R factors in the list of fitted parameters shown in Table III.7.

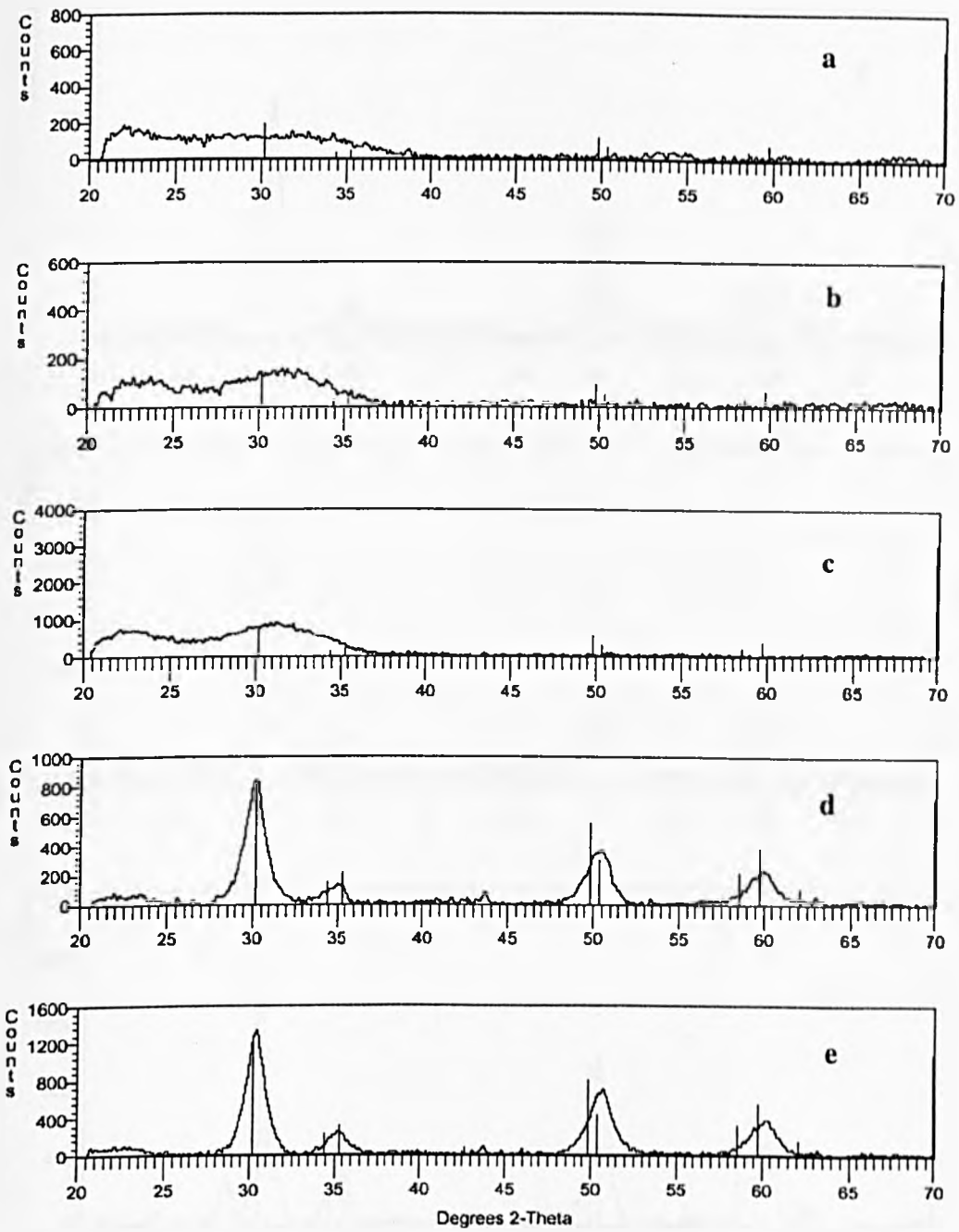

Figure III.16: The XRPD patterns for calcined zirconia in 126 nm pore silica samples. Calcination for 60 minutes at (a) no heat, (b) 300°C, (c) 400°C, (d) 500°C and (e) 600°C. The solid lines are database positions for tetragonal zirconia.

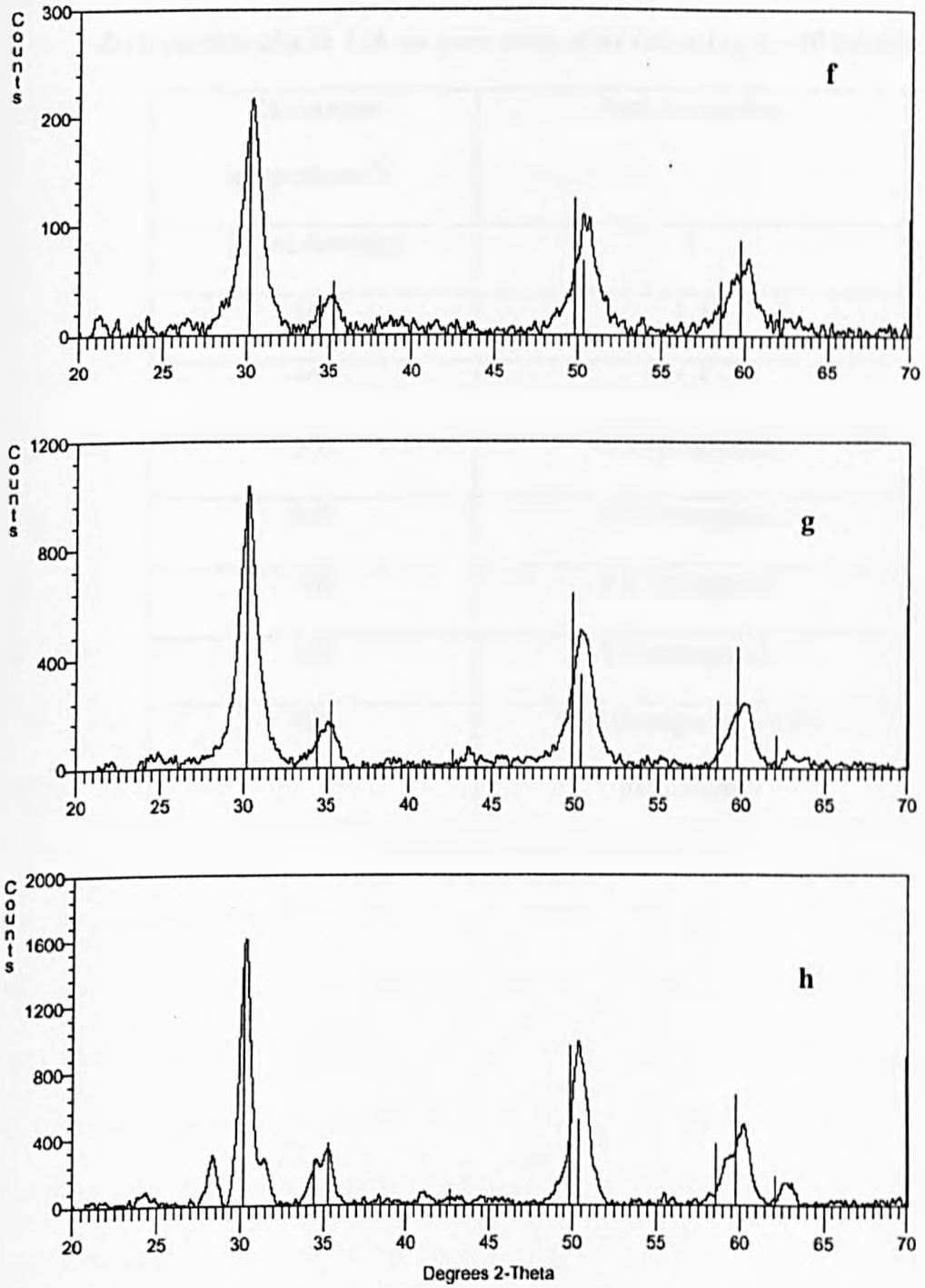

Figure III.16 (continued): The XRPD patterns for calcined zirconia in 126 nm pore silica samples. Calcination for 60 minutes at (f) 700°C, (g) 800°C, and (h) 900°C. The solid lines are database positions for tetragonal zirconia.

Table III.6

ZrO_2 particle size in 126 nm pore silica after calcining for 60 minutes

Calcination temperature/°C	Particle size/nm
25 (no heating)	1
300	1.5
400	1.5
500	7.5 (tetragonal)
600	8.0 (tetragonal)
700	8.0 (tetragonal)
800	8.0 (tetragonal)
900	15.0 (tetragonal + trace monoclinic)

The Fourier transform of the unheated sample is typical of the amorphous zirconium hydroxide reported by other workers (Rush et al, 2000, Rush 2001). The fit to an amorphous model was in excellent agreement with the previous work, as can be seen in Table III.7. The sample that had been heated at 500°C was fitted to an amorphous model and a tetragonal model. The fit to the amorphous model is still good. An equally good fit, in terms of the R-factor, was found to the tetragonal starting model. However, the parameters are unreasonable; the Zr-Zr distance is too short and the Debye-Waller factors are too large for the two outer shells. This observation is consistent with other studies (Chadwick et al, 2001, Rush 2001) where the XRPD suggests that calcining the hydroxide at 500°C produces tetragonal zirconia and the EXAFS indicates that the sample still contains amorphous material. The XRPD is only sensitive to crystalline material and the EXAFS to the average local structure. Other work has suggested calcining at 700°C is required to give complete transformation to zirconia (Chadwick et al, 2001). The EXAFS for the sample heated at 750°C gives a good fit to the tetragonal structure and the particle size has been kept small at 8 nm. The sample heated at 1000°C did show evidence of the formation of some monoclinic material in the sample. A rough estimate from the peak heights gives about 20% monoclinic material. Hence the EXAFS was fitted to both the tetragonal and monoclinic structures. The best fit is clearly to the tetragonal structure and the parameters obtained for the monoclinic structure are clearly unreasonable. This reflects the insensitivity of EXAFS when studying a mixture of structures.

These studies show that incorporating zirconia inside the larger pore silica does maintain the small particle size up to 900°C. In contrast to the small pore silica a larger zirconia content can be achieved.

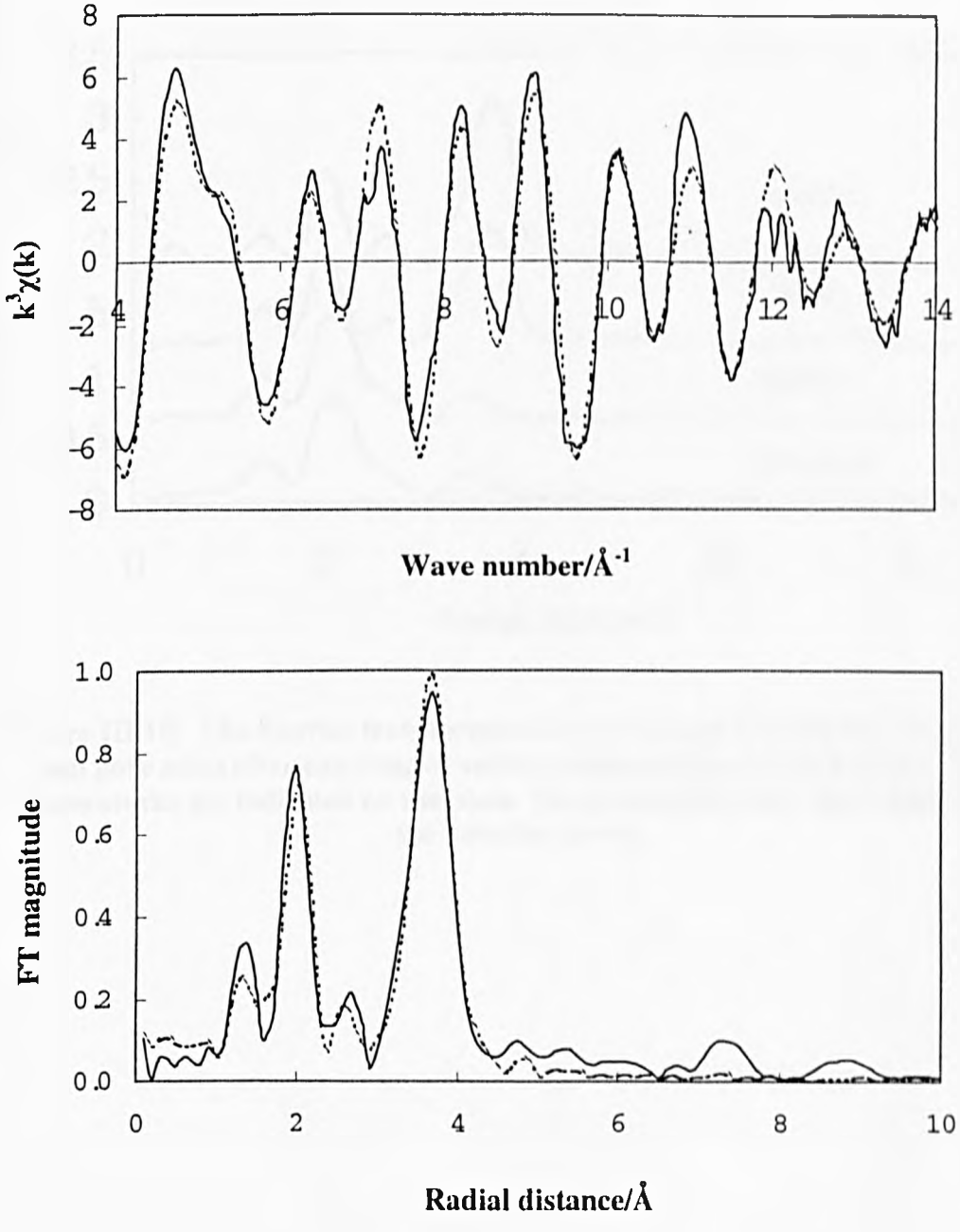

Figure III.17:- The Zr K-edge EXAFS for ZrO_2 in 126 nm pore silica after calcining at 750°C. The upper plot is the EXAFS and the lower plot the corresponding Fourier transform. The solid lines are the experimental results and the dashed lines are for the best fit model to tetragonal zirconia. (R-factor = 26%)

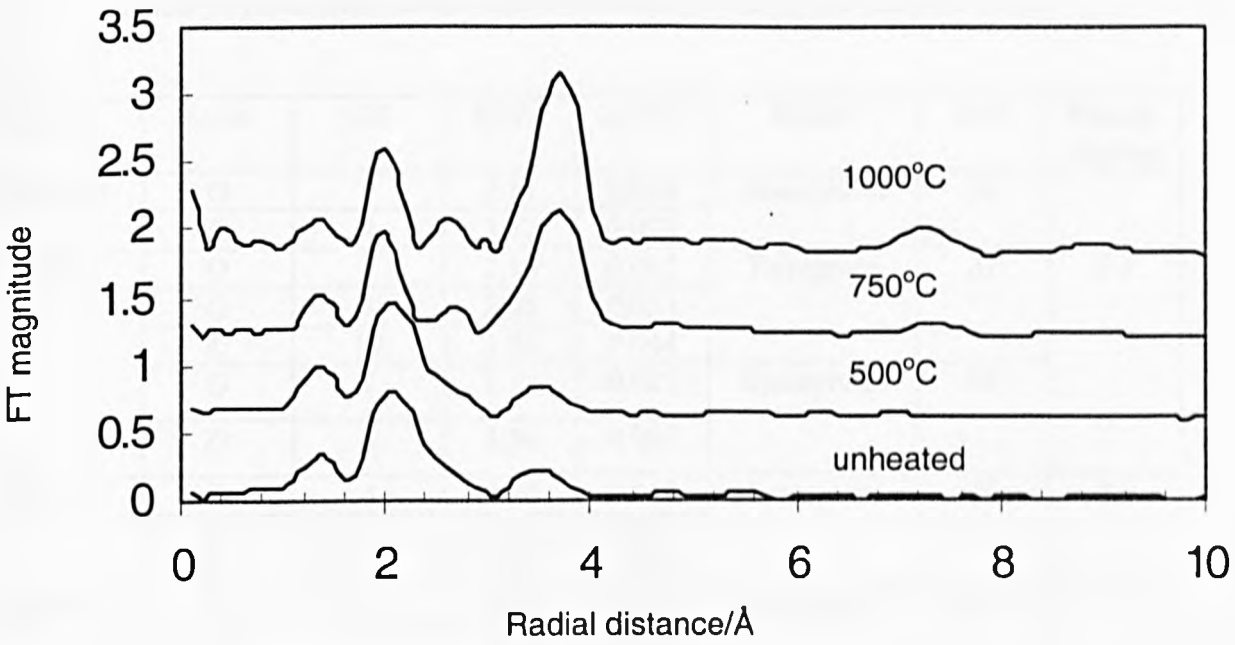

Figure III.18: The Fourier transforms of the Zr K-edge EXAFS for ZrO_2 in 126 nm pore silica after calcining at various temperatures for 60 minutes. The temperatures are indicated on the plots. Successive plots have been displaced by 0.6 units for clarity.

Table III.7

Best fit parameters to the EXAFS results for ZrO_2 126 nm pore silica

Sample	Atom	CN	RD/Å	$2\sigma^2/Å^2$	Model	R/%	Particle size/nm
Unheated	O	7	2.11	0.024	Amorphous	32	-
	Zr	4	3.37	0.028			
500°C	O	4	2.10	0.012	Tetragonal	32	7.5
	O	4	2.08	0.053			
	Zr	12	3.36	0.044			
	O	7	2.10	0.023	Amorphous	33	
	Zr	4	3.36	0.027			
750°C	O	4	2.08	0.010	Tetragonal	26	8.0
	O	4	2.30	0.032			
	Zr	12	3.61	0.019			
1000°C	O	4	2.09	0.008	Tetragonal	26	~15
	O	4	2.33	0.024			
	Zr	12	3.64	0.015			
	O	7	1.99	0.022	Monoclinic	46	
	Zr	7	3.83	2.558			
	Zr	4	3.83	0.003			
	Zr	1	4.21	0.001			
Amorphous zirconium hydroxide	O	7	2.13	0.018		From Rush (2001)	
	Zr	4	3.37	0.028			
Bulk tetragonal zirconia	O	4	2.11	0.013		From Rush (2001)	
	O	4	2.30	0.037			
	Zr	12	3.64	0.020			
Bulk monoclinic zirconia	O	7	2.15	0.020		From Rush (2001)	
	Zr	7	3.46	0.015			
	Zr	4	4.03	0.017			
	Zr	1	4.55	0.002			

III.3.c Nanocrystalline ZrO_2 with alumina

Samples containing 5, 10 and 15% alumina were prepared using the procedures described in Section II.1e.3. Most of the work was focused on the 15% alumina sample and the results for this will be discussed first.

The XRPD for the as-prepared sample of the 15% alumina material, i.e. after hydrolysis of the alkoxide mixture, is shown in Figure III.19a. There are two very broad peaks and they were not fitted to the database. The sample was then calcined for 60 minutes at 100°C intervals. Up to calcination temperatures of 600°C there was no change in the XRPD pattern. After the 700°C anneal peaks began to appear, as shown in Figure III.19f. However, these peaks are not obvious peaks for either zirconia or alumina. After the 800°C anneal the pattern was 'clean', as shown in Figure III.19g, and all the peaks, except a very small peak at $2\theta = 43.5^{\circ}$, matched tetragonal zirconia. The particle size was 11 nm. The pattern remained unchanged after anneals at 900 and 1000°C and the particle sizes were 11 and 13 nm, respectively. The calcination at 1200°C produced the pattern for monoclinic zirconia and the particle size was 38 nm. The patterns are summarised in Figure III.19a to j.

It is worth noting that DSC measurements were made of the as-prepared sample. Heating to 600°C revealed no endothermic or exotherms. Unfortunately, higher temperatures could not be achieved as the only available pans were made of aluminium, melting point 650°C. However, this confirmed the temperature of transition to zirconia was in excess of 600°C.

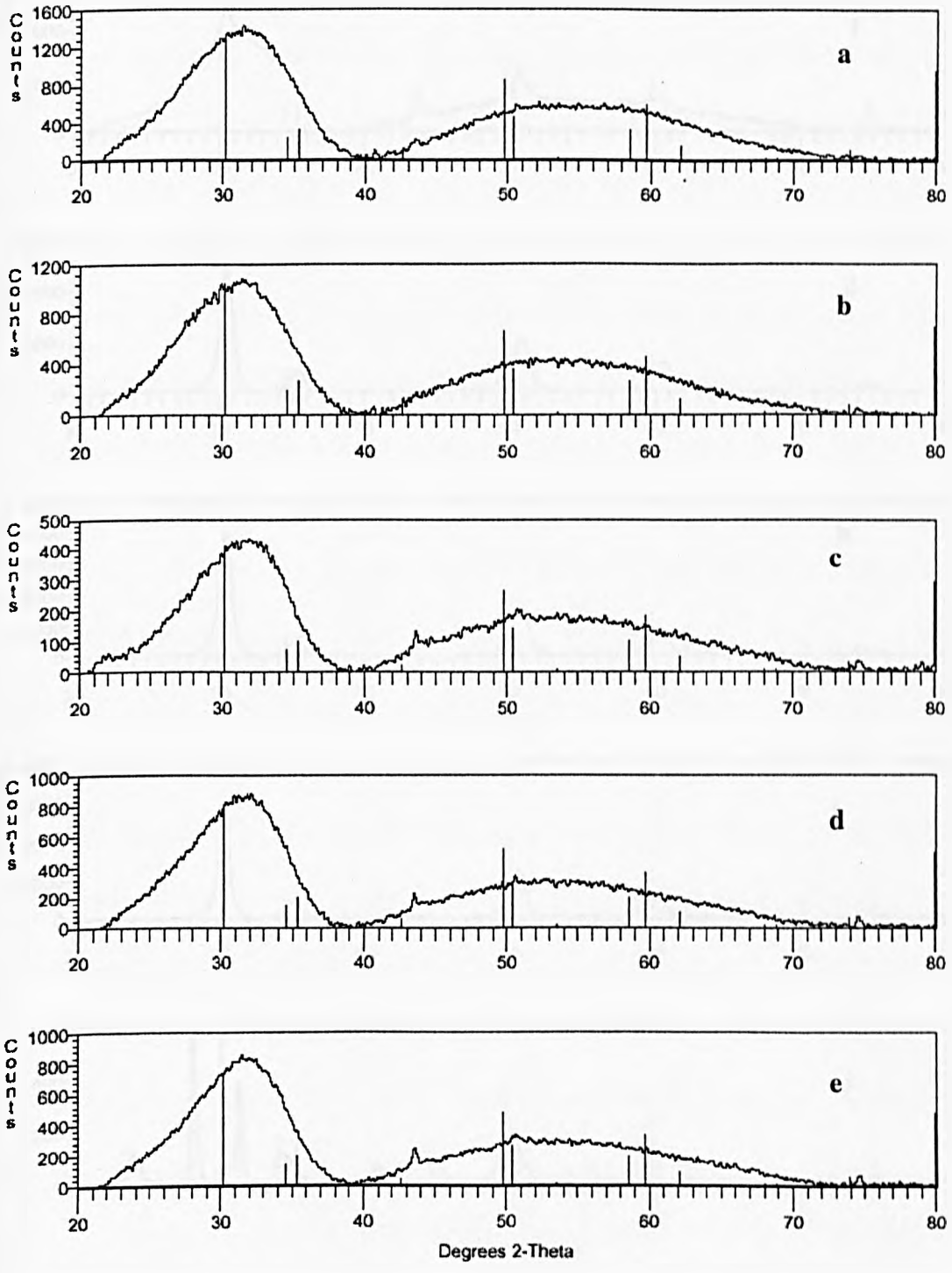

Figure III.19: The XRPD patterns for calcined zirconia – 15% alumina samples. Calcination for 60 minutes at (a) no heat, (b) 140°C, (c) 400°C, (d) 500°C and (e) 600°C. The solid lines are database positions for tetragonal zirconia.

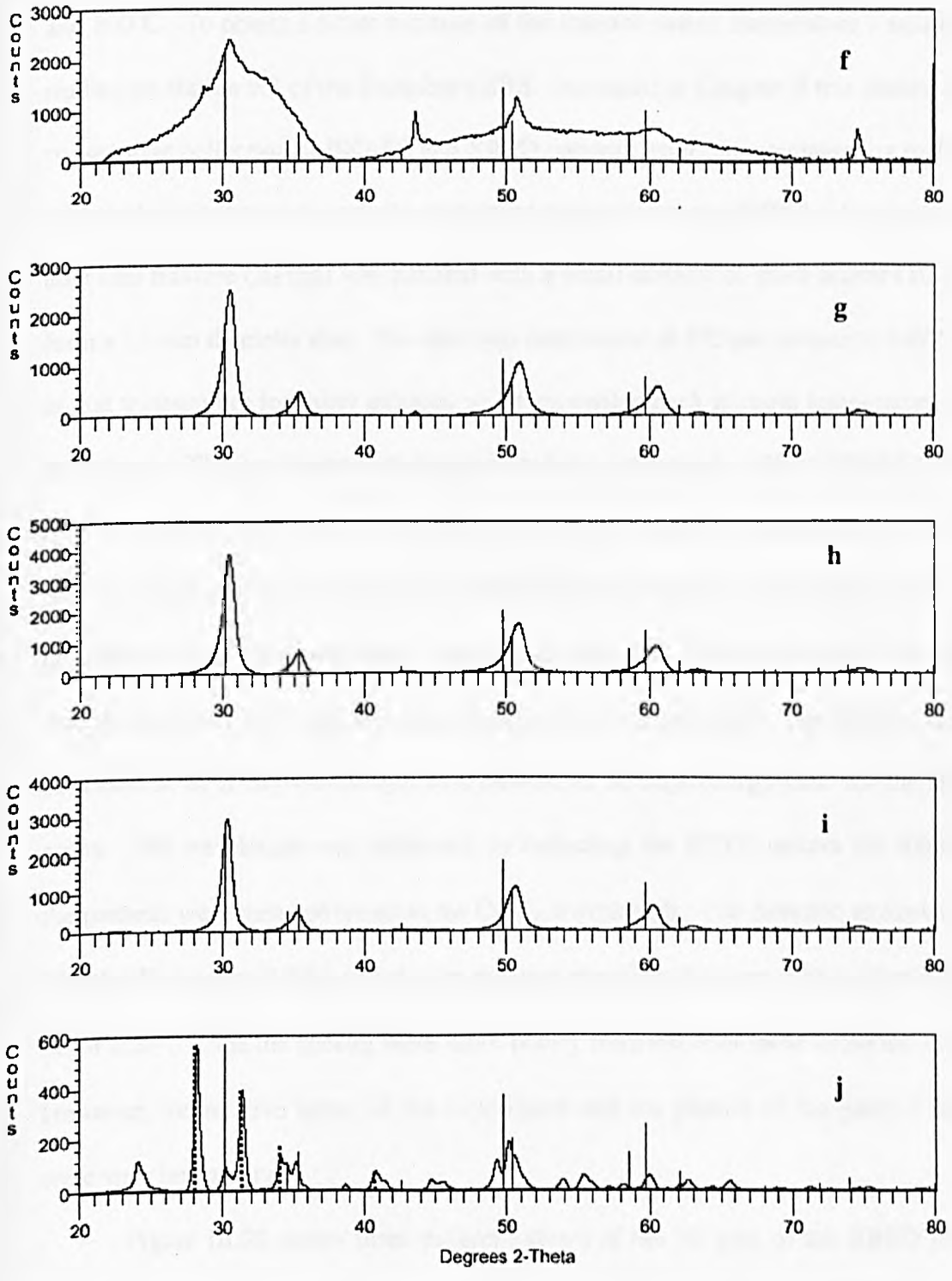

Figure III.19 (continued): The XRPD patterns for calcined zirconia – 15% alumina samples. Calcination for 60 minutes at (f) 700°C, (g) 800°C, (h) 900°C, (i) 1000°C and (j) 1200°C. The solid lines and dashed lines are database positions for tetragonal zirconia and monoclinic zirconia, respectively.

The transformation of the sample to zirconia occurs somewhere between 700 and 800°C. To obtain a better estimate of the transformation temperature a sample was studied on station 9.3 of the Daresbury SRS. As stated in Chapter II this station allows consecutive collection of EXAFS and XRPD patterns from room temperature to 1100°C (although in the present work the maximum temperature was 940°C). A sample of the unheated mixture (20 mg) was pelleted with a small amount of silica binder (10 mg) to form a 13 mm diameter disc. The disc was then heated at 5°C per minute to 940°C, held at that temperature for thirty minutes, and then cooled back to room temperature at 5°C per minute. The instrument was programmed to continuously collect EXAFS followed by XRPD patterns. The EXAF scan took 2 minutes and 20 seconds, the XRPD scan took 2 minutes and there was a 40 s dead time between the two scans. Thus every 25°C an XRPD pattern was produced. During the collection of the pattern the temperature was changing by 10°C and the mean temperature was recorded. The XRPD scan was collected at an X-ray wavelength of 0.6889Å, Zr K edge energy used for the EXAFS scans. The wavelength was calibrated by collecting the XRPD pattern for silicon and the patterns were then converted to the Cu K_α wavelength. The detector, as explained in Chapter II, was an INEL curved wire position sensitive detector, which gave a step in 2θ of 0.21°. Thus the spectra were more poorly resolved than those collected at UKC. However, the relative speed of the experiment and the picture of the general features were very informative.

Figure III.20 shows three different views of the 3D plot of the XRPD patterns collected at Daresbury. The transformation is occurring between 700 and 800°C. Figure III.21 shows the individual patterns collected in this temperature range. The pattern is broad until 741°C, where small peaks start to form. These grow rapidly until 791°C and then only grow slowly up to 841°C. The two clear peaks, at 2θ ~30 and

~35°, are those for tetragonal zirconia. Given that the heating is continuous, the transformation temperature is estimated as 770-780°C. The 3D plot for the cooling runs is shown in Figure III.22 and the patterns remain unchanged. Figure III.23 shows the patterns for the original, unheated sample at room temperature, the sample at 940°C and at room temperature after heating and cooling. These show that the sample remains unchanged after cooling and is still tetragonal zirconia. The particle sizes estimated from these patterns were consistent with those measured on the laboratory system.

The samples prepared with 5 and 10% alumina were not studied in detail. They were calcined for 60 minutes at 700°C and the XRPD patterns collected. These are shown in Figure III.24. For these samples the XRPD only exhibits the patterns for tetragonal zirconia with small particle sizes; 10 and 12 nm for the 10 and 5% alumina samples, respectively.

The particle sizes for the samples are summarised in Table III.8. . It is clear that the addition of alumina is restricting particle growth at high temperatures. The most striking result is that the sample with 15% alumina has a particle size of only 12 nm after annealing at 1000°C and that there is only tetragonal zirconia present. Also included in Table III.8 are the data of Viswanath and Ramaswamy (1999). Unfortunately, these workers did not record the time they held their samples at a given calcining temperature, however there is a reasonable agreement up to a temperature of 900°C.

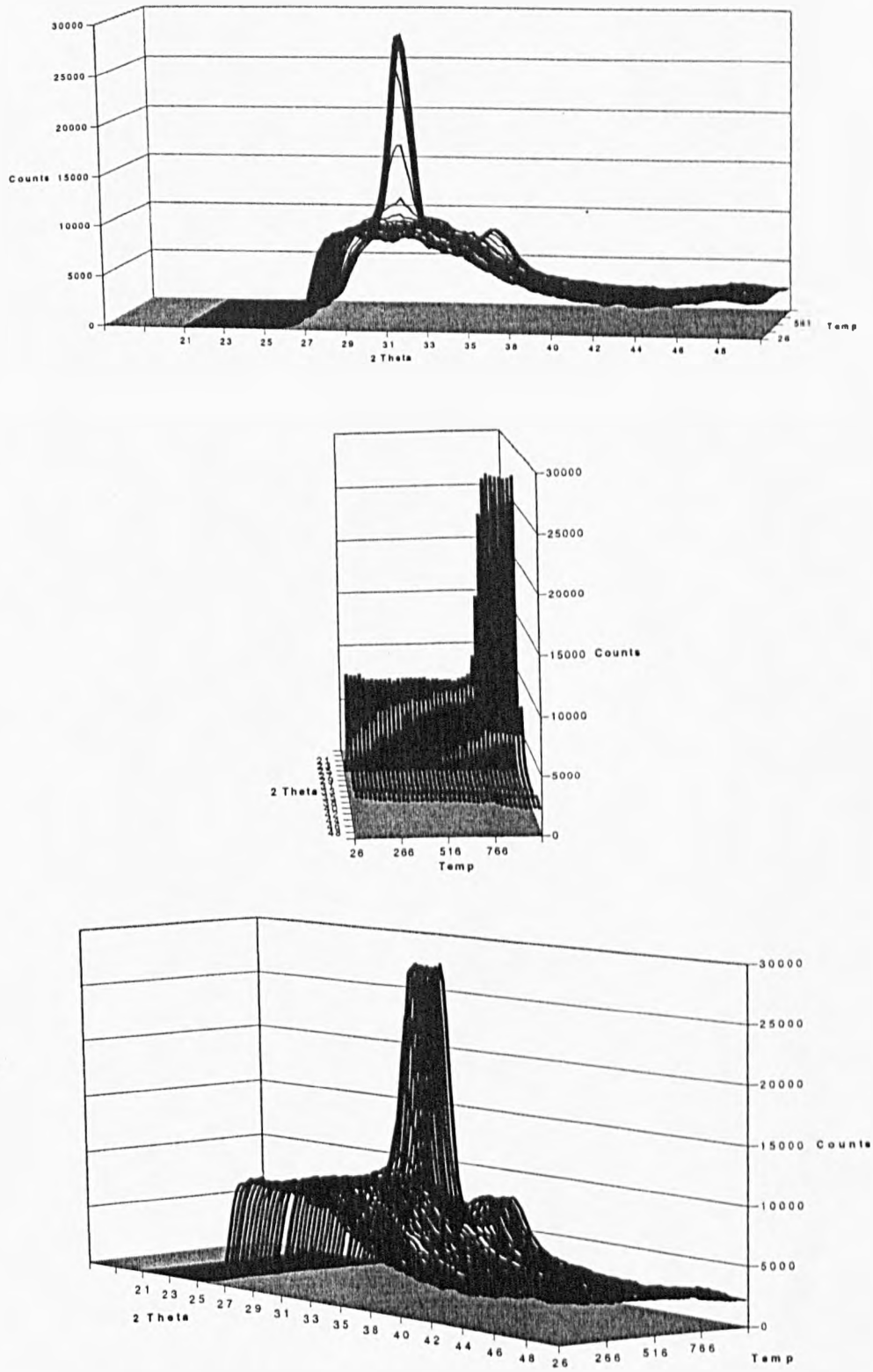

Figure III.20: The XRPD patterns collected on heating of the zirconia-15% alumina samples. The patterns were collected at the Daresbury SRS. The 3D plots are three views of the patterns on heating the as-prepared sample from room temperature to 940°C at 5° per minute.

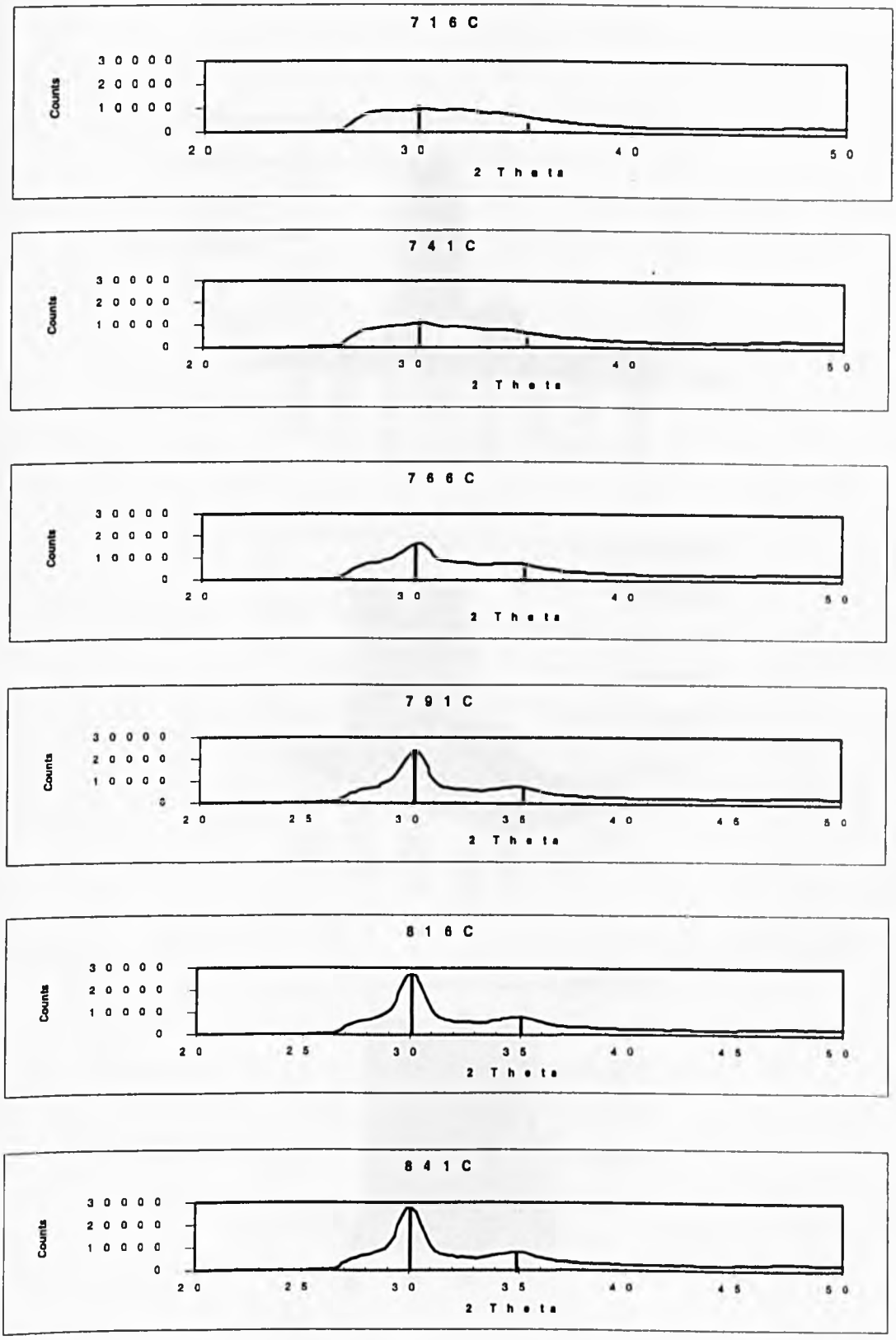

Figure III.21: Selected patterns from Figure 20. The temperatures are indicated on the plots. The solid lines are database positions for tetragonal zirconia.

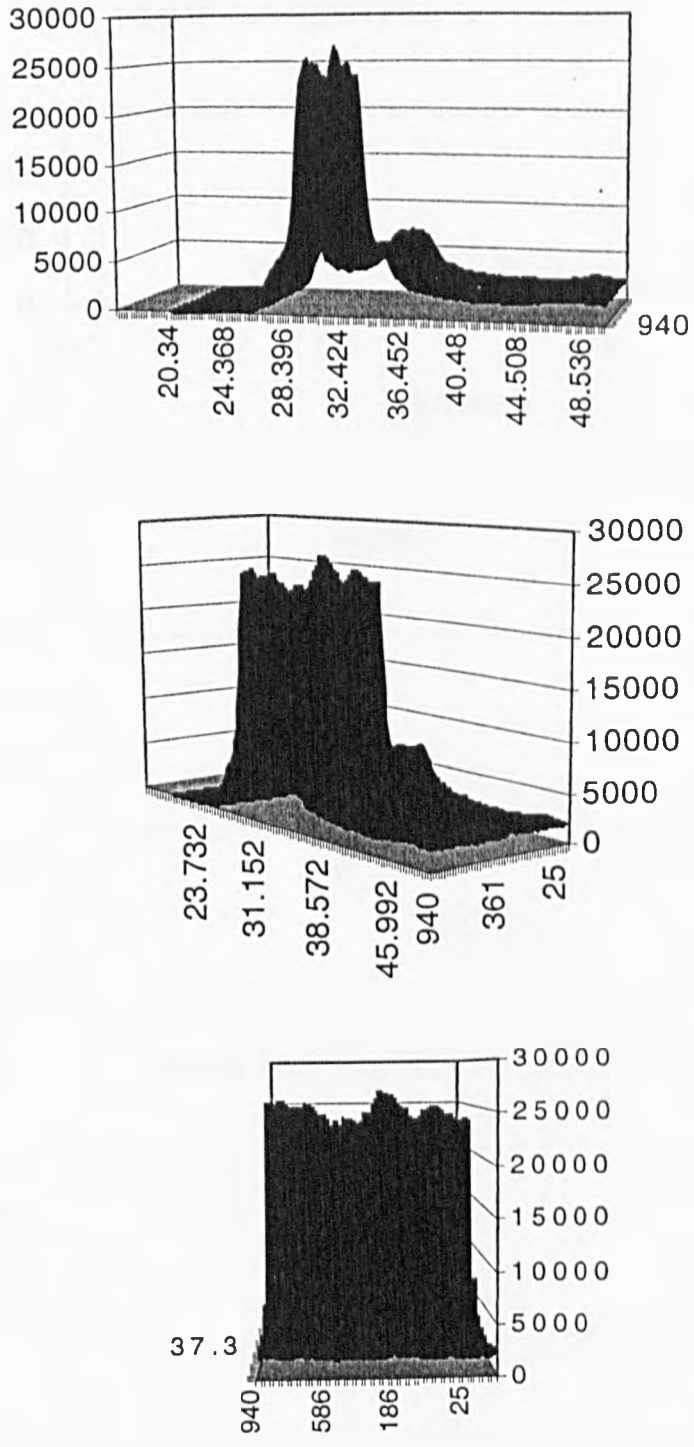

Figure III.22: The XRPD patterns collected on cooling of the zirconia-15% alumina samples. The patterns were collected at the Daresbury SRS. The 3D plots are three views of the patterns on cooling the sample from 940°C at 5° per minute.

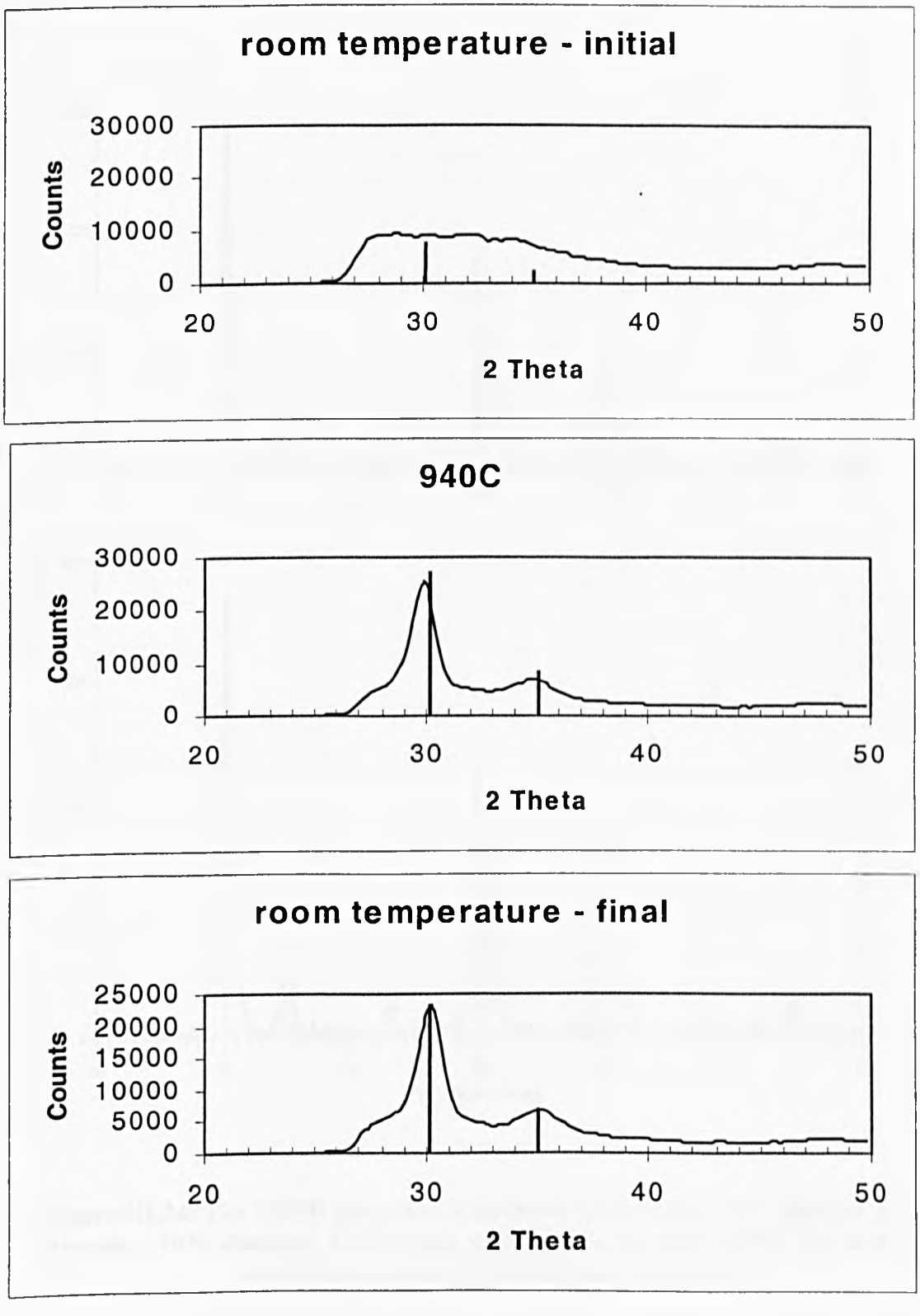

Figure III.23: Selected XRPD patterns collected for the zirconia-15% alumina samples. They show the results for the unheated sample, the sample at the maximum temperature of 940°C and the final cooled sample.

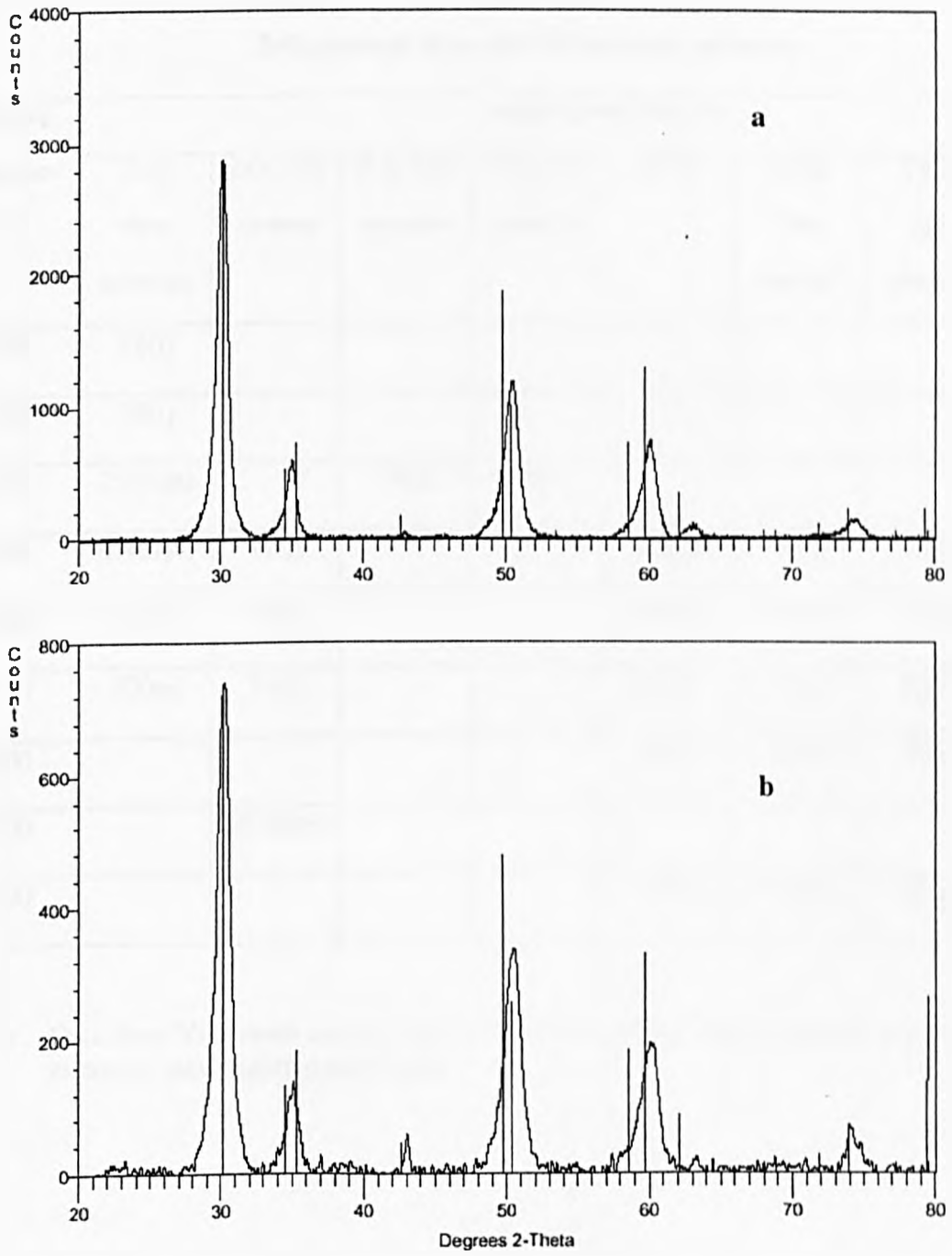

Figure III.24: The XRPD patterns for calcined (a) zirconia – 5% alumina and (b) zirconia – 10% alumina. Calcination was for 60 minutes at 700°C. The solid lines are database positions for tetragonal zirconia.

Table III.8

ZrO_2 particle sizes after 60 minutes calcining

Calcining temperature/ °C	Sample particle size/nm							
	ZrO_2 from hydroxide	ZrO_2 15% alumina	ZrO_2 10% alumina	ZrO_2 5% alumina	YSTZ*	YSTZ 15% alumina*	YSTZ 10% alumina*	YSTZ 5% alumina*
500	16(t)							
600	18(t)							
700	25(t+m)		10(t)	12(t)				
800	47(m+t)	11(t)			10(t)	9(t)	10(t)	9(t)
900	40(m)	10(t)			11(t)	10(t)	11(t)	11(t)
1000	50(m)	12(t)			27(t)	33(t)	32(t)	28(t)
1100					47(t)	50(t)	50(t)	44(t)
1200		35 (t+m)						
1300					58(t)	56(t)	57(t)	55(t)

- Data from Viswanath and Ramaswamy (1999); tetragonally stabilised yttrium doped zirconia, heating times undefined.

EXAFS spectra were collected for the sample containing 15% alumina. The full results, i.e. the EXAFS and Fourier transform for the sample heated at 900°C are shown in Figure III.25, and this can be used to judge the quality of the spectra. The Fourier transforms for the unheated sample and samples that were calcined at 700, 900 and 1200°C are shown in Figure III.26 and the fits to the data are listed in Table III.9. The spectrum for the unheated sample was very similar to that for amorphous zirconium hydroxide obtained by other workers (Rush et al, 2000, Rush, 2001) and for the zirconia in silica unheated samples. As can be seen in Table III.9 a good fit was obtained assuming zirconium hydroxide as the starting model and the parameters were in good agreement with previous studies. The sample calcined at 700°C for 60 minutes was still predominantly amorphous from the XRPD pattern. However some peaks were beginning to appear, as seen in Figure III.19. Therefore both amorphous and tetragonal zirconia models were used as the starting parameters for the fitting. As can be seen the fit to both models is poor, with R-factors above 40%, and the Zr-Zr distance is between that for the two models. The EXAFS suggests that there has been some transformation to tetragonal zirconia in this sample. The sample calcined for 60 minutes at 900°C gives an excellent fit to tetragonal zirconia, as expected from the XRPD patterns for this sample. The XRPD pattern for the sample calcined for 60 minutes at 1200°C showed predominantly the presence of monoclinic zirconia. This was confirmed by the EXAFS, which gave a good fit to a starting model of the monoclinic structure.

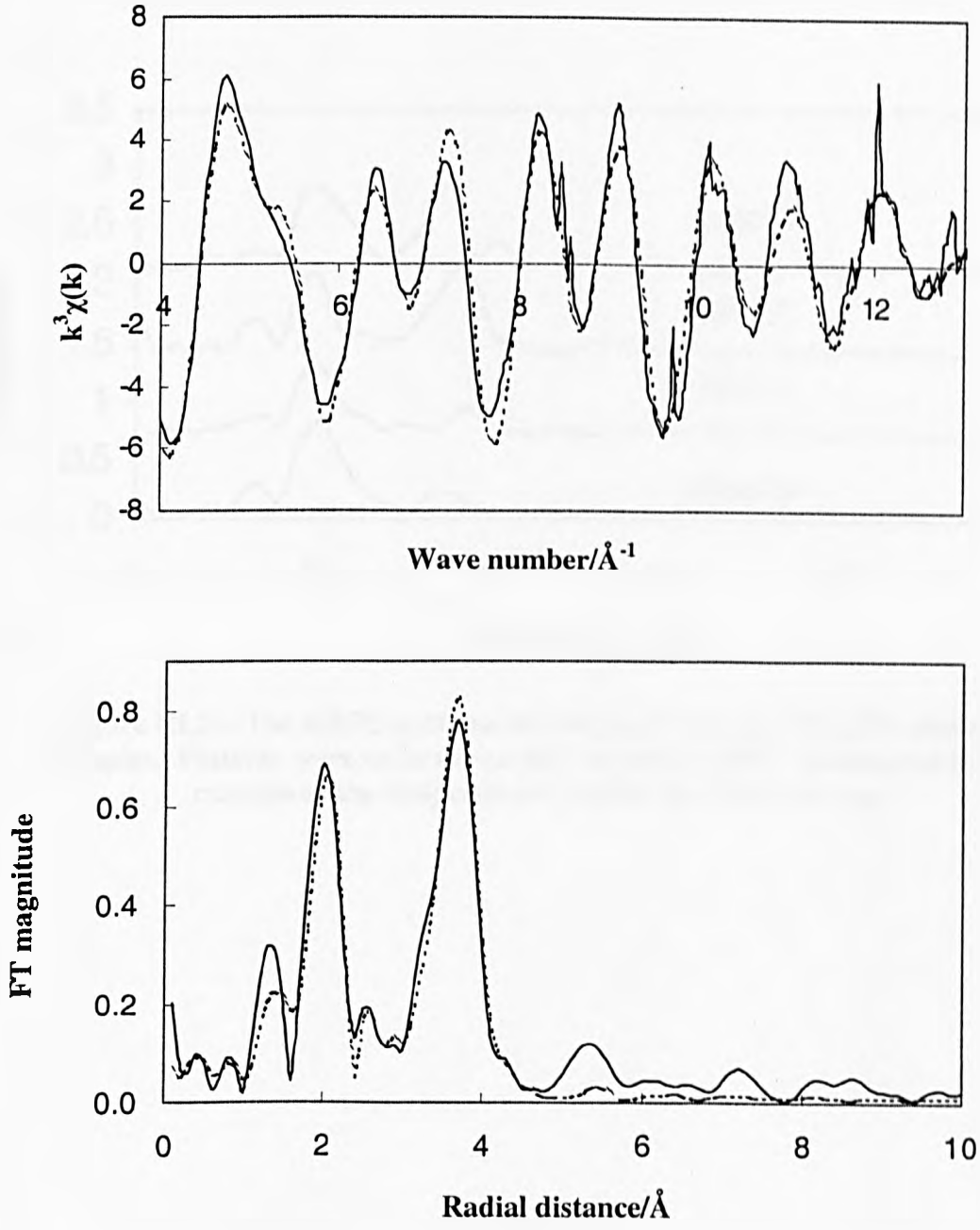

Figure III.25: The Zr K-edge EXAFS for ZrO_2 with 15% alumina after calcining at 900°C. The upper plot is the EXAFS and the lower plot is the corresponding Fourier transform. The solid lines are the experimental results and the dashed lines are for the best fit model to tetragonal zirconia. (R-factor = 28%)

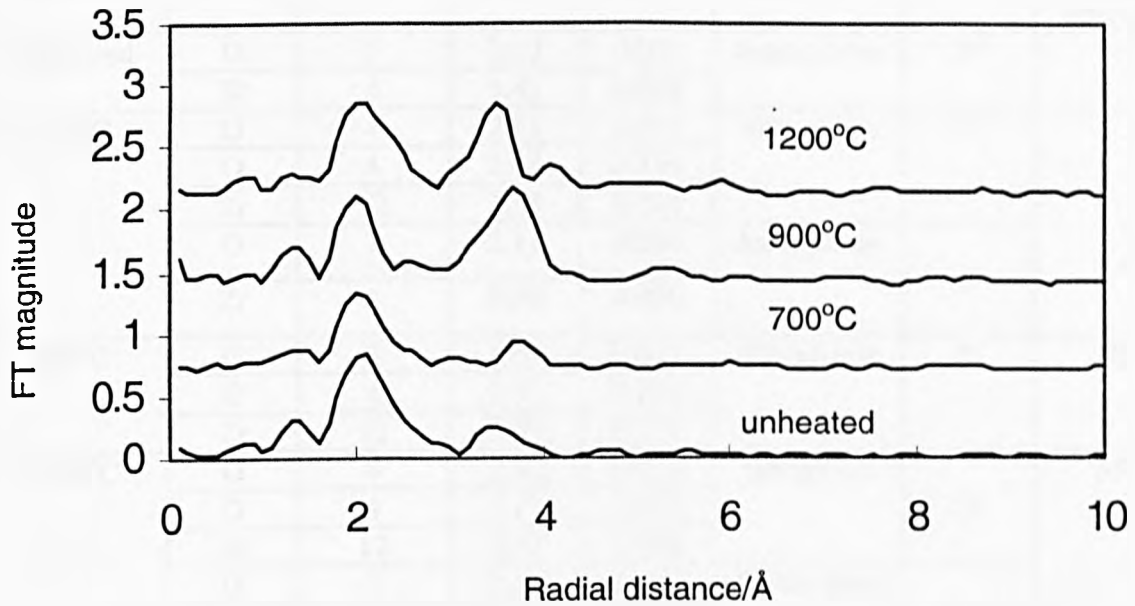

Figure III.26: The XRPD patterns for calcined zirconia with 15% alumina samples. Patterns were collected on the Daresbury SRS. Calcination for 60 minutes at the temperatures indicated on the patterns

Table III.9

Best fit parameters to the EXAFS results for zirconia – 15% alumina.

Sample	Atom	CN	RD/Å	$2\sigma^2/Å^2$	Model	R/%	Particle size/nm
Unheated	O	7	2.12	0.023	Amorphous	34	-
	Zr	4	3.41	0.026			
700°C	O	4	2.11	0.015	Tetragonal	41	-
	O	4	2.44	0.354			
	Zr	12	3.55	0.044			
	O	7	2.11	0.034	Amorphous	46	
	Zr	4	3.55	0.026			
900°C	O	4	2.09	0.011	Tetragonal	28	10
	O	4	2.31	0.038			
	Zr	12	3.59	0.021			
1200°C	O	4	2.10	0.014	Tetragonal	38	35
	O	4	2.17	0.039			
	Zr	12	3.42	0.024			
	O	7	2.12	0.022	Monoclinic	33	
	Zr	7	3.44	0.016			
	Zr	4	3.96	0.021			
	Zr	1	4.51	0.009			
Amorphous zirconium hydroxide	O	7	2.13	0.018		From Rush (2001)	
	Zr	4	3.37	0.028			
Bulk tetragonal zirconia	O	4	2.11	0.013		From Rush (2001)	
	O	4	2.30	0.037			
	Zr	12	3.64	0.020			
Bulk monoclinic zirconia	O	7	2.15	0.020		From Rush (2001)	
	Zr	7	3.46	0.015			
	Zr	4	4.03	0.017			
	Zr	1	4.55	0.002			

The addition of alumina clearly restricts the growth of zirconia and a number of interesting questions arise. An obvious question is the nature of the pre-cursor and the transformation to zirconia. The transformation of the pure hydroxide occurs at 500°C. The addition of alumina increases the transformation temperature in a manner proportional to the amount of alumina; the 5 and 10% had transformed at 700°C, but the 15% sample transformed at 770-780°C. This suggests the precursor is complex and not a simple mixture of zirconium and aluminium hydroxides. Attempts were made to precisely define the transformation temperatures with DSC measurements but they were not successful, as the upper temperature limit of the equipment was 600°C. Another intriguing feature of the results is the lack of any peaks for alumina in all the XRPD patterns.

III.3.d Summary of the results for nanocrystalline ZrO_2

The attempts to confine nanocrystalline zirconia were successful. The two methods, confining inside silica pores and adding alumina, restricted the growth of the zirconia. The results are summarised in Figure III.27. Confinement in the small pore silica, 10 nm pores, produced very small particles, however there was very little zirconia in the samples. The use of the larger pored Reatec silica, 126 nm pores, gave a sample with a significant amount of zirconia although the zirconia particles did begin to grow at 900°C and there was some formation of monoclinic zirconia. The addition of alumina was the most successful in terms of restricting growth, which began only above 1000°C.

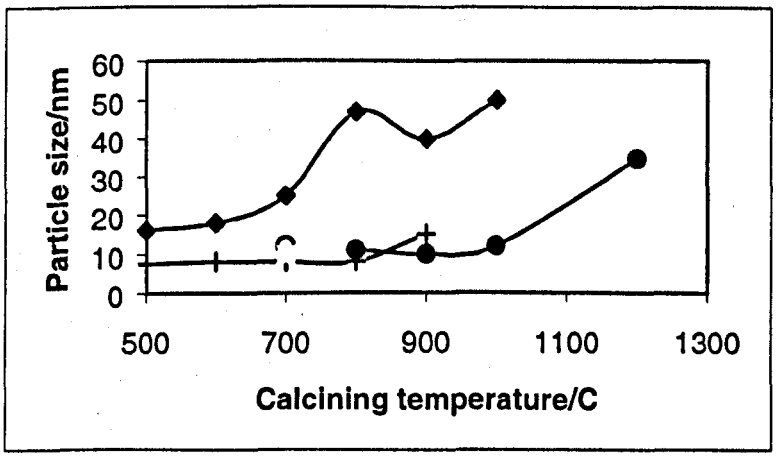

Figure III.27: A summary of the zirconia particle sizes for different preparation methods. ◆ pure zirconia by heating the hydroxide; + zirconia in 126 nm pore silica; ● zirconia – 15% alumina.

III.4 NANOCRYSTALLINE CERIA

Cerium oxide, ceria, (CeO_2) has the cubic fluorite-structure (space group Fm3-m) when pure or doped with lower valent cations. The pure material is a mixed electronic and oxygen ion conductor. The doped material (e.g. 8 mol per cent Gd) is a purely ionic conductor and can be a better oxygen ion conductor than YSZ at equivalent temperatures (e.g. Gd-doped CeO_2) and offers the potential for an SOFC operating at lower temperatures (Kharton et al, 2001).

III.4.a Standards

The samples of cerium hydroxide were prepared using the method described in Section II.1.f.1. Calcining was performed for 360 minutes at 150, 400, 600 and 800°C. The usual calcining time of 60 minutes was not used for these samples as the procedure of Nachimuthu et al (2000) was followed. The XRPD patterns of these samples are shown in Figure III. 28. The pattern for the aged precipitate shows only peaks for ceria peaks that might be expected from $Ce(OH)_3$ are absent. The particle sizes estimated from the XRPD patterns are listed in Table III.10.

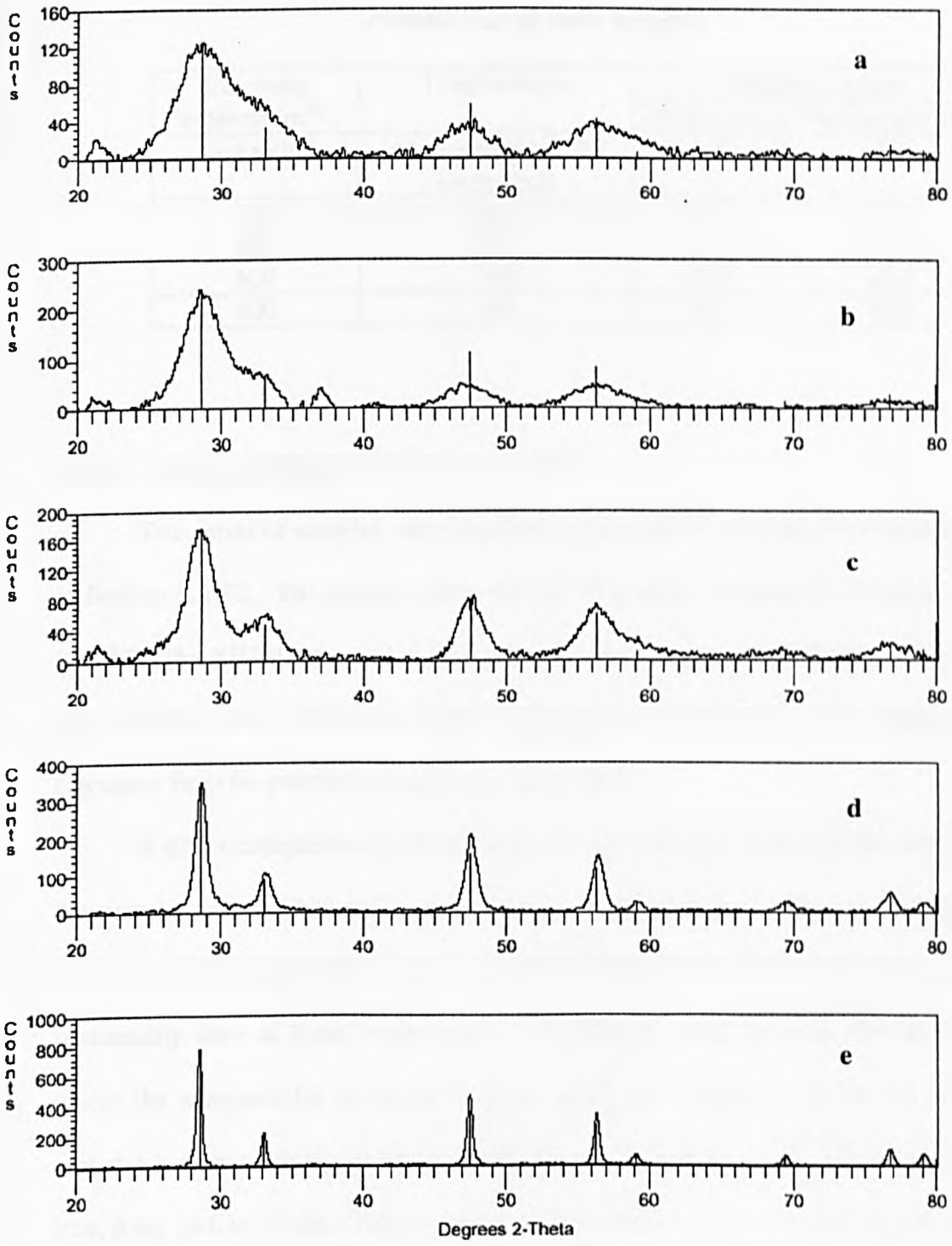

Figure III.28: The XRPD patterns for calcined cerium hydroxide samples. Calcination for 360 minutes at (a) no heat (aged for seven days), (b) 150°C, (c) 400°C, (d) 600°C and (e) 800°C. The solid lines are database positions for cubic ceria.

Table III.10

Particle sizes of ceria samples.

Calcining temperature/°C	Time/minutes	Particle size/nm	
		This work	Nachimuthu et al
No heating	Aged precipitate for seven days	2.2	2.1
150	360	2.8	2.3
400	360	4.8	4.6
600	360	12.2	15.4
800	360	48	75.6

III.4.b Nanocrystalline CeO_2 in porous silicas

Two series of samples were prepared using 4 and 10 nm pore silica, as described in Section II.1.f.2. The samples were calcined at a series of temperatures from 500 to 1000°C. The XRPD patterns for the 4 nm pore material are shown in Figure III.29 and the patterns for the 10 nm pore material are shown in Figure III.30. The particle sizes calculated from the patterns are shown in Tables III.11.

A direct comparison of the particle sizes for the pure ceria and the ceria inside the pores is not possible due to the different annealing times. However, the particle sizes on calcining up to 600°C are very similar for all the materials and the growth is presumably slow at these temperatures. Differences occur between 700 and 800°C where the nanoparticles in the silica pores grow less rapidly. For the 10 nm pore material a long calcining overnight (720 minutes) produced only a small increase in size, from 19.6 to 24 nm. This is good evidence that the silica is restricting the growth of the ceria nanoparticles.

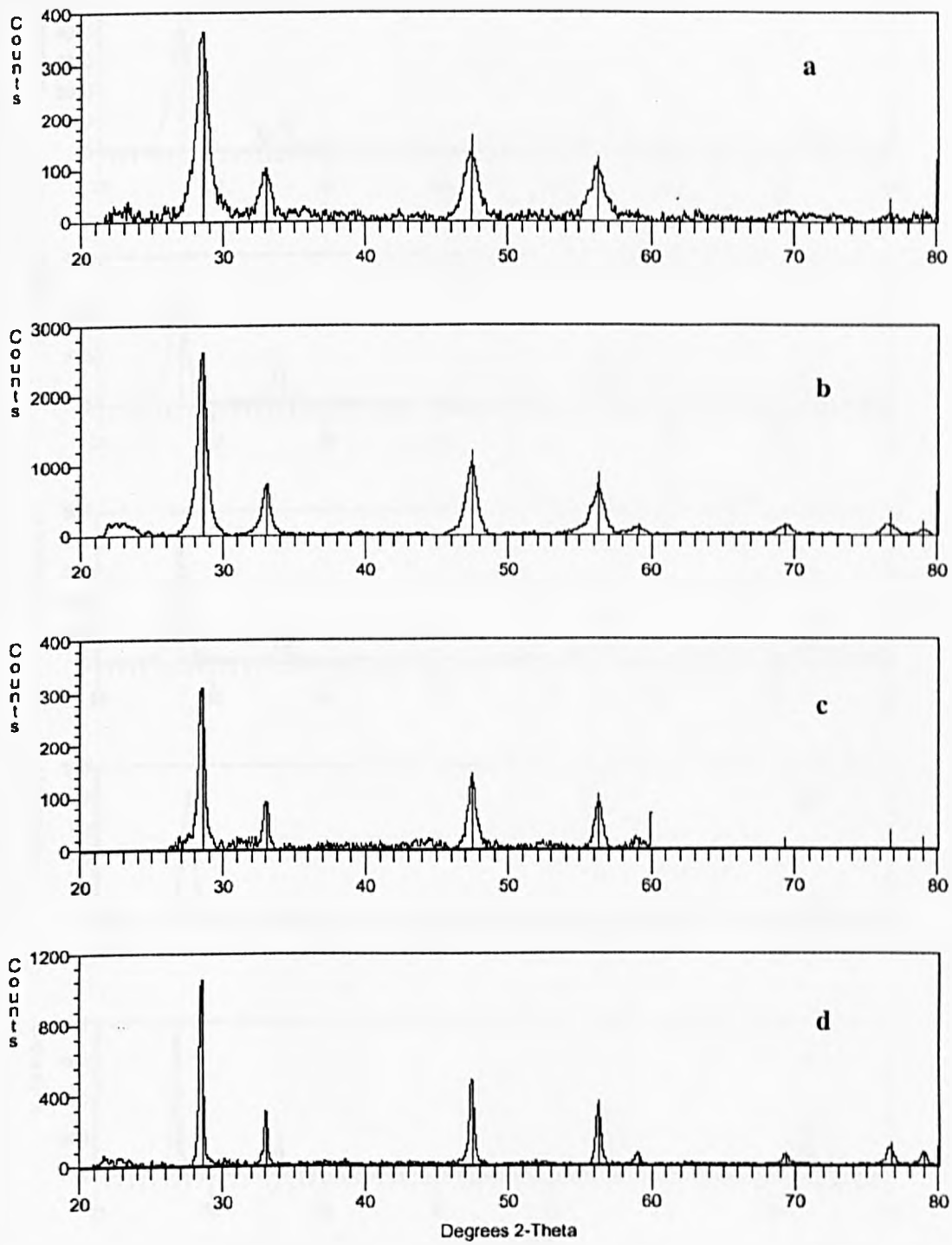

Figure III.29: The XRPD patterns for calcined cerium hydroxide in 4 nm pore silica samples. Calcination for 60 minutes at (a) 500°C (b) 600°C, (c) 800°C, and (d) 1000°C. The solid lines are database positions for cubic ceria.

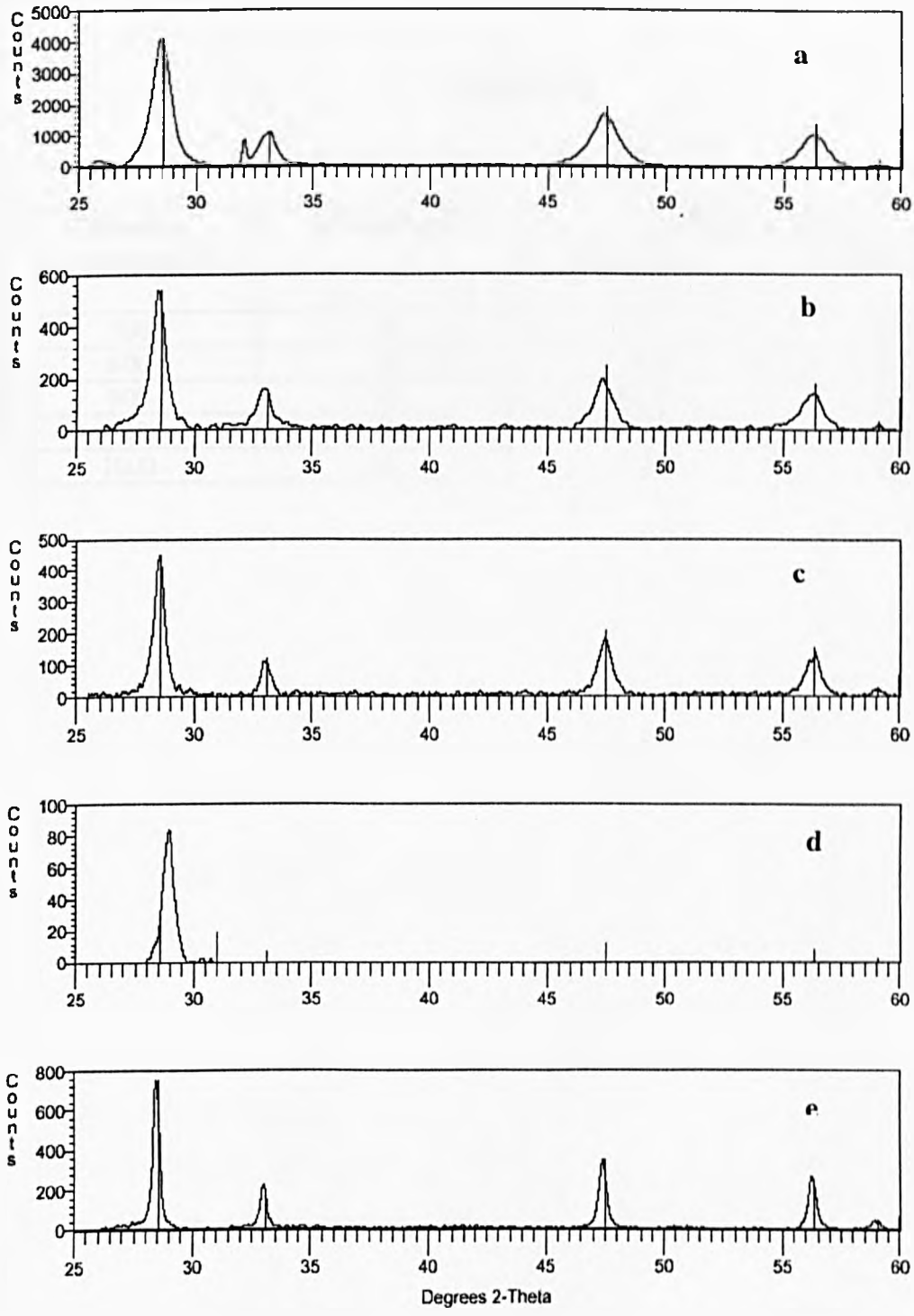

Figure III.30: The XRPD patterns for calcined cerium hydroxide in 10 nm pore silica samples. Calcination for 60 minutes at (a) 500°C (b) 600°C, (c) 800°C, (d) 800°C (calcined for 720 minutes) and (e) 1000°C. The solid lines are database positions for cubic ceria.

Table III.11

Ceria in 4 nm and 10 nm pore silica

Calcining temperature/^{0}C	Time/minutes	Particle size/nm	
		4 nm silica	10 nm silica
500	60	8.7	8.3
600	60	12.3	12.5
800	60	18.5	19.6
800	720	-	24
1000	60	79.3	64

III.4.c Summary of the results for nanocrystalline CeO_2

Although the study of nanocrystalline was not extensive the evidence is that the inclusion of the nanoparticles in the silica pores did restrict the growth. A plot of the particle size versus calcining temperature is shown in Figure III.31. The differences in calcining time have been ignored to make this plot. At 800°C the ceria in the silica pores is smaller, and as remarked earlier for one sample a very long calcining time was used. At 1000°C the growth is clearly rapid and the restriction of growth by the silica pores is not evident.

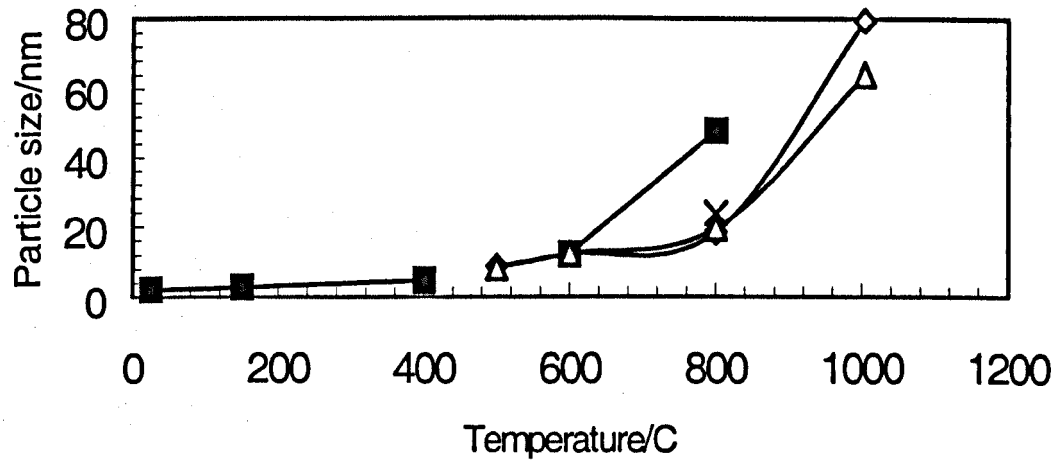

Figure III.31: A summary of the ceria particle sizes for different preparation methods. ■ pure ceria by heating the hydroxide; △ ceria in 10 nm pore silica; X ceria in 10 nm pore silica calcined for 720 minutes; ✧ ceria in 4 nm pore silica.

III.5 NANOCRYSTALLINE TIN OXIDE

Tin oxide occurs naturally as cassiterite and has the rutile structure (space group P42/mnm). It is an *n*-type semiconductor, which is used in flammable gas sensors (Sberveglieri, 1992,1995). Strategies that have been employed to improve the sensitivity and selectivity have included the use of nanocrystalline materials and doping with aliovalent cations.

III.5.a Standards

The preparation of pure nanocrystalline tin oxide was described in Section II.1.g.1. The particle size, as estimated from the XRPD peaks was 2.1 nm. The sample was then calcined for 60 minutes at several temperatures up to 1000°C. After each calcination a XRPD pattern was collected and some of the results are shown in Figure III.32. The sizes of the particles after each calcination are shown in Table III.12. As noted by other workers growth of the nanocrystals is evident even at temperatures as low as 400°C (Davis et al, 1996).

Table III.12

Pure nanocrystalline tin oxide particle sizes.

Calcining temperature/°C	Calcining time/minutes	Particle size/nm
25		2.1
400	60	3.6
500	60	7.1
600	60	13.6
700	60	25.1
800	60	32.0
900	60	44.4
1000	60	87.8

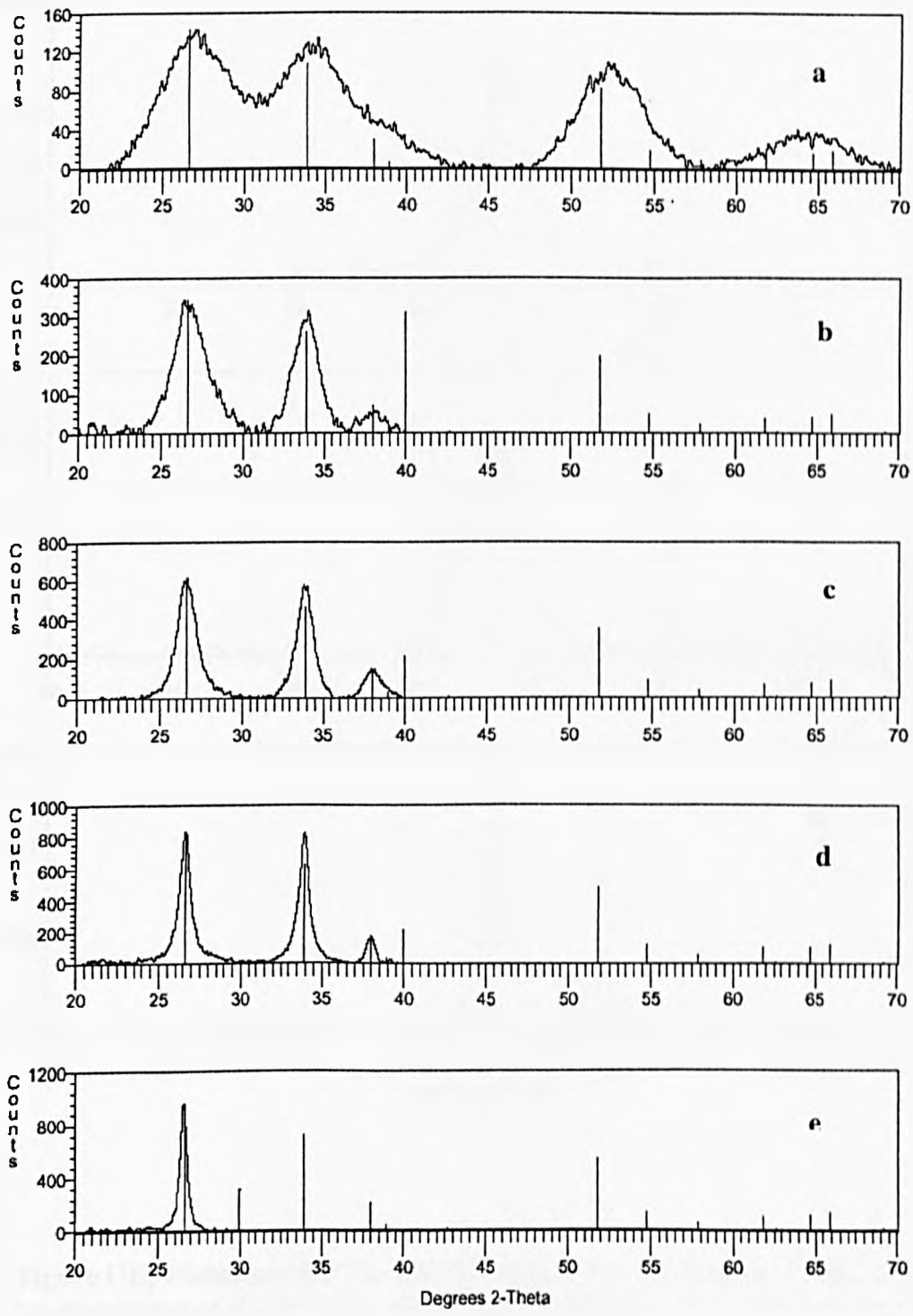

Figure III.32: The XRPD patterns for calcined tin oxide. Calcination for 60 minutes at (a) no heat (b) 400°C, (c) 500°C, (d) 600°C and (e) 700°C. The solid lines are database positions for cassiterite.

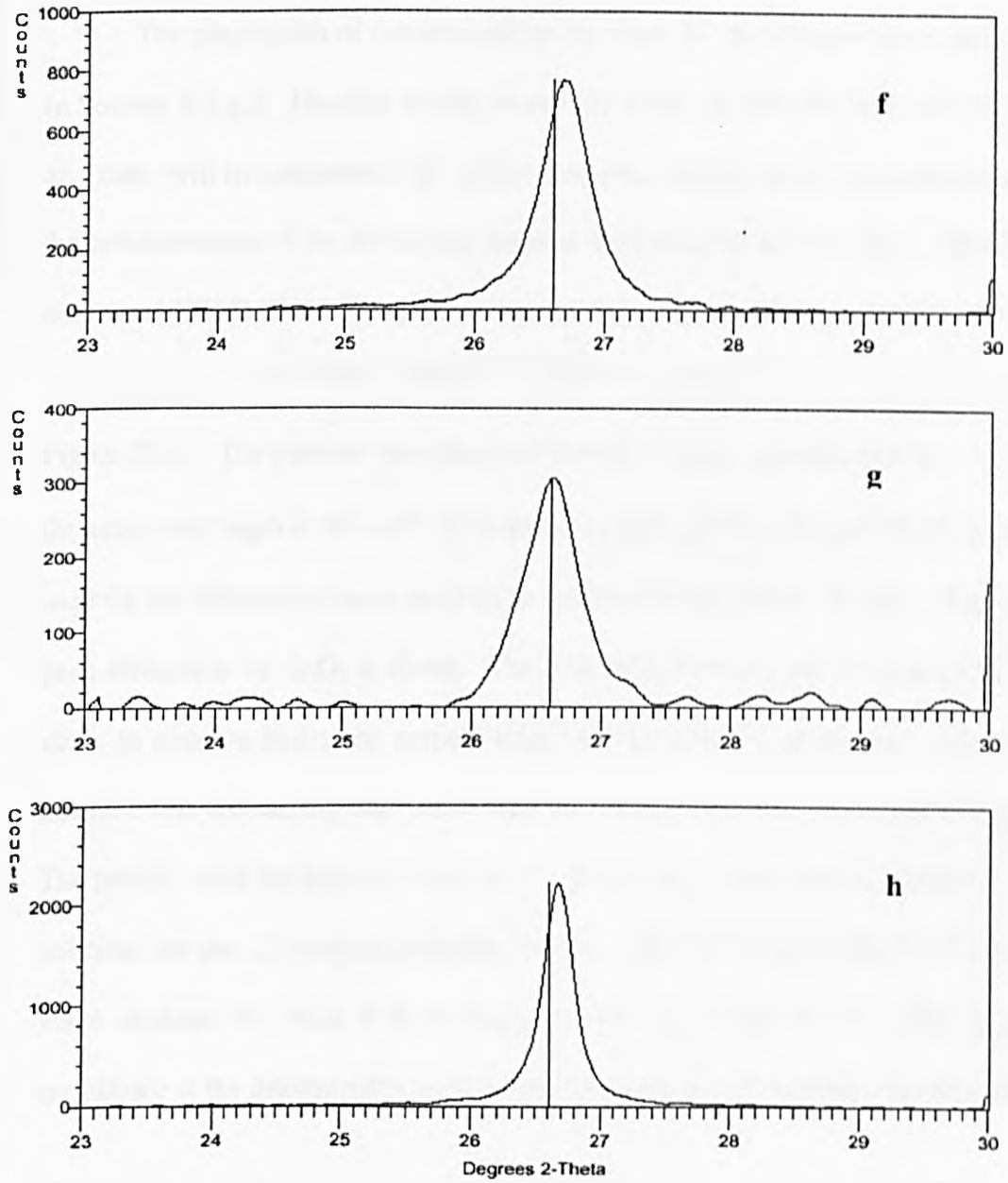

Figure III.32 (continued): The XRPD patterns for calcined tin oxide. Calcination for 60 minutes at (f) 800°C (g) 900°C, and (h) 1000°C. The solid lines are database positions for cassiterite.

III.5.b Nanocrystalline SnO_2 in porous silicas

The preparation of nanocrystalline tin oxide in 10 nm pore silica was described in Section II.1.g.2. Detailed studies were only made for samples with half filled pores, and these will be designated HF. Other than one XRPD for the as-prepared sample all the measurements of the diffraction patterns were made at the Daresbury SRS as part of combined XRPD/EXAFS studies on station 9.3. The samples were calcined at a series of temperatures from 500 to 1000°C. The XRPD patterns for the samples are shown in Figure III.33. The patterns have been converted to Cu K_α radiation and this is the reason the scans only begin at $2\theta = 45^\circ$. In order to collect both EXAFS and XRPD the radiation used for the diffraction has to be close to that for the EXAFS Sn K-edge. Thus the main peak diffraction for SnO_2 is absent. The peak at 51.6° was used to measure the particle size. In order to determine particle sizes via the Scherrer equation an estimate of the machine line broadening was made from the patterns for bulk SnO_2 and a Si standard. The particle sizes are listed in Table III.13. It is worth noting that the particle size of the unheated sample (2.3 nm) is consistent with the value measured at UKC (2.0 nm) and the value obtained for SnO_2 without silica (2.1 nm, see Table III.12). This gives some confidence in the determination of the particle size from the Daresbury measurement.

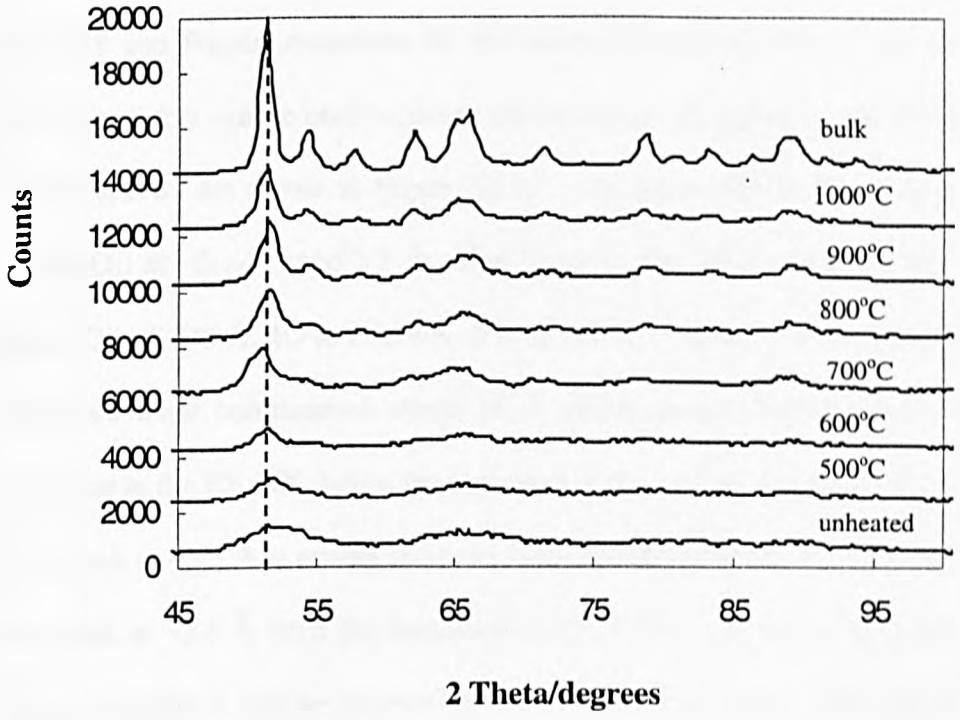

Figure III.33: The XRPD patterns for calcined tin oxide in 10 nm pore silica samples. Patterns were collected on the Daresbury SRS. Calcination for 60 minutes at the temperatures indicated on the patterns. The dashed line is a database position for cassiterite.

Table III.12

Tin oxide particle sizes in 10 nm pore silica

Calcining temperature/°C	Calcining time/minutes	Particle size/nm
25		2.3 (2.0*)
500	60	4.4
600	60	8.7
700	60	8.7
800	60	12.8
900	60	26.1
1000	60	26.1

(* Particle size determined on laboratory XRPD system at UKC)

EXAFS spectra were collected for the samples at the same time as the XRPD patterns were measured on station 9.3 at the Daresbury SRS. The full results, i.e. the EXAFS and Fourier transform for the sample heated at 1000°C are shown in Figure III.34, and this can be used to judge the quality of the spectra. The Fourier transforms of the spectra are shown in Figure III.35. The figure shows that there are three peaks for SnO_2; at ~2, ~3.5 and 3.8 Å. The X-ray crystal structure (see Table III.13) shows that 2O at 2.045 Å, 4O at 2.058 Å, 2Sn at 3.185 Å, 4O at 3.594 Å and 8Sn at 3.708 Å. The two inner coordination shells of O atoms are so close that they would not be resolved in the EXAFS, hence the first peak in the Fourier transform is due to 6O atoms. The peak at ~3.5 Å is arising from the back-scattering of the Sn atoms (at 3.185 Å) and the peak at ~3.8 Å from the back-scattering of the 8 Sn atoms (at 3.708 Å). The 4O atoms at 3.594 Å will be contributing to the two outer peaks. Thus the EXAFS of bulk SnO_2 was fitted to four shells using the crystallographic data as a starting model, slightly simplified with 6O atoms placed at 2.05 Å for the inner shell. As can be seen from Table III.13 the fit is excellent and the radial distances agree well with the crystallographic data (to within an expected error of ± 0.02 Å).

The EXAFS for the SnO_2 nanocrystals in the silica pores show a distinct change of Fourier transform as the samples are heated. For the unheated samples, i.e. smallest particle size, the two outer peaks are much smaller than for the bulk material. As the samples are heated and the particles grow, these two peaks grow in intensity. The effect is clearly due to the nanocrystalline nature of the samples. There has been considerable debate over the origin of the reduced magnitude of the outer peaks in the EXAFS of nanocrystals (Davis et al, 1997, Chadwick and Rush, 2001). It could arise from disorder in the samples (an affect on the Debye-Waller factor) or simple due to the small size (an affect on the average co-ordination number). Thus there are several approaches to

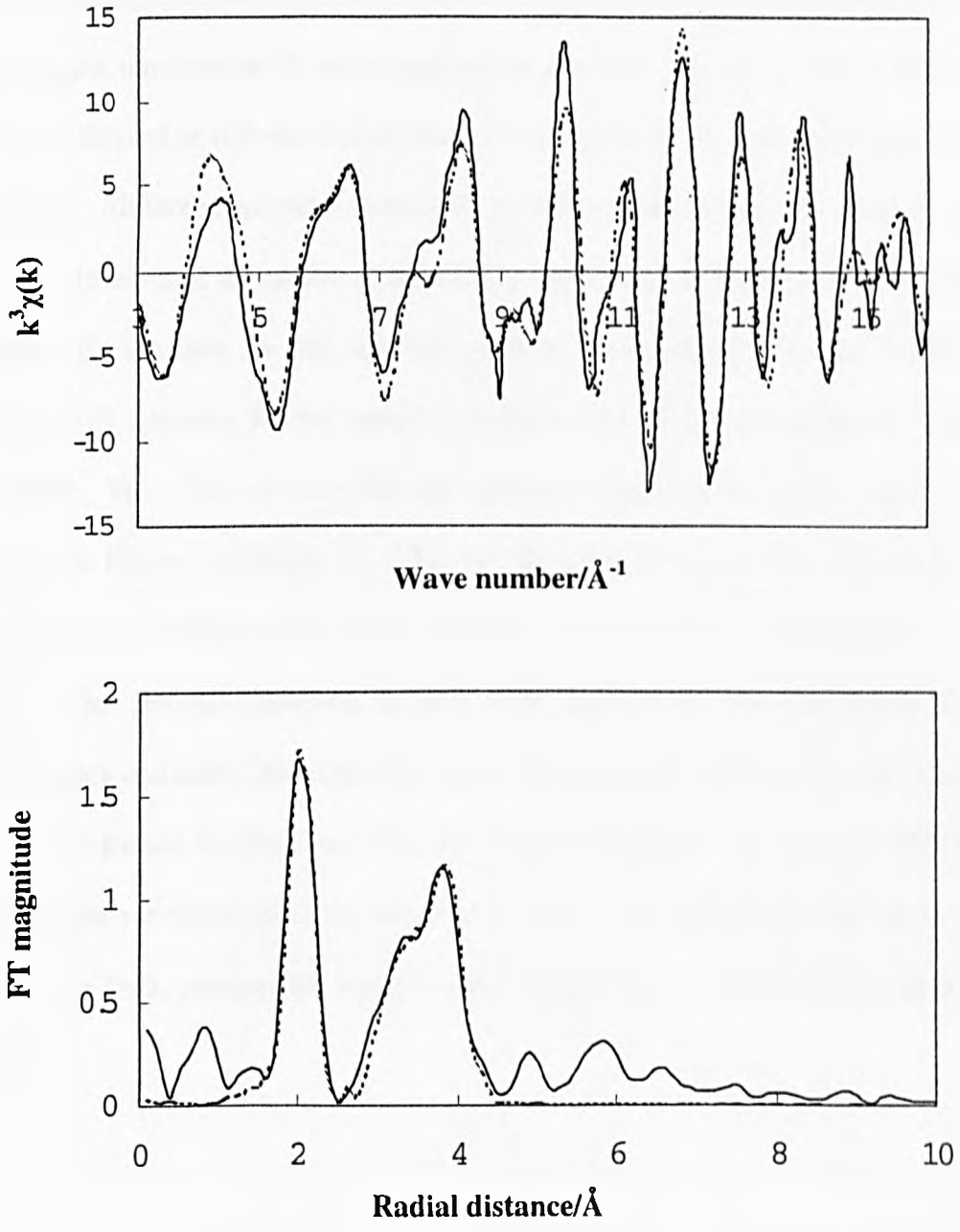

Figure III.34. The Sn K-edge EXAFS for SnO_2 in 10 nm pore silica after calcining at 1000°C. The upper plot is the EXAFS and the lower plot the corresponding Fourier transform. The solid lines are the experimental results and the dashed lines are for the best fit model. (R-factor = 35%)

the analysis of the EXAFS data of nanocrystals. Starting from the crystallographic data as the fitting model then (i) the Debye-Waller factors can be iterated with fixed co-ordination numbers or (ii) the co-ordination numbers with fixed Debye-Waller factors can be iterated or (iii) the Debye-Waller factors and the co-ordination numbers can be iterated. All three approaches were used in this work and the results are shown in Table III.13. In terms of the quality of the fits, i.e. the R factors, there is very little difference. Model (i) accounts for the reduced peaks by increasing the Debye-Waller factors. Model (ii) accounts for the reduced peaks by decreasing the average co-ordination number. The effect of using the two different models as the particle size changes is shown in Figures III.36 and 37. The co-ordination number can be calculated from the particle sizes (Wilson et al, 1994) and these agree well with those derived from Model (ii). The general consensus is now that nanocrystals are not highly disordered (Chadwick and Rush, 2001) and the current results are consistent with that picture.

It should be noted here that the reduced magnitude of the outer EXAFS peaks were clearly evident for SnO_2 but not for ZrO_2. The difference is due to the particle sizes; the SnO_2 particles are much smaller and the effects only become important at ~2 nm.

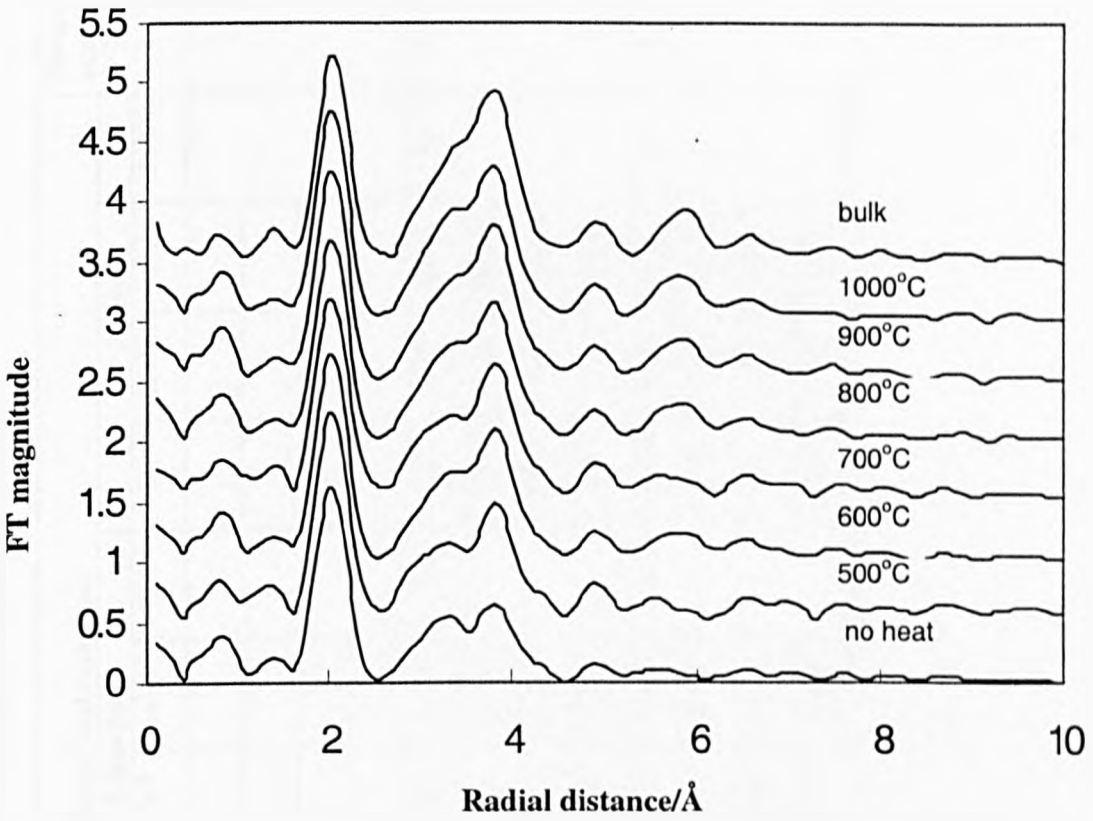

Figure III.35 The Fourier transforms of the Sn K-edge EXAFS for SnO_2 in 10 nm pore silica after calcining at various temperatures for 60 minutes. The temperatures are indicated on the plots. Successive plots have been displaced by 0.5 units for clarity.

Table III.13

Best fit parameters to the EXAFS results for tin oxide in 10 nm silica.

Sample	Atom	Starting Model/Fixed Parameters												Particle size/nm
		X-Ray/CN				X-Ray/$2\sigma^2$				X-Ray				
		CN	RD/Å	$2\sigma^2$/Å^2	R/%	CN	RD/Å	$2\sigma^2$/Å^2	R/%	CN	RD/Å	$2\sigma^2$/Å^2	R/%	
Bulk	O	6	2.05	0.004	33									
	Sn	2	3.21	0.005										
	O	4	3.61	0.013										
	Sn	8	3.73	0.007										
Unheated	O	6	2.05	0.005	35	6.0	2.05	0.004	36	6.9	2.05	0.007	33	2.3
	Sn	2	3.21	0.007		1.5	3.21	0.005		3.0	3.21	0.010		
	O	4	3.52	0.032		4.8	3.58	0.013		6.61	3.60	0.013		
	Sn	8	3.72	0.014		3.41	3.72	0.007		3.8	3.72	0.008		
500^{0}C	O	6	2.05	0.005	39	6.4	2.05	0.004	37	7.2	2.05	0.006	35	4.4
	Sn	2	3.21	0.007		1.5	3.20	0.005		5.6	3.20	0.013		
	O	4	3.66	0.017		4.4	3.45	0.013		8.6	3.60	0.007		
	Sn	8	3.72	0.010		5.6	3.71	0.007		4.1	3.72	0.006		

Table III.13

Best fit parameters to the EXAFS results for tin oxide in 10 nm silica.

Sample	Atom	Starting Model/Fixed Parameters												Particle size/nm
		X-Ray/CN				X-Ray/$2\sigma^2$				X-Ray				
		CN	RD/Å	$2\sigma^2$/Å^2	R/%	CN	RD/Å	$2\sigma^2$/Å^2	R/%	CN	RD/Å	$2\sigma^2$/Å^2	R/%	
600°C	O	6	2.04	0.005	35	6.4	2.04	0.004	35	7.2	2.05	0.006	34	8.7
	Sn	2	3.20	0.006		1.85	3.20	0.005		4.2	3.20	0.011		
	O	4	3.50	0.030		2.61	3.56	0.013		3.81	3.55	0.001		
	Sn	8	3.72	0.009		6.01	3.72	0.007		3.74	3.73	0.003		
700°C	O	6	2.04	0.005	38	6.3	2.04	0.004	37	7.0	2.05	0.006	36	8.7
	Sn	2	3.20	0.006		1.9	3.20	0.005		4.2	3.20	0.010		
	O	4	3.47	0.031		3.1	3.51	0.013		4.9	3.55	0.001		
	Sn	8	3.72	0.009		6.4	3.72	0.007		4.3	3.72	0.004		
800°C	O	6	2.05	0.005	35	6.2	2.05	0.004	34	6.7	2.05	0.006	34	12.8
	Sn	2	3.20	0.005		1.9	3.20	0.005		4.3	3.20	0.011		
	O	4	3.48	0.030		3.1	3.57	0.013		4.7	3.56	0.001		
	Sn	8	3.72	0.009		6.4	3.72	0.007		4.0	3.73	0.004		

Table III.13

Best fit parameters to the EXAFS results for tin oxide in 10 nm silica.

Sample	Atom	Starting Model/Fixed Parameters												Particle size/nm
		X-Ray/CN				X-Ray/$2\sigma^2$				X-Ray				
		CN	RD/Å	$2\sigma^2$/Å^2	R/%	CN	RD/Å	$2\sigma^2$/Å^2	R/%	CN	RD/Å	$2\sigma^2$/Å^2	R/%	
900°C	O	6	2.05	0.004	36	6.4	2.04	0.004	35	7.0	2.05	0.006	35	26.1
	Sn	2	3.20	0.005		2.1	3.19	0.005		3.5	3.20	0.008		
	O	4	3.47	0.028		2.2	3.54	0.013		3.6	3.56	0.001		
	Sn	8	3.72	0.008		7.4	3.72	0.007		4.7	3.73	0.004		
1000°C	O	6	2.04	0.004	36	6.43	2.04	0.004	35	7.0	2.05	0.006	35	26.1
	Sn	2	3.20	0.004		2.21	3.20	0.005		3.3	3.20	0.008		
	O	4	3.54	0.025		3.05	3.57	0.013		3.0	3.56	0.001		
	Sn	8	3.72	0.008		7.3	3.72	0.007		5.1	3.72	0.005		
X-ray crystallographic data (Yogyo Kyokai Shi (= Journal of the Ceramic Assoc. Of Japan) Seki H, Ishizawa N, Mizutani N, Kato M														
	O	2	2.045											
	O	4	2.058											
	Sn	2	3.185											
	O	4	3.594											
	Sn	8	3.708											

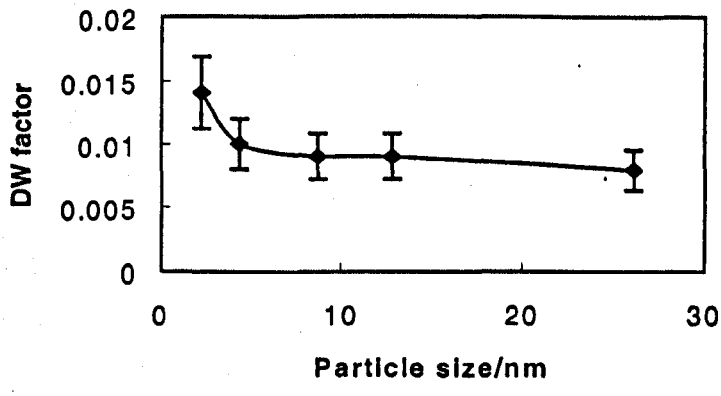

Figure III.36: The variation of Debye-Waller factor for second Sn shell with particle size with CN held at crystallographic number.

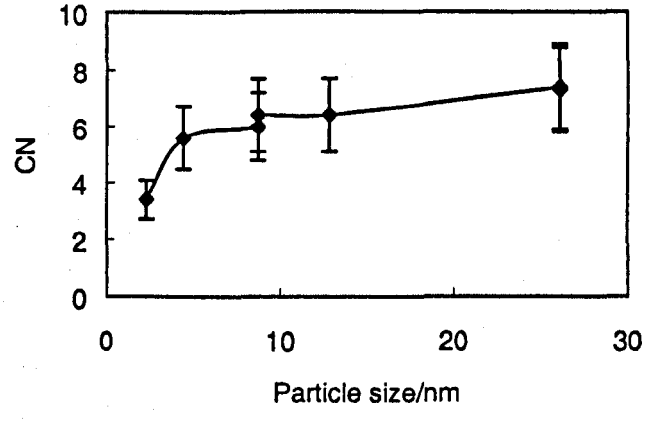

Figure III.37: The variation of CN for second Sn shell with particle size with Debye-Waller factor held at bulk tin oxide value.

III.5.c Nanocrystalline SnO_2 with alumina

The preparation of the sample was described in Section II.1.g.3 and was estimated to contain nominally 3% by weight of Al_2O_3 (equivalent to 5% by volume). Samples were calcined for 60 minutes at a series of temperatures up to 1000°C. After each calcination a XRPD pattern was collected and some of the results are shown in Figure III.38. The sizes of the particles after each calcination are shown in Table III.14. A comparison with the results for pure tin oxide shows that the particles with alumina grow significantly slower; the particle sizes after a 1000°C calcination are 88 and 35 nm, respectively.

Table III.14

Particle sizes in nanocrystalline tin oxide – 3% alumina

Calcining temperature/°C	Calcining time/minutes	Particle size/nm
25		2.1
400	60	4.1
500	60	6.9
600	60	11.6
700	60	19.3
800	60	21.8
900	60	25.7
1000	60	35.4

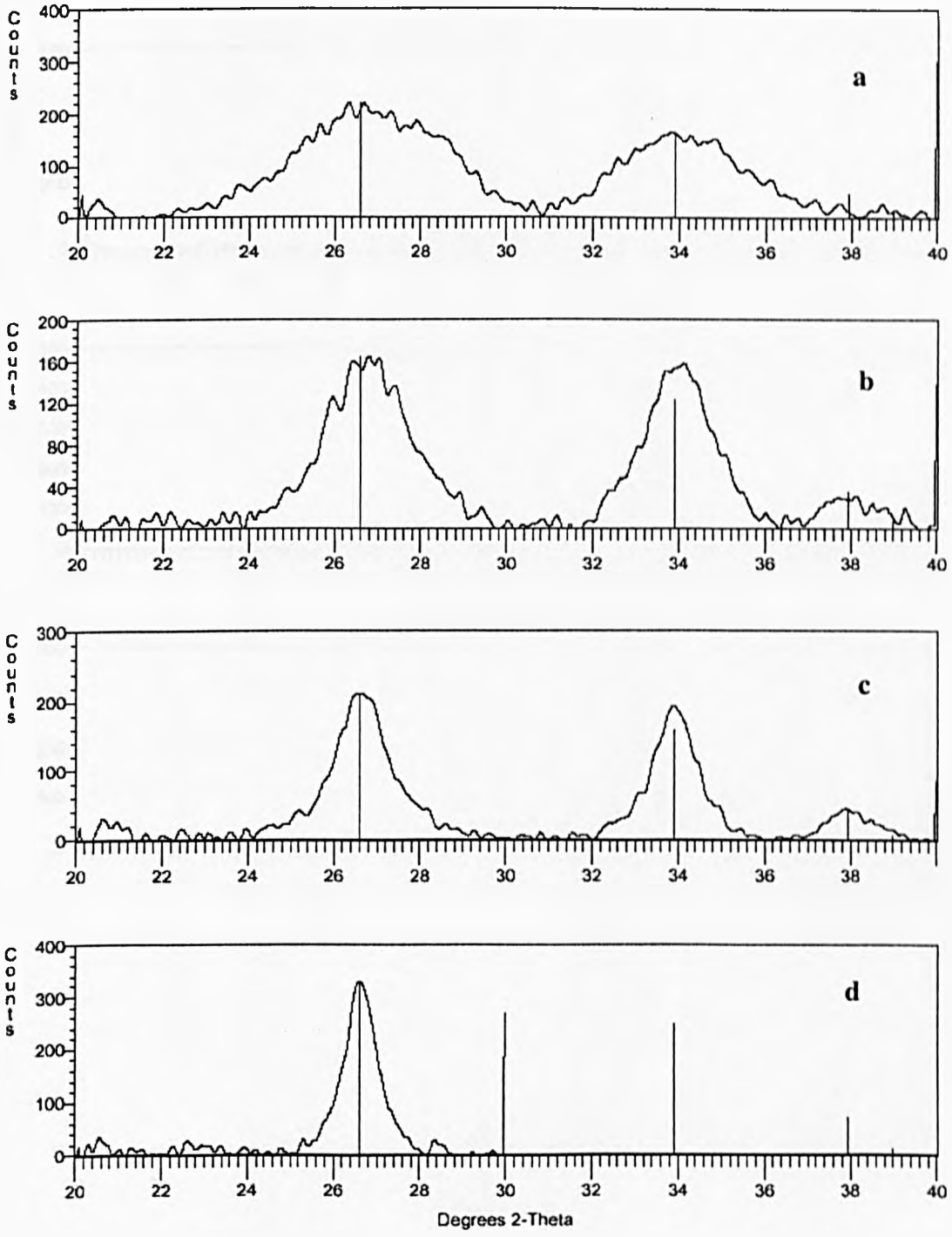

Figure III.38: The XRPD patterns for calcined tin oxide – 3% alumina. Calcination for 60 minutes at (a) no heat (b) 400°C, (c) 500°C, and (d) 600°C. The solid lines are database positions for cassiterite.

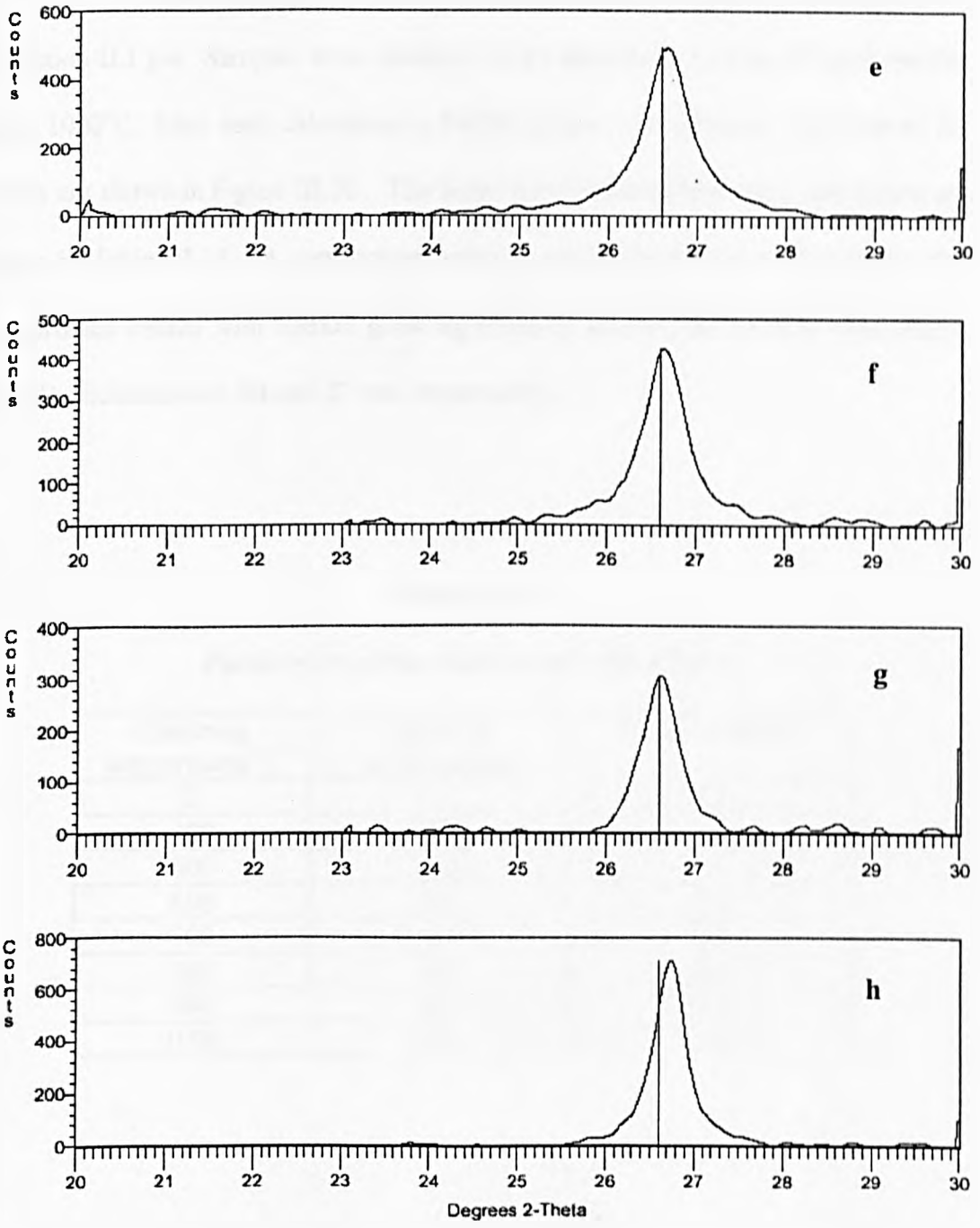

Figure III.38 (continued): The XRPD patterns for calcined tin oxide – 3% alumina. Calcination for 60 minutes at (e) 700°C, (f) 800°C, (g) 900°C, and (h) 1000°C. The solid line is a database position for cassiterite.

III.5.d Nanocrystalline SnO_2 with HMDS

The treatment of nanocrystalline tin oxide with HMDS was described in Section II.1.g.4. Samples were calcined for 60 minutes at a series of temperatures up to 1000°C. After each calcination a XRPD pattern was collected and some of the results are shown in Figure III.39. The sizes of the particles after each calcination are shown in Table III.15. A comparison with the results for pure tin oxide shows that the particles treated with HMDS grow significantly slower; the particle sizes after a 1000°C calcination are 88 and 27 nm, respectively.

Table III.15

Partice sizes of tin oxide treated with HMDS.

Calcining temperature/°C	Calcining time/minutes	Particle size/nm
25		2.1
400	60	3.2
500	60	4.9
600	60	8.4
700	60	13.6
800	60	16.2
900	60	18.8
1000	60	27.3

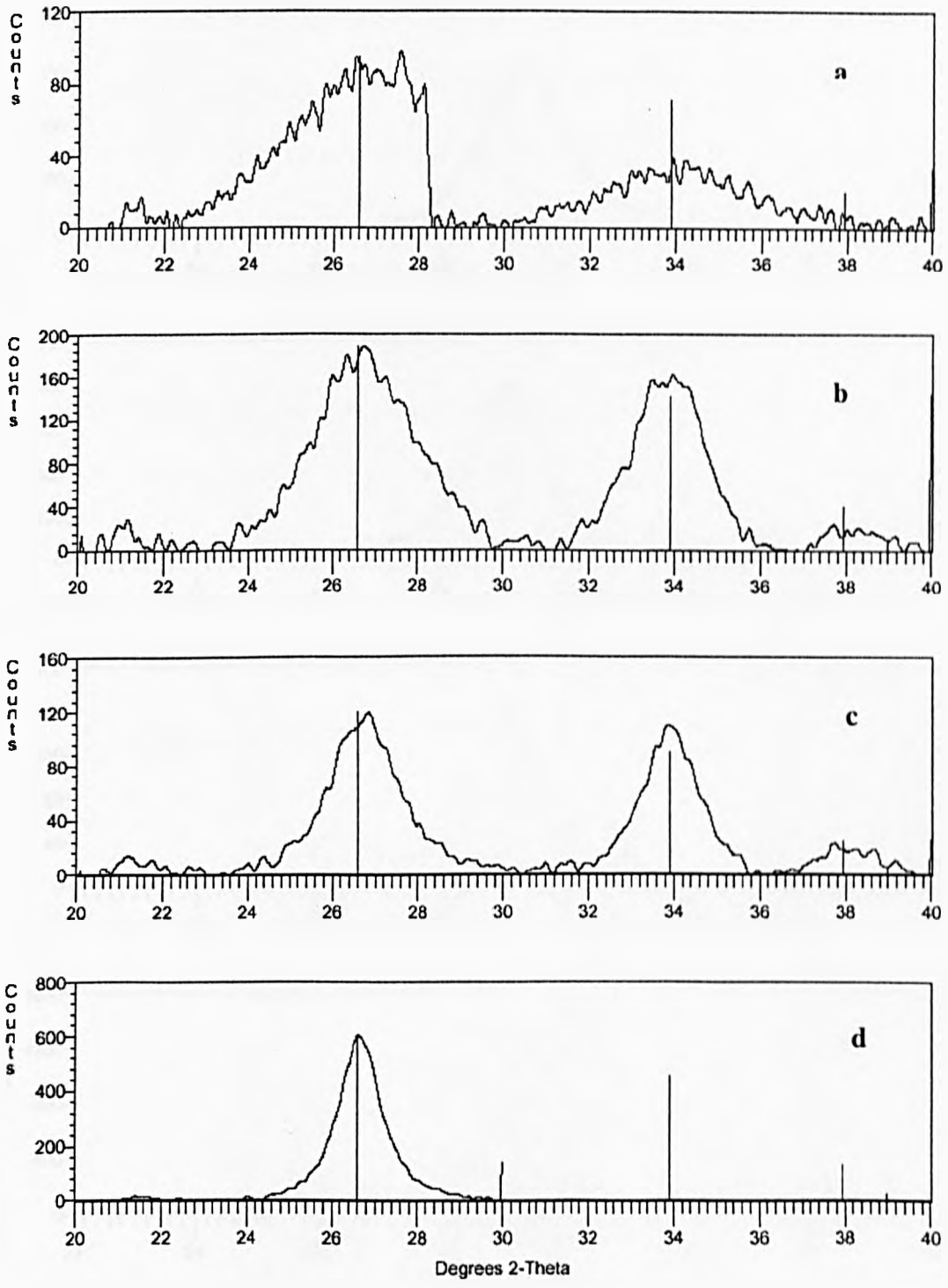

Figure III.39: The XRPD patterns for calcined tin oxide treated with HMDS. Calcination for 60 minutes at (a) no heat (b) 400°C, (c) 500°C, and (d) 600°C. The solid lines are database positions for cassiterite.

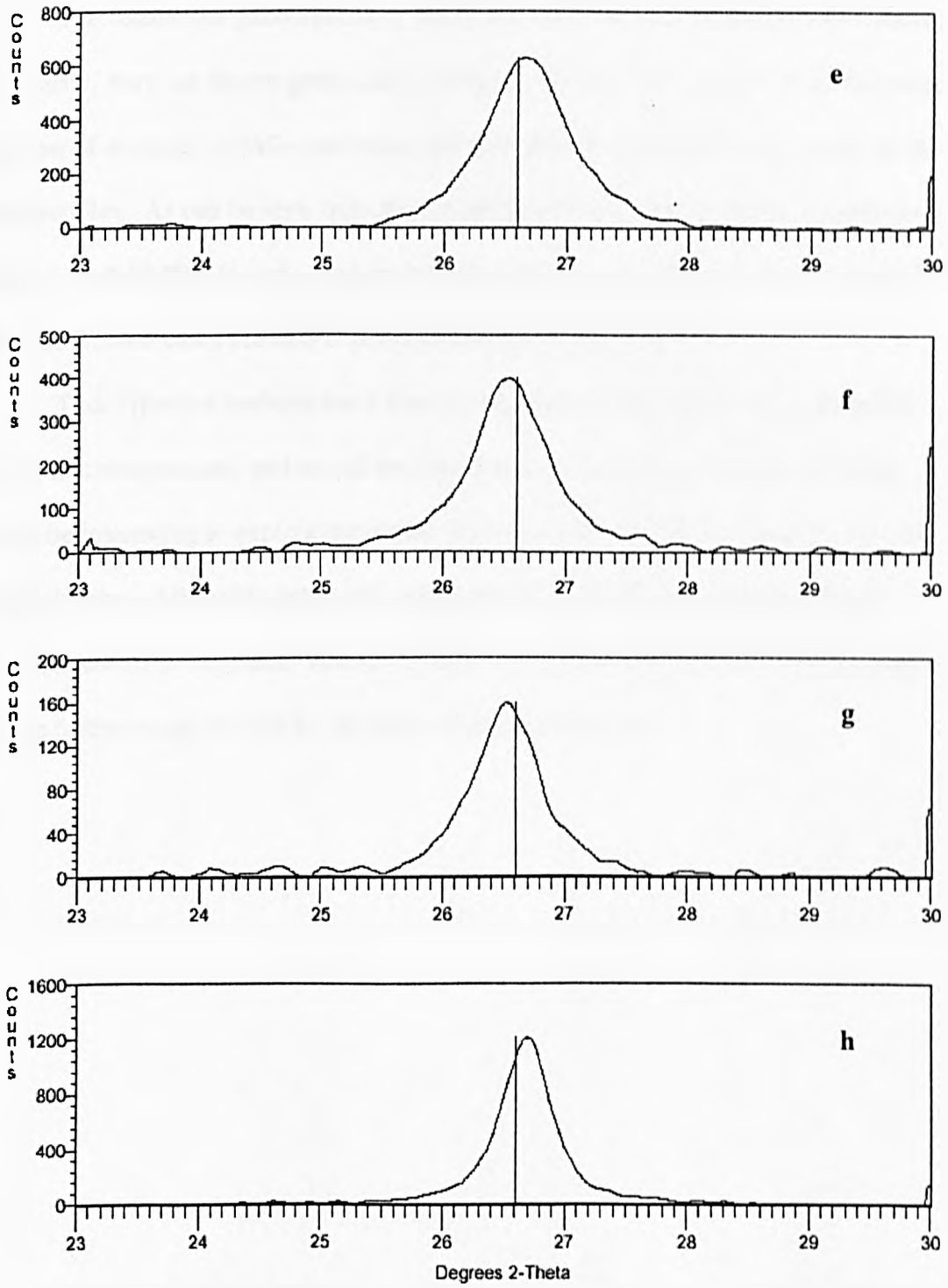

Figure III.39 (continued): The XRPD patterns for calcined tin oxide treated with HMDS. Calcination for 60 minutes at (e) 700°C, (f) 800°C, (g) 900°C, and (h) 1000°C. The solid line is a database position for cassiterite.

III.5.e Summary of the results for nanocrystalline SnO_2

The results for nanocrystalline SnO_2 are basically contained in Tables III.16. For clarity, they are shown graphically in Figure III.40. Precipitation in silica pores, addition of alumina to SnO_2 and treatment with HMDS all restrict the growth of the nanoparticles. As can be seen from the figure the effect of restricting the growth with alumina and HMDS is very similar in both cases up to calcining temperatures of 1000°C. In both cases the XRPD patterns only show peaks for SnO_2.

Thus effective methods have been developed to maintain nanocrystalline SnO_2 at elevated temperatures and one of the objectives of the project has been achieved. It would be interesting to explore the details of the treatments. For example, in the case of the alumina addition the effect of varying the concentration of alumina on grain growth needs to be explored. Also the details of the chemical and structural processes require further study, as will be discussed later in this chapter.

Table III.16

Comparison of tin oxide particle sizes after 60 minutes calcination with various preparation methods

Calcination temperature/°C	No treatment	3% alumina	HMDS	10 nm pore silica
25	2.1	2.1	2.1	2.3
400	3.6	4.1	3.2	
500	7.1	6.9	4.9	4.4
600	13.6	11.6	8.4	8.7
700	25.1	19.3	13.6	8.7
800	32	21.8	16.2	12.8
900	44.4	25.7	18.8	26.1
1000	87.8	35.4	27.3	26.1

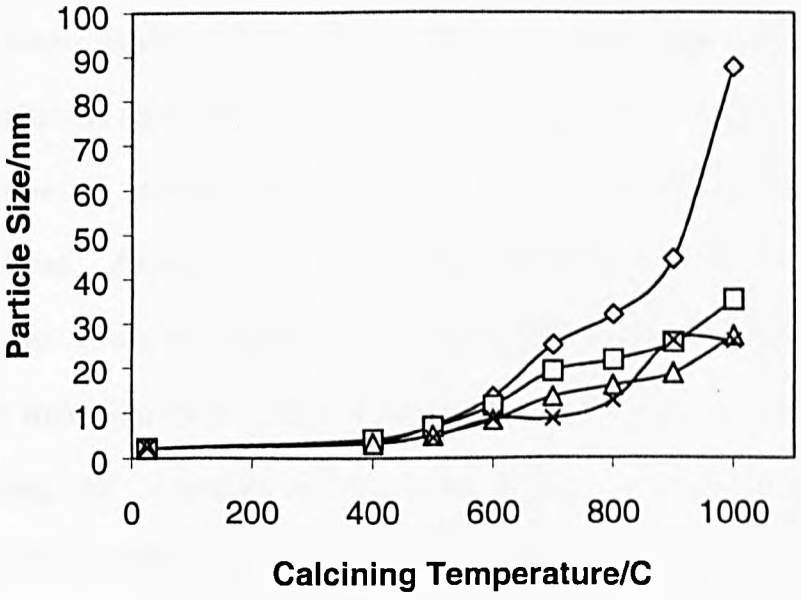

Figure III.40: A summary of the effect of calcining on particle size of tin oxide with various treatments. ✧ Pure tin oxide; tin oxide with 3% alumina; △ tin oxide in 10 nm pore silica; X tin oxide treated with HMDS.

III.6 SUMMARY OF THE RESULTS FOR NANOCRYSTALLINE OXIDES

At this point it worthwhile to summarise the results and make some comparisons between the different systems. The conclusions of the studies will be covered in the next Chapter.

Generally three approaches were used to stabilise the particle sizes of the nanocrystals, namely confining them in the pores of a silica matrix, adding alumina to the nanocrystals and coating the surface of the nanocrystals with HMDS. On the whole all of the approaches had some degree of success. A discussion of the level of this success and the reasons for the success requires some consideration.

The basic idea of confinement of the nanocrystals inside a silica pore is straightforward; the particles cannot grow as they are restricted by the size of the pore. The idea is shown schematically in Figure III.41. For all the materials, MgO, ZrO_2, CeO_2 and SnO_2, this approach was effective in that after comparable calcination time and temperatures the nanocrystals in the porous silicas were smaller than those that were unconfined. However, there are clearly differences in the results for the different oxides, which are related to the method of preparing the confined oxide. Inserting the hydroxide or the alkoxide means that there is a considerable loss of material during the calcination to the oxide. The work on zirconia clearly demonstrates this problem. There was little zirconia in the small pore silica and the XRPD signal was not observable on the laboratory X-ray source. Thus this is a good method provided there are preparation techniques that allow a large quantity of oxide to be prepared inside the pores. An alternative solution is to use larger pore sizes, e.g. the Reatec 126 nm pore silica, and hence allow for a large loss of mass during the oxide formation. It is worth noting that Reatec produce silicas with a very wide range

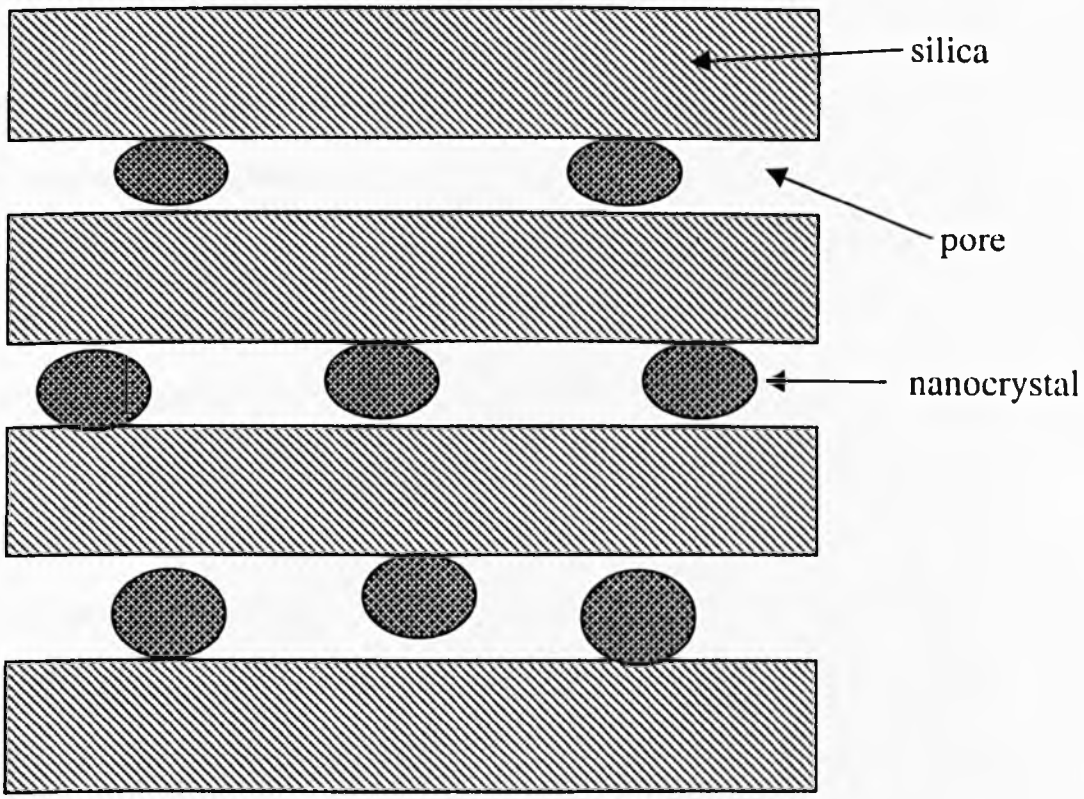

Figure III.41: A schematic picture of nanocrystals in pores.

of pore size, up to 200 nm, and in principle the pore size could be 'tuned' to produce the required amount of oxide. A second problem with the use of silica is that some oxides will react at high temperatures to produce silicates. An example of this is the work on magnesia, where heating above 800°C produced fosterite, Mg_2SiO_4. Thus the reactivity of the oxide with silica needs to be established if this method is to be employed.

A general question that has not been addressed so far is the size of the nanocrystals and the size of the pores. In all the systems that were examined the particle grew at high temperatures and exceeded the size of the pores. The work on ceria is a good example; heating samples prepared with 4 and 10 nm pore sizes to 800°C for 60 minutes resulted in ceria particles that were ~20 nm size ~5 times and 2 times the pore size. Other workers have observed a similar effect. Anderson et al (1996) used zeolites to confine cobalt oxide in the pores and then reduced the oxide to the metal. The work was performed with zeolite X which has pores of 1.3 nm diameter. The particle size of the cobalt was 15 to 20 nm, suggesting that the oxide particles must have been even larger. These authors suggested that the explanation was a disruption of the pore walls by the particles and not a movement of the particles out of the pores. A similar explanation can be invoked here. It should be noted that one of the special properties of nanocrystals is their superhardness as they are free from dislocations. This silica is not highly crystalline as evidenced by the lack of peaks in the XRPD patterns and from the manufacturer's literature. The particles will therefore be much harder than the silica and could easily break through the silica walls.

The use of alumina additions to stabilise the nanocrystals was applied to MgO, ZrO_2 and SnO_2 and was generally successful in all cases. The alumina is assumed to

form between the crystallites and prevent their growth by pinning the boundaries. The effect is shown schematically in Figure III.42. In all the systems studied XRPD patterns for alumina were not observed. The simplest conclusion is that the alumina particles are too small to give a diffraction peak. Some comments are necessary for the different systems. In the case of MgO and ZrO_2 the alumina was introduced at the first stage of the preparation, by mixing the alkoxides, and the alumina particles were formed at the same time as the metal oxide nanocrystals. In the case of ZrO_2 there is clearly some complex chemistry occurring, as the temperatures required for conversion of the zirconium hydroxide to zirconia are considerable increased. In the case of MgO there is a reaction with the Al_2O_3 at high temperatures with the formation of a spinel. Thus this approach to stabilising MgO nanocrystals has a distinct limitation. In the case of SnO_2 the nanoparticles were prepared first and then the alumina produced on the nanocrystals. This appears to be a satisfactory procedure that in principle could be generally applied to any oxide.

The use of HMDS coatings was only used to stabilise SnO_2 nanocrystals and appears to be very effective. Other workers have used this with a variety of oxides (Wu et al, 1999). Clearly what is happening is that the HMDS is reacting with surface OH on the oxide to produce a thin coating of silica. This silica keeps the oxide particles out of contact and prevents their sintering and growth. However, it is worth noting that silica is relatively reactive with many other oxides (although a tin silicate does not appear to exist on the crystallographic databases) and this approach may fail at high temperatures.

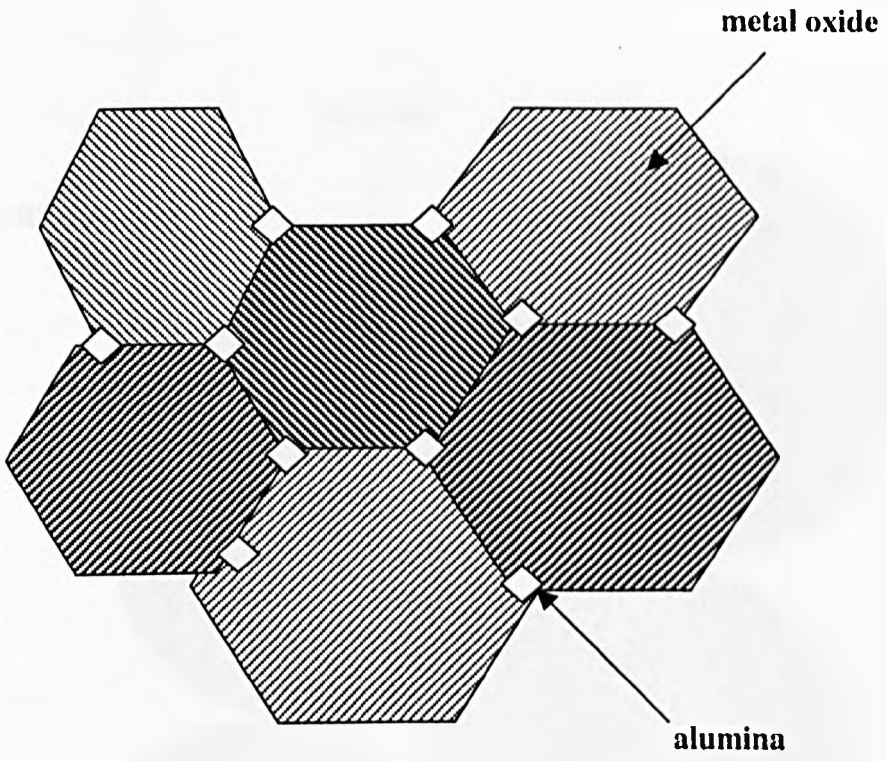

Figure III.42: A schematic picture of alumina particles in the grain boundaries between nanocrystals

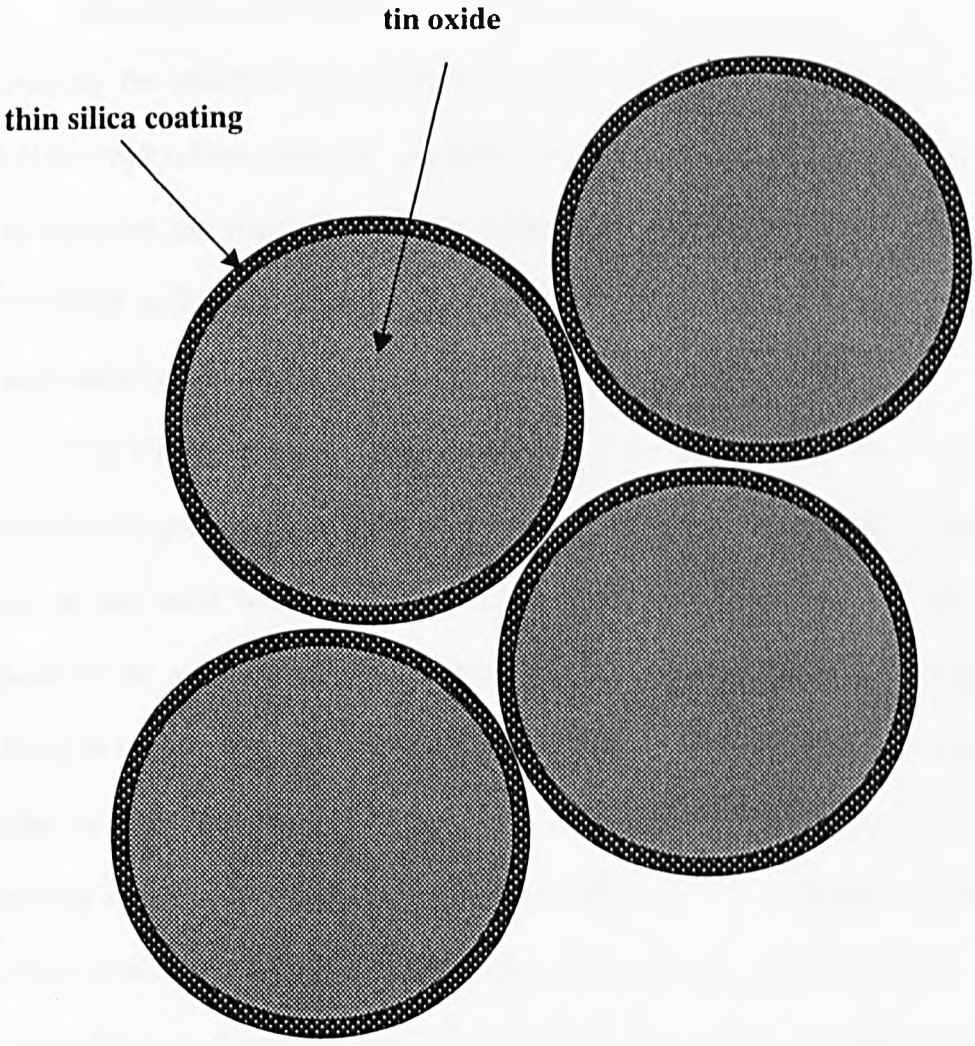

Figure III.43: A schematic picture of silica coated nanocrystals.

IV CONCLUSIONS AND SUGGESTIONS FOR FUTURE WORK

IV.1 CONCLUSIONS

The objective of the work described in this thesis was to find methods of preventing the growth of nanocrystalline oxides when they are heated. On the whole the objective has been achieved. A variety of methods to prevent the grain growth have been explored and most of them were successful. The main results of the work are summarised in Table IV.1, which collects together the particle sizes of untreated and treated nanocrystals after heating for 60 minutes at 600, 800 and 1000°C.

It is clearly of interest to consider which of the methods used is the best at restricting the grain growth. The answer, as can be seen from Table IV.1, depends very much on the oxide being studied. Confining the nanocrystals on the pores of silica appears to be effective for all the materials that were investigated. However, it is difficult to introduce material into the pores in large quantities, as can be seen from the studies of ZrO_2 described in Section III.2.b.1. This would be the best method of preparing samples for the NMR diffusion studies that were proposed in Section I.4. Addition of alumina, via the butoxide, seems to be generally effective for all the oxides, however there are clearly problems with MgO due to reactivity. Treatment with HMDS was very effective in reducing growth in SnO_2 and it would be extremely interesting to explore this treatment with other oxides.

The mechanisms for the prevention of the grain growth were discussed in Section III.6. In the case of nanocrystals in the pores of silica it appears to be the simple case of the silica presenting a physical barrier between the crystallites. The addition of alumina creates small crystallites that pin the grain boundaries. The

treatment with HMDS coats the crystallites with a layer of silica to keep them out of mutual contact and prevents growth.

Table IV.1

Effect of treatment on particle size

Oxide	Method to prevent grain growth	Particle size/nm					
		600°C		800°C		1000°C	
		Pure	Treated	Pure	Treated	Pure	Treated
MgO	126nm silica	13	4.5	-	Mg_2SiO_4 Formed	-	Mg_2SiO_4 formed
	15% alumina	13	4.7	-	5.7	-	Spinel formed
ZrO_2	10nm silica half-filled	18	-	47	-	50	5
	10nm silica fully-filled	18	-	47	-	50	5.8
	126nm silica	18	8	47	8	50	-
	5% alumina	18	≤12	47	-	50	-
	10% alumina	18	≤10	47	-	50	-
	15% alumina	18	-	47	11	50	12
CeO_2	4nm silica	12.2	12.3	48	18.5	-	79
	10nm silica	12.2	12.5	48	19.6	-	64
SnO_2	10nm silica	13.6	8.7	32	12.8	88	26.1
	3% alumina	13.6	11.6	32	21.8	88	35.4
	HMDS	13.6	8.4	32	16.2	88	27.3

IV.2 SUGGESTIONS FOR FUTURE WORK

The work presented in this thesis was an attempt to make a systematic study of the methods of preventing the growth of nanocrystalline oxides. As far as the author is aware this is the first study of this type. However, the time available for the work was limited and many questions are still left unanswered. It is therefore valuable to consider how the work could continue in the future and what improvements might be possible. These will be listed under simple headings and a few brief comments will be made.

Improvements of the present work

The work in the thesis was exploratory. The prime system for study was ZrO_2 and most of the time on the project was spent studying this system. There are clearly some gaps, that would have been filled if time had been available. For example, HMDS treatment seems to be a very good way of preventing grain growth and it was only used with SnO_2. It would have been interesting to try this method with the other oxides. Similarly, CeO_2 is a very important fuel cell oxide and more work on preventing grain growth in this system would have been very useful. There were also gaps in the annealing of the samples and, given time, it would have been useful to have a set series of temperatures applied to all the samples.

The use of other porous matrices

Confining the nanocrystals into the pores of silica was generally found to be an effective method of preventing grain growth. However, only a few pore sizes were studied in this thesis and a systematic study of the effect of pore size on particle growth would be fruitful. For example, a study of the growth of ZrO_2 in pores ranging from 1 to 1000nm would be very useful. In addition, there is a wide range of other porous

matrices that could be used. Porous alumina is worthy of exploration as alumina is generally less reactive than silica.

The effect of the concentration of alumina

Addition of alumina was very effective in preventing the growth of the oxides studied in this thesis. It was particularly useful, as the preparative method was very simple, and large quantities of sample were easily made. However, the quantities of alumina that were added were simply taken from previous papers, e.g. 5, 10 and 15% in the case of ZrO_2 and no attempt was made to determine the most effective concentration of additive. This could very usefully and easily be explored and the optimum composition determined.

The use of other methods of characterisation

The range of methods of characterising the samples was limited to XRPD, EXAFS and DSC. Whilst they were adequate in assessing the effect of the treatments it would be very worthwhile to use some other methods. The most obvious would be to study the samples with high-resolution electron microscopy (HRTEM). This gives a picture of the microstructure and show where the additives were exactly in the material. For example, the alumina additive should be identifiable as a separate phase. In addition, HRTEM would also provide an estimate of the individual grain sizes to supplement the average values obtained by XRPD.

Transport measurements

One of the objectives of the current study was to prepare materials suitable for transport studies by NMR. As this has been achieved it is clearly important that these measurements are performed. In the light of the interest in the ionic conductivity of nanocrystals (Sata et al, 2000), these would be extremely informative. In addition,

simple a.c. conductivity measurements on the nanocrystals would be useful. For example, Kosacki (2002) finds a high conductivity in nanocrystalline ZrO_2. It would be interesting to see if the nanocrystalline ZrO_2 with added alumina also shows a high conductivity.

Chemical reactivity

There has been considerable interest in the use of nanocrystalline oxides as adsorbers for pollutant gases and Klabunde and co-workers have published several papers on this topic (Klabunde et al, 1996, Koper et al, 1997, Stark et al, 1996). The materials produced in this thesis are worth study as they are stable at high temperatures and could be easily regenerated. For example, Klabunde's work has shown nanocrystalline MgO is a good adsorber of SO_2. However, the removal of SO_2 from the MgO would require heat and the nanocrystals would be lost. The stabilised MgO made in this thesis would be stable on heating and potentially more useful. Very recently Klabunde's group have reported the formation of mixed MgO-alumina nanocrystals using an alkoxide synthesis similar to the one used in the current work (Carnes et al, 2002). They found the mixed material an even better adsorber than pure nanocrystalline MgO but they did not study the effect of heating the material.

REFERENCES

Akamatsu, K., Takei, S., Mizuhata, M., Kajinami, A., Deki, S., Takeoka, S., Fujii, M., Hayashi, S. and Yamamoto, K., 2000, *Thin solid films*, **359**, 60.

Al-Angari, Y., Savin, S.L.P, Rammutla, K.E., Pooley, M.P., van Eck, E.R.H. and Chadwick, A.V., 2002, *Radiation Effects and Lattice Defects in Solids*, in press

Anderson, P.A., Bell, R.G., Catlow, C.R.A., Chang, F.L., Dent, A.J., Edwards, P.P., Gameson. I., Hussain. I., Porch, A. and Thomas, J.M., 1996, *chem. Mat.*, **8**, 2114.

Anpo, M., 1989, *Res. Chem. Intermediates*, **11**, 67.

Badwal, S.P.S., 1990, *Applied Physics A*, **50**, 449.

Bai, C.L., 2001, *J. Nanoparticle Res.*, **3**, 251.

Barrer, R.M., 1958, *J. Chem. Soc.*, 299.

Barrer,R.M,, 1983, *J, Inclusion Phenom.*, **1**, 105.

Barsan, N., Schweizer-Berberich, M. and Gopel, W., 1999, *Fresenius J. Anal. Chem.*, **365**, 287.

Bearman, K., 2000. *Final year project report,* School of Physical Sciences, University of Kent.

Berman, G.P., Doolen, G.D. and Tsifrinovich, V.I., 2000, *Superlattices and Microstructures*, **27**, 89.

Betz, U., Sturm, A., Loffler, J.F., Wagner, W., Wiedenmann, A. and Hahn, H., 2000, *Mat. Sci. Eng., A.*, **281**, 68.

Binsted, N., Campbell, J.W., Gurman, S.J. and Stephenson, P.C., *SERC Daresbury Program Library*, 1992, Daresbury Laboratory, Warrington, Cheshire WA4 4AD, UK.; Binsted N. 1998. EXCURV98: *CCLRC Daresbury Laboratory computer program.*

Birdi, K.S., 1999, *J. Dispersion Sci. Tech.*, **20**, 795.

Birkby, I and Stevens, R, 1996, A*dvanced Ceramic Materials; Key Eng.Materials*,**122,** 527.

Birringer, R., Gleiter, H., Klein, H.P. and Marquardt, P., 1984, *Phys. Letts, A*, **102**, 365.

Carnes, C.L., Kapoor, P.N., Klabunde, K.J. and Bonevich, J., 2002, *Chem. Mat.*, **14,** 2922.

Cauqui MA, Rodriguez-Izquierdo, J.M., 1992, *J. Non-Cryst. Solids,* **147**, 724.

Chadwick, A.V., Russell, N.V., Whitham, A.R.and Wilson, A., 1994, *Sensors and Actuators*, **B18**, 99.

Chadwick, A.V., Maitland, D.T.S., Popplett, I.J.F. and Smith, M.E., 1998, *Chem, Mat.*, **10,** 864.

Chadwick, A.V. and Rush, G.E., 2001, in '*Nanocrystalline Metals and Oxides: Selected Properties and Applications*', eds P. Knauth and J. Schoonman, Kluwer, Boston.

Chadwick, A.V., Mountjoy, G., Nield, V.M., Poplett, I.J.F., Smith, M.E., Strange, J.H. and Tucker, M.G., 2001, *Chem. Mater.*, **13**, 1219.

Cohen, M.L. 2001, *Mat. Sci. Eng., C,* **15**, 1.

Comini, E., Sberveglieri, G., Ferroni, M., Guidi, V., Frigeri, C. and Boscarino, D., 2001, *J. Mat. Res.*, **16**, 1559.

Cui, Z.L. 1999, *J. Mat. Sci. Tech.* **15**, 71.

Cullity, J.B.D., 1978, *Elements of X-ray Diffraction*, 2nd Edition, Addison Wesley, Reading, MA, p.102.

Davis, A.P., 1999, *Nature*, **401**, 120.

Davis, S.R., 1997, *Ph.D. thesis,* University of Kent.

Davis, S.R., Chadwick, A.V. and Wright, J.D., 1997, *J. Phys. Chem .B.*, **101**, 9901.

Davis, S.R., Chadwick, A.V., Wright, J.D. 1998, *J. Mat. Chem.*, **8**, 2065.

Ding, X.Z. and Liu, X.H., 1997, *Mat. Sci. Eng. A.*, **224**, 210.

Drexler, K. E., 1986, *'Engines of Creation; The Coming Era of Nanotechnology'*, New York: Anchor Press/Doubleday; URL http://www.foresight.org/EOC/index.html.

Fahy, G.M., 1993, *Clinical Chemistry*, **39**, 2011.

Fang, G.J., Liu, Z.L. and Yao, K.L., 2002, *J. Inorg. Mat.*, **17**, 139.

Gajovic, A., Stubicar, M., Ivanda, M. and Furic, K.,2001, *J. Mol. Structure*, **563**, 315.

Garcia-Martinez, O, Rojas, R.M., Vila, E., DeVidales, J.L.M., 1993, *Solid State Ionics*, **63-5**, 443.

Garvie, R.C., 1965, *J. Phys. Chem.*, **69**, 1238.

Garvie, R.C., 1978, *J. Phys. Chem.*, **82**, 218.

Gleiter H. and Marquardt, P., 1984, *Z. fur Metallkunde*, **75** 263.

Gleiter, H., 1989, *Prog. Mat. Sci.*, **33**, 223.

Gleiter, H., 1992, *Adv. Mat.*, **4**, 474.

Gleiter, H., 2000, *Acta Materialia*, **48**, 1.

Gleiter, H., Weismuller, J, Wollersheim, O. and Wirschum, R., 2001, *Adv. Mater*, **49**, 737.

Harris, D.J., Harding, J.H. and Parker, S.C., 1999, *Rad. Eff. Latt. Def. Solids*, **151**, 299.

Harris, D.J., Watson, G.W. and Parker, S.C., 2001, *Phys.Rev. B.*, **64**, art. no.134101.

Hirano, M and Kato, E., 1996, *J.Ceram Soc. Japan,* **104,** 958.

Huh, M.Y., Kim, S.H., Ahn, J.P., Park, J.K. and Kim, B.K., 1999, *Nanostructured Mat.,* **11,** 211.

Indris, S., Bork, D. and Heitjans, P., 2000, *J. Mat. Synthesis and Processing,* **8,** 245.

Kenway, P.R., Oliver, P.M., Parker, S.C., Sayle, D.C.,Sayle, T.X.T. and Titiloye, J.O., 1992, Mol. Simulation, **9,** 83.

Kharton, V.V., Figueiredo, F.M., Navarro, L., Naumovich, E.N., Kovalevsky, A.V., Yaremchenko, A.A., Viskup, A.P., Carneiro, A., Marques, F.M.B. and Frade, J.R., 2001, *J. Mat. Sci.*, **36,** 1105.

Klabunde, K.J., Stark, J., Koper, O., Mohs, C., Park, D.G., Decker, S., Jiang, Y., Lagadic, I. and Zhang, D.J., 1996, *J. Phys. Chem.*, **100,** 12142.

Klug, H.P. and Alexander, L.E., 1974, *X-Ray Diffraction Procedures*, Wiley; New York.

Komiyama, H., Shimogaki, Y. and Egashira, Y. 1999, *Chem. Eng. Sci.*, **54,** 1941.

Kong, L.B., Zhu, W.G. and Tan, O.K., 1999, *Ferroelectrics,* **230,** 583.

Koningsberger, D.C. and Prins, R., 1988, *X-Ray Absorption. Principles, Applications, Techniques of EXAFS, SEXAFS and XANES*; Wiley; New York.

Koper, O., Lagadic, I. and Klabunde, K.J., 1997, *Chem. Mat.*, **9,** 838.

Kosacki, I., ., 2002, *Radiation Effects and Lattice Defects in Solids*, in press

Kosacki, I., Suzuki, T., Petrovsky, V. and Anderson, H.U., 2000, *Solid State Ionics,* **136,** 1225.

Lee, P.A. and Pendry, J.B., 1975, *Phys. Rev. B*, **11,** 2795.

Li Z.Q., Ramasamy, S, Hahn, and Siegel, R.W., 1988, *Mat. Letts.*, **6,** 195.

Liang, C.C., 1973, *J. Electrochem. Soc.*, **120,** 1289.

Lin, H.M., Keng, C.H. and Tung, C.Y., 1997, *Nanostructured Mat.*, **9,** 747.

Liu, H., Feng, L., Zhang, X. and Xue, Q., 1995, *J. Phys. Chem.*, **99**, 332.Maier, J., 1995, *Prog. Solid State Chem.*, **23**, 171.

Maier, J. And Tuller, H.L., 2000, *Solid State Ionics,* **131**, 1.

MacKenzie, K.J.D., Temuujin, .J, Smith, M.E., Angerer, P. and Kameshima, Y., 2000, *Thermochimica Acta,* **359**, 87.

McLellan, J., 2002, *Sunday Observer*, Life Magazine, 31, March, 2002 URL http://www.observer.co.uk/life/story/0,6903,675598,00.html

Mayo, M.J., 1997, *Nanostructured Mat.*, **9**, 717.

Mayo, M.J., Seidensticker, J.R., Hague, D.C. and Carim, A.H., 1999, *Nanostructured Mat.*, **11**,271.

Menon, A.K. and Gupta, B.K., 1999, *Nanostructured Mat.*, **12**, 1117.

Mukherjee, P., Patra, C.R., Kumar, R. and Sastry, M., 2001, ***Pnys. Chem. Comm.*, 5**, 1.

Nachimuthu, P., Shih, W.C., Liu, R.S., Jang, L.Y. and Chen, J.M., 2000, *J. Solid State Chem.*, **149**, 408.

Pesce, M., 2001, URL http://www.nanozine.com/NANOFOLK.HTM

Rao, C.N.R. and Cheetham, A.K., 2001, *J. Mat. Chem.*, **11**, 2887.

Roco, M.C., 2001, *J. Nanopart. Res.*, **3**, 353.

Rush, G.E., Chadwick, A.V. Kosacki, I. and Anderson, H.U., 2000, *J. Phys. Chem. B*, **104**, 9597.

Rush, G.E., 2001, *Ph.D. thesis,* University of Kent.

Rywak, A.A., Burlitch, J.M. and Loehr, T.M., 1995, *Chem. Mat.*, **7**, 2028.

Sata, N., Eberman, K., Eberl, K. and Maier, J., 2000, *Nature,* **408**, 946.

Sberveglieri, G., 1992, *Sensors and Actuators B,* **6**, 239.

Sberveglieri, G., 1995, *Sensors and Actuators B,* **23**, 103.

Scholz, G., Stösser, R, Klein, J., Silly, G., Buzaré, J.Y., Laligant, Y. And Ziemer, B., 2002, *J. Phys.: Condens. Matter*, **14**, 2101.

Shaw, N.J., 1989, *Powder Metallurgy International*, **21**, 31.

Seeman, N.C., 2001. *Nano Letts.*, **1**, 22.

Siegel, R.W., Hahn, H, Ramasamy, S., Zongquan. L., Ting, L. and Gronsky, R., 1988, *J de Physique*, **49**, (C-5), 681.

Siegel, R.W., Ramasamy, S., Hahn, H., Li, Z.Q., Lu, T. and Gronsky, R., 1988, *J. Mat. Res.*, **3**, 1367.

Srivastava, O.K. 1967, *Can. J. Chem.*, **45**, 585.

Stark, J.V. and Klabunde, K.J., 1996, *Chem. Mat.*, **8**, 1913.

Stark, J.V., Park, D.G., Lagadic, I. and Klabunde, K.J., 1996, *Chem. Mat.*, **8**, 1904.

Suzuki, T., Kosacki, I., Petrovsky, V. and Anderson, H.U., 2002, *J. Appl. Phys.*, **91**, 2308.

Tang, J.M., Uehara, M., Enomoto, N., Hojo, J. and Nakagawa Z.E., 2001, *J. Ceram. Soc. Japan*, **109**, 201.

Tuller, H.L., 2000, *Solid State Ionics*, **131**, 143.

Turi, E.A., 1997, *Thermal Characterization of Polymeric Materials*. Academic Press, New York.

Turillas, X., Barnes, P., Gascoigne, D., Turner, J.Z., Jones, S.L., Norman, C.J., Pygall, C.F. and Dent, A.J., 1995, *Radiation Phys. Chem.*, **45**, 491.

Utamapanya, S, Klabunde. K.J. and Schlup, J.R., 1991, *Chem. Mat.*, **3**, 175.

Veith, M., Altherr, A., Lecerf, N., Mathur, S, Valtchev, K. and Fritscher, E., 1999, *Nanostructured Mat.*, **12**, 191.

Viswanath, R.N. and Ramasamy, S., 1999, *Nanostruct. Mater.*, **12**, 1085; 1999, *J Mater Sci.*, **34**, 2879.

Whatmore R.W., 1999, *Ferroelectrics* , **225**, 985.

Wilson, A., Chadwick, A.V. Russell, N.V. and Whitham A.R., 1994, *Sensors and Actuators*, **B18**, 102.

Wu, N.L., Wang, S.Y. and Rusakova, I.A., 1999, *Science*, **285**, 1375.

Yamaguchi, Y and Kimiyama, H., 2001, *Nanoparticle Res.*, **3**, 105.

Yang, X, Pierre, A.C. and Uhlmann, D.R., 1988, *J. Non-Cryst. Solids*, **100**, 371.

Xue, L.A. and Brook, R.J., 1989, *J. Am. Ceram. Soc.*, **72**, 341.

Zaharescu, M., Crisan, M., Jitianu, A., Crisan, D., Meghea. A and Rau, I., 2000, *J. Sol-gel Sci. Tech.*, **19**, 631.

Zhang, J, Wang, B.J., Ju, X., Liu, T and Hu, T.D., 2001, *Polymer*, **42**, 3697.

Ziehfreund, A. and Maier, W.F., 1996, *Chem. Mat.*, **8**, 2721.